Theoretical and Computational Explorations of Topological Materials

By

ANIRUDHA MENON

DISSERTATION

Submitted in partial satisfaction of the requirements for the degree of

DOCTOR OF PHILOSOPHY

in

Physics

in the

OFFICE OF GRADUATE STUDIES

of the

UNIVERSITY OF CALIFORNIA

DAVIS

Approved:

Rajiv R. P. Singh (Chair)

Richard T. Scalettar

Andrew K. Waldron

Committee in Charge

2021

There are many people who have positively shaped my life. The ones mentioned below hold a special place in my heart. I would like to thank them in every way possible for without them, I would not be me. To them, I dedicate this dissertation.

To my mother, for showing me the true power of gritty determination and unwavering affection.

To Dr. Rajiv Singh, for being there to discuss science at any possible time and for mentoring and supporting me through my Ph.D.

To Dr. Banasri Basu, for showing me the light when I wanted to shift fields, and for the years of collaboration and support.

To Tuli Bhattacharya, for always having a smile on her face and reminding me that life is right now.

To Natalie Krzyanowski, for her enduring friendship, and for her countless qualities.

To Mayank Sanganeria, for always being there when I needed him most.

To Runa Roy, for her inimitable style of discussing pop-science.

To Ondrea Clarkson, for introducing me to Spike. And for showing me that skills can be acquired.

I would like to end by recalling a set of words that always brings me joy.

All that is gold does not glitter,
Not all those who wander are lost;
The old that is strong does not wither,
Deep roots are not reached by the frost.
From the ashes a fire shall be woken,
A light from the shadows shall spring;
Renewed shall be blade that was broken,
The crownless again shall be king.

– J. R. R. Tolkien

Acknowledgments

A significant portion of this work was performed under the auspices of the U.S. Department of Energy by Lawrence Livermore National Laboratory under Contract DE-AC52-07NA27344 - document release numbers LLNL-JRNL-778510 and LLNL-JRNL-796781. This work is supported in part by National Science Foundation grant number NSF-DMR 1855111 and by grant number NSF-PHY 1748958.

Contents

List of Figures

Abstract

Topological materials are of great interest to condensed matter physicists and engineers alike due to their potential application in quantum technology. To this end, two materials in this class, Weyl semimetals and quantum spin liquids, are studied in this dissertation using a set of computational and theoretical techniques.

Quantum spin ice models are studied using exact diagonalization, numerical linked cluster expansions, and perturbation theory. We calculate a host of observables like entanglement entropy and Ising correlation, and use them extract the phase boundaries of these models as a function of model parameters. These results have potential application in the experimental study of rare-earth pyrochlores.

We study the Hall transport properties of Weyl and multi-Weyl semimetals under the periodic drive of a laser pulse using analytical methods such as the Kubo formalism and the Matsubara Green's function formalism. Physical quantities such as the thermal Hall and Nernst conductivities are extracted for such models. The information obtained is analyzed and we show the characteristics of the transport coefficients as a function of monopole charge.

Chapter 1

Introduction

1.1 Topological materials

In this thesis, we will examine the role of topology in modern condensed matter physics using a gamut of analytical and numerical techniques. The two most in-vogue classes of topological materials are Dirac materials and quantum spin liquids (QSLs). Besides the plethora of exotic phenomena they are predicted (and in some cases, shown) to host, they find potential applications in the future of quantum technology. Dirac materials [1, 2] are those which host Dirac (or Weyl) points in their energy dispersion in momentum space, and form the low energy manifestations of Dirac (or Weyl) fermions. Over the last two decades Dirac materials such as topological insulators, Dirac semimetals (DSMs), and Weyl semimetals (WSMs) have been studied both theoretically and experimentally. QSLs [3, 4], on the other hand, are a form of quantum matter which exhibit long range entanglement and fractional quasiparticle excitations. They are topologically ordered systems which do not fit the Landau paradigm of distinguishing phases based on symmetries. Despite a plethora of proposals for quantum spin liquid materials, definitive demonstration of their existence is lacking. In what follows we dive in to a deeper understanding of these exotic

phenomena. The following subsections are classed into two sets: the first four cover topics related to QSLs whereas the remaining five covers WSMs.

1.2 Topological paradigms in low energy physics - I

Topology is the study of deformable spaces - those that maybe smoothly reshaped without introducing holes or tearing them. It is apriori unclear as to how this abstract mathematical subject may be relevant to condensed matter physicists. Remarkably however, it shows up in more than one way in modern condensed matter physics. One of the striking discoveries of the 1980's was that of *topological order* [3, 4]. Before that, it was thought that all phases of matter could be classified using Landau's theory. Put simply, Landau's theory [5] states that a phase is characterized by local order which is associated with the preserved/ broken symmetries of the system. There were at least two distinct developments that led to the inception of topological order. The first idea is the chiral spin state [6, 7], which was conjectured to describe high temperature superconductivity. While experiments proved otherwise, it was realized that there are many distinct chiral spin states with exactly the same symmetries, thereby escaping Landau's description. This new type of order was named topological order, motivated by the fact that the underlying effective theory is a topological quantum field theory. The notion of topological order also came about from another astonishing observation, this time in the fractional quantum Hall effect (FQHE) [7, 8]. In this phenomenon, the different Hall conductivities, which depend on the filling factor $\sigma_H = \nu \frac{e^2}{2\pi\hbar}$, represent different phases, all of which have the same symmetries. Thus Landau's theory does not permit one to distinguish between the different FQH phases described by rational values of ν. Hallmark features of topologically ordered phases include long-range entanglement and quasi-particles excitations with fractional statistics.

It turns out that magnetic systems can also exhibit topological order. Typically one would expect that when magnets in two and three dimensions are cooled down to zero temperature, they develop long-range order. However, the presence of geometric frustration can prevent this outcome by virtue of competing spin interactions that cannot be simultaneously satisfied. The simplest example of geometric frustration can be seen by imagining a three site triangular lattice Ising antiferromagnet with one up and one down spin. There is no choice for the remaining spin which would lead to a non-degenerate ground state. Geometric frustration can lead to a macroscopic degeneracy in the ground state manifold for such systems - a classical spin liquid. A quantum spin liquid is induced by introducing quantum fluctuations which pick out a unique ground state via superposition, leading to long range entanglement.

1.2.1 Quantum Entanglement

The idea of quantum entanglement dates back to the Einstein-Podolsky-Rosen (EPR) paradox [9] and is a feature of quantum mechanics with no classical analog. The textbook example of this phenomenon is explained using the Bell pair - a pair of electrons (spin 1/2 particles) A and B with the following state:

$$|\psi\rangle = \frac{1}{\sqrt{2}}(|\uparrow\rangle_A |\downarrow\rangle_B - |\downarrow\rangle_A |\uparrow\rangle_B). \tag{1.1}$$

If we measure the spin of either electron, we automatically know the state of the other electron, no matter how far they are spatially separated. This is what Einstein called "spooky action at a distance" and he used it to argue that quantum mechanics was flawed - surely information cannot travel faster than the speed of light! Despite its reputation with experiments, quantum mechanics wasn't universally accepted for quite a while. It wasn't until in 1964, when John Bell [10] came along and showed that no classical system would ever be able to reproduce the effects of quantum mechanics,

that the validity of quantum mechanics stood on incontrovertible ground.

In order to measure the degree of entanglement, an excellent object is the von Neumann entropy, defined in terms of ρ, the density matrix of the system. The von-Neumann entropy (henceforth referred to as entanglement entropy) answers the question

"If a system is divided into two subsystems (say A and B), how much is subsystem A entangled with subsystem B?"

The entanglement entropy is defined as

$$S = -\operatorname{Tr}[\rho_A \log \rho_A] = -\operatorname{Tr}[\rho_B \log \rho_B], \tag{1.2}$$

where ρ_A and ρ_B are the reduced density matrices given by $\rho_A = Tr_B(\rho)$ and $\rho_B = Tr_A(\rho)$ respectively. The Hilbert space $\mathcal{H}$ of the whole system can be decomposed as a direct product of the Hilbert space of the subsystems $\mathcal{H} = \mathcal{H}_A \otimes \mathcal{H}_B$. A product state is one where the wave-function can be decomposed as $|\psi\rangle = |\psi_A\rangle \otimes |\psi_B\rangle$, with $|\psi_A\rangle\, \epsilon \mathcal{H}_A$ and $|\psi_B\rangle\, \epsilon \mathcal{H}_B$, and the entanglement entropy vanishes for such a state. We will use the von-Neumann entropy as the measure of entanglement throughout the dissertation.

1.2.2 Valence bonds, resonance, and spin liquids

Its now appropriate to consider the original idea of a spin liquid. This concept was proposed by Philip W. Anderson as a variational solution for the ground state of the Heisenberg antiferromagnet on a triangular lattice [11]. While the proposal turned out to be incorrect, the idea of a spin liquid state persisted in the imaginations of physicists. In this segment, we will review the basic building blocks of Anderson's

idea. Defining the Bell pair [eqn.(4.1)] as a singlet, one can imagine tiling a triangular lattice of N spins with $N/2$ singlets. This state is the so called valence bond (VB) state $|\phi\rangle$, and while all spins are entangled with at least one other spin, the entanglement is not long-ranged. To incorporate this missing feature, Anderson considered a superposition of all such valence bond coverings of the triangular lattice, leading to the construction of the resonating valence bond (RVB) state - a quantum spin liquid (QSL)! The defining property of a QSL phase is that it exhibits long range entanglement, though other more restrictive definitions exist in the literature.

As we shall see resonances are a key component in the formation of QSLs, a fact which will be unearthed using geometry and perturbation theory. A somewhat coarse classification of QSLs [4] splits them into two classes: gapped QSLs and ungapped QSLs. By "gapped" we mean that there is an energy gap between the ground state and the first excited state of the QSL. Gapped QSLs usually have well defined emergent quasi-particle excitations (spinons, magnetic monopoles, anyons, etc.) with a topological structure which forces creation (and annihilation) in pairs. Due to the resonating nature of the QSL phase these quasi-particles can be arbitrarily separated at finite energy cost! Gapless spin liquids, on the other hand, can lead to the breakdown of the quasi-particle description. They typically have power-law correlations for their observables. Next we consider a class of materials which are thought to host a type of QSL called a quantum spin ice.

1.2.3 Spin-ice models

One class of materials that has attracted significant interest in the search for QSLs is the spin-ice family of rare-earth pyrochlores [12–20]. Magnetic rare-earth ions form a lattice of corner-sharing tetrahedra. Though these ions typically have large spin, strong spin-orbit coupling and crystal-field effects map them on to an effective two-state or spin-half system. The local Ising axis is defined by the line joining the vertex

to the center of the tetrahedron. When exchange interactions favor '2-in-2-out' Ising states in each tetrahedron, this leads to macroscopic ground state degeneracy at the classical level with the well-known Pauling entropy [21]. This classical spin-liquid, also called spin-ice, is well established in some rare earth pyrochlores [13].

These materials can be divided into Kramers and non-Kramers systems [12]. The former consist of odd number of electrons per ion which must have a two-fold degeneracy for every single-ion eigenstate. The latter will typically have non-degenerate eigenstates and double degeneracy can only arise as a result of some lattice symmetry. Thus spin-active non-Kramers systems can arise from two nearby non-degenerate lowest-energy states well separated from the rest, or, from a lattice-symmetry protected doublet ground state which will be split by any impurities. These systems can be modelled by random-transverse field Ising models (RTFIMs) [22–27]. Indeed the material $Pr_2Zr_2O_7$ is a realization of this model [28].

The pyrochlore lattice consists of corner-sharing tetrahedra and is not a Bravais lattice. Each pyrochlore site is part of two-tetrahedra and each tetrahedron has four sites. One way to construct the pyrochlore lattice is to consider an F.C.C. lattice of lattice constant a with tetrahedra centred on each site with the vertices located at $(a/8, a/8, a/8)$, $(-a/8, -a/8, a/8)$, $(-a/8, a/8, -a/8)$ and $(a/8, -a/8, -a/8)$. The random transverse field Ising model (RTFIM) is defined by the following local Hamiltonian.

$$H = J \sum_{<ij>} \sigma_i^z \sigma_j^z + \sum_i h_i \sigma_i^x \tag{1.3}$$

$< i, j >$ represents nearest neighbors pyrochlore sites i and j, J represents the Ising coupling, σ^μ represent the spin 1/2 Pauli matrices, and h_i represent the local transverse random fields. As stated previously, the Ising z-axis at each site is local and points towards the center of the tetrahedon. Since σ_i^z's commute with the Ising term, the Hamiltonian is unitarily equivalent to an RTFIM with the local fields pointing

along any direction in the $x-y$ plane. Note that this is not the most general Hamiltonian allowed by symmetries on a pyrochlore lattice. We study this model extensively in Chapter 2 using exact diagonalization and numerical linked cluster expansions (NLCE). Since we have an easy Ising axis favoring the '2-in 2-out' states, one can use perturbation theory to derive an effective Hamiltonian with the space of states restricted to the spin-ice manifold. The relevant degenerate perturbation theory scheme is described by [16]

$$H_{eff} = (1-\mathcal{P})\Big[- H^{'}\frac{\mathcal{P}}{H_I}H^{'} + H^{'}\frac{\mathcal{P}}{H_I}H^{'}\frac{\mathcal{P}}{H_I}H^{'} + \dots \Big](1-\mathcal{P}), \tag{1.4}$$

where $H_I = J\sum_{<ij>}\sigma_i^z\sigma_j^z$, $H^{'} = \sum_i h_i\sigma_i^x$, and $\mathcal{P}$ is the projection onto the orthogonal complement of the spin-ice manifold. $H^{'}$ introduces quantum fluctuations leading to the spin liquid groundstate for the model at $|h_i| \ll J$. The effective Hamiltonian picks up non-trivial contributions at fourth and sixth orders in perturbation theory leading to

$$H_{eff} = \ \tfrac{1}{48}\sum_{<i,j>} h_i^2h_j^2\sigma_i^z\sigma_j^z - \tfrac{63}{256}\sum_u K_u(\sigma_1^+\sigma_2^-\sigma_3^+\sigma_4^-\sigma_5^+\sigma_6^- \ + \ h.c.), \tag{1.5}$$

where u is a sum over all hexagonal rings on the pyrochlore lattice, and $K_u = h_1h_2h_3h_4h_5h_6$. The essence of the QSL physics stems from the ring-exchange term while the local Ising term enriches the phase diagram generated by the model. We discuss the physics of this model in Chapter 3 from a computational viewpoint.

We now switch gears and discuss some exotic physics in a related model. Ring-exchanges are not uncommon in pyrochlore based QSL setups, with a striking example being the seminal work by Hermele et. al. [16] on the easy-axis Heisenberg model. Perturbation theory along the easy axis (Ising axis) generates a similar ring-exchange term for that model although the Ising term (presented in the RTFIM) does not exist.

The starting observation is the fact that the pure ring-exchange term is equivalent to a quantum dimer model on a diamond lattice. As shown by Rokhsar and Kivelson [29], quantum dimer models generically have a point in their parameter space where they are exactly solvable, aptly named the RK point. Further, this model can be shown to be equivalent to a $U(1)$ compact lattice gauge theory [16], specifically lattice QED - this theory supports artificial photons, and magnetic and electric excitations, among other things. As a future direction, it would be interesting to see how the local Ising term affects the structure of this gauge theory, and its consequences on the observables in that language. The hope is to add to the list of established spin liquid phenomena to aid in its experimental detection.

1.2.4 Computational tools to probe many body spin models

1.2.4.1 Exact diagonalization and Krylov space methods

Exact Diagonalization (ED) is the most direct method to analyze quantum spin lattice models involving many body Hamiltonians. The idea is to find a matrix representation of the many-body Hamiltonian and calculate the eigenvalues and eigenvectors using a computer program. The system sizes accessible by modern computers and state-of-the-art algorithms is ~ 50 sites worth of spin 1/2 particles [30]. This is mainly due to the fact that the Hilbert space sizes of quantum systems scale exponentially with particle number N, and in the case of spin s particles this equals $(2s+1)^N$ states. Clearly then, any real system with an Avogadro number's worth of particles cannot be treated by this technique. To remedy this, one typically uses Born-von Karman (periodic) boundary conditions on systems of finite size. Despite being a widely used technique, in many cases finite size effects persist.

Additionally, fully diagonalizing matrices of size 2^{50} is computationally impossible given current standards. Luckily, all of the calculations done in this thesis are at zero temperature, which means that only the ground state of the system is relevant.

There exist a class of algorithms called Krylov space techniques which may be used to determine the low-lying and high-lying eigenvalues and eigenvectors of a Hamiltonian. In our works we employ one such algorithm, called the Lanczos algorithm, which converges to the spectrum iteratively. We now outline the Lanczos algorithm.

The number of Lanczos iterations m depends on the N and also the degree of numerical precision desired. Given an $N \times N$ Hermitian matrix and $m <= N$, the Lanczos Algorithm proceeds as follows: We initialize a unit norm arbitrary n-dimensional vector $v_1 \in \mathbb{C}$. The iteration steps are outlined in table 1.2.4.1.

First iteration step	Remaining Iteration steps
$w_1^{'} = Hv_1$	$\beta_j = \lvert w_{j-1} \rvert$
$\alpha_1 = w_1^{*'} v_1$	$v_j = w_{j-1}/\beta_j$
$w_1 = w_1^{'} - \alpha v_1$	$w_j^{'} = Hv_j$
	$\alpha_j = w_j^{'*} v_j$
	$w_j = w_j^{'} - \alpha v_j - \beta_j v_{j-1}$

Next we construct a $m \times m$ tridiagonal matrix T as

$$\begin{bmatrix} \alpha_1 & \beta_2 & & \dots & & 0 \\ \beta_2 & \alpha_2 & \beta_3 & & & \\ & \beta_3 & & & & \\ & & & \ddots & & \\ & & & & \alpha_{m-1} & \beta_m \\ 0 & & \dots & & \beta_m & \alpha_m \end{bmatrix} \tag{1.6}$$

The eigenvalues of H coincide with the eigenvalues of T which is a much smaller matrix and easier to diagonalize. The corresponding eigenvectors can also be obtained without too much difficulty.

1.2.4.2 Numerical Linked Cluster Expansions

As we have seen, the results of studying systems with ED may not hold in the thermodynamic limit. To probe the behavior of physical quantities in this limit, a class of methods commonly employed is series expansions. A typical course in statistical mechanics covers the high temperature expansion (HTE) and the low temperature expansion (LTE) methods [31]. As their respective names suggest, they are valid in the high and low temperatures regimes. The HTE involves a series expansion of in powers of $\beta = 1/k_B T$ where each term represents a graph on the lattice. These graphs are typically ordered by bonds and a finite number of terms are retained in any computation. The HTE fails below a certain temperature T_c set by the energy scales of the system's Hamiltonian. A potent tool in the set of series expansion methods is the numerical linked cluster expansion (NLCE) [32–35]. This involves the expansion of a physical quantity (in the thermodynamic limit) in a series of graphs. Such an expansion can converge below T_c as long as the correlations of the system are short-ranged. We now briefly describe the prescription for the NLCE. An extensive property of interest P, per site, can be calculated by a sum over connected clusters C that can be embedded in the lattice.

$$P/N = \sum_C L(C) \times W(C), \tag{1.7}$$

where $L(C)$ is the lattice constant of the cluster, or the number of times the cluster arises in the lattice per site. The weight $W(C)$ is defined recursively as

$$W(C) = P(C) - \sum_c W(c), \tag{1.8}$$

where $P(c)$ is the property for the cluster and the subtraction is over all sub-clusters $c \subset C$. It turns out that there is greater freedom in the choice of graphs for the

NLCE as compared to the HTE. As shown in [32, 35] one can choose to order graphs by sites, bonds, and even larger units - typically these larger units can be translated to reproduce the entire lattice without any overlapping bonds. We have used both the regular NLCE and a modified version to probe spin-ice physics, as described in Chapter 3.

1.3 Topological paradigms in low energy physics - II

The role of topology in condensed matter physics can be viewed through a different lens. This second part of our journey starts with the notion of the Berry phase or geometric phase. Essentially, the idea is to determine how the wave-function of a state changes due to the adiabatic variation of the parameters of the Hamiltonian. Berry's phase demonstrates how geometry and topology interplay with each other in condensed matter. It is closely linked to the quantum Hall effect as we shall see [8]. Additionally, it provides crucial insight to Weyl semimetal physics by the Chern number - a topological invariant representing the monopole charge of a Weyl point [1].

1.3.1 Geometric Phases and Chern Numbers

A great place to start discussing the role of geometry and topology in modern physics is the subject of Berry phases or more precisely Berry holonomy [8]. Michael Berry discovered this phenomenon in 1985 when he considered the following question:

"Imagine that a Hamiltonian is dependent on the usual phase space variables x_μ and a parameter λ. How does the wavefunction of a particular state change when this parameter is varied slowly?"

By "slowly" we mean that the parameter is varied adiabatically. For simplicity let us assume that we are interested in the ground state and that it is non-degenerate. The *adiabatic theorem* answers the question almost completely. It tells us that as long as we avoid a level crossing, the system will cling to the groundstate $|n\rangle$ as the parameter is varied adiabatically. However, there is one piece of information that is missing - the state can (and will) pick up an overall phase factor which is left undetermined.

$$|\psi\rangle \to e^{i\gamma} |\psi\rangle \tag{1.9}$$

This phase $e^{i\gamma}$ is precisely the Berry phase and it can be computed. The final result for a closed path C in parameter space reads

$$e^{i\gamma} = exp\Big(-i \oint_C \mathcal{A}(\lambda) d\lambda \Big) \tag{1.10}$$

The Berry phase does not depend on the time taken to traverse the path, but does depend on the path taken. $\mathcal{A}$ is called the Berry connection and is defined as

$$\mathcal{A} = -i \langle n| \frac{\partial}{\partial \lambda} |n\rangle . \tag{1.11}$$

The Berry connection is identical in formulation to the electromagnetic vector potential. It also exhibits a gauge redundancy and in fact the gauge invariant quantity turns out to be the corresponding Berry 2-form, equivalently, Berry curvature, defined as

$$\mathcal{F}_{ij} = \frac{\partial \mathcal{A}_i}{\partial \lambda^j} - \frac{\partial \mathcal{A}_j}{\partial \lambda^i}. \tag{1.12}$$

Note that we've introduced indices on the parameter - the parameter is not neces-

sarily one dimensional and we suppressed the index so far for brevity. Using Stokes' theorem, the Berry phase exponent can be expressed as

$$e^{i\gamma} = \exp\left(-i \oint_C \mathcal{A}_i d\lambda^i \right) = \exp\left(-i \int \mathcal{F}_{ij} dS^{ij} \right). \tag{1.13}$$

We now switch to a toy model to elucidate some instructive results associated with the Berry phase. Consider the Hamiltonian

$$H = -\vec{B} \cdot \vec{\sigma} + B, \tag{1.14}$$

where we will treat the magnetic field $\vec{B}$ as our parameter. One can readily show that the ground state energy of this Hamiltonian is zero, so the only phase accumulated when $\vec{B}$ is varied is the Berry phase. A straightforward calculation yields the Berry curvature,

$$\mathcal{F}_{ij}(\vec{B}) = -\epsilon_{ijk} \frac{g B^k}{B^3}. \tag{1.15}$$

On closer examination, we see that the field strength represents a magnetic monopole. $g = 1/2$ plays the role of magnetic charge. The monopole is a source for Berry flux - as easily seen by integrating the 2-form over a 2-sphere to yield $4\pi g = 2\pi$. We can extract one more crucial piece of information. Imagine that we integrate the Berry curvature over some solid angle Ω covering the surface of a sphere. For every closed curve on the surface of a sphere there are two distinct choices of surfaces enclosed. This would imply the consistency condition

$$e^{i\gamma} = \exp\left(\frac{i\Omega}{2} \right) \stackrel{!}{=} \exp\left(\frac{i(8\pi g - \Omega)}{2} \right) \tag{1.16}$$

Enforcing the last equality requires that $2g \in \mathbb{Z}$ - the quantization of magnetic charge. This quantization criteria is also present for a general Berry 2-form, which

when integrated over a closed surface must equal $2\pi C$, where $C \in \mathbb{Z}$ is called the *Chern number*.

Berry phases are intimately related to Weyl monopoles in momentum space and anomalous Hall phases, which are central themes to this dissertation. Further details are discussed in succeeding subsections.

1.3.2 Weyl and Dirac Fermions

In 1929, Paul Dirac produced his seminal work uniting the principles of special relativity with quantum mechanics. In doing so, he constructed the Dirac equation which describes Dirac fermions [1, 36]. The equation requires the use of four-component objects called Dirac spinors ψ and can be compactly written as

$$\big[i\gamma^\mu \partial_\mu - m\big]\psi = 0. \tag{1.17}$$

The index $\mu = 0, 1, 2, 3$ label the $3 + 1$ space-time dimensions, and the Einstein summation convention is used to handle sums. m represents the mass of the Dirac fermion, and the four 4×4 matrices γ^μ form a representation of the Clifford algebra:

$$\{\gamma^\mu, \gamma^\nu\} = 2\eta^{\mu\nu} I_4, \tag{1.18}$$

where $\eta^{\mu\nu}$ is the Minkowski metric and I_4 is the 4×4 identity matrix.

Hermann Weyl noticed a special property of the Dirac equation in even space-time dimensions [1, 36]. It turns out that for massless fermions, the Dirac equation decouples further into two equations describing two two-component fermions. These fermions are, respectively, left and right handed Weyl fermions (ψ_L, ψ_R), and the corresponding set of equations are called the Weyl equations:

$$\sigma^\mu \partial_\mu \psi_R = 0, \qquad\qquad \bar{\sigma}^\mu \partial_\mu \psi_L = 0. \tag{1.19}$$

The set of matrices σ and $\bar{\sigma}$ are given by $\sigma = [I_2, \sigma_x, \sigma_y, \sigma_z]$ and $\sigma = [I_2, -\sigma_x, -\sigma_y, -\sigma_z]$, $(\sigma_x, \sigma_y, \sigma_z)$ are the three Pauli matrices. The Weyl fermions are chiral in that they have definite helicity (spin-momentum locking) - either the spin is parallel to the momentum or it is anti-parallel. This is best understood by considering the Weyl Hamiltonian (the Hamiltonian whose equations of motion are the Weyl equations) in momentum space. A straightforward calculation shows that

$$H_{\text{Weyl}} = \pm \vec{p} \cdot \vec{\sigma}. \tag{1.20}$$

With this we can make the connection between Weyl fermions and their manifestations in condensed matter physics. It turns out that near certain band-touching points (called diabolic points or Weyl points) of certain materials, the effective Hamiltonian of the system turns out to take the form of Eqn. 1.20. Thus we find the low-energy realization of these relativistic objects and such materials are called Weyl semimetals. We will make the connection explicit later by deriving the low energy model from a lattice model of Weyl semimetals. A word of caution: simply having the Weyl Hamiltonian as the effective theory is insufficient to classify a material as a WSM. One also requires that the chemical potential be sufficiently close to the diabolic or Weyl points.

1.3.3 Accidental degeneracies and Weyl semimetals

Accidental degeneracies are not very common in all dimensions, especially in the absence of symmetries. To understand this statement further, we consider the following generic two-band model in momentum space

$$H = f_0(k) + f_1(k)\sigma_x + f_2(k)\sigma_y f_3(k)\sigma_z. \tag{1.21}$$

The energies of this Hamiltonian are $E_\pm = f_0(k) \pm \sqrt{f_1(k)^2 + f_2(k)^2 + f_3(k)^2}$. We see

that in order for the bands to be degenerate, even at a single point, we require that $f_1(k)^2 + f_2(k)^2 + f_3(k)^2 = 0$ - a condition which may only be satisfied by setting three independent parameters to zero, i.e., $f_1(k) = f_2(k) = f_3(k) = 0$. Thus, it is only in three dimensions that one readily encounters point degeneracies [1]. This is not the end of the story as one must also consider the possible symmetries of the system. For example if both parity (inversion, $\mathcal{I} : \vec{r} \to -\vec{r}$) and time-reversal symmetries ($\mathcal{T}$) are simultaneously present, every momentum $\vec{k}$ maps back to itself and hence all bands are doubly degenerate. If on the other hand if only $\mathcal{T}$ is present, then $\vec{k} \to -\vec{k}$ and so the only point at which degeneracy can occur is $\vec{k} = 0$. A similar story prevails when only inversion symmetry is present.

Weyl semimetals are materials where band degeneracies occur at pairs of points (called Weyl points) throughout the Brillouin zone with the added ingredient that the Fermi surface is sufficiently close to the Weyl points. Based on the above discussion, it becomes clear that WSMs models break $\mathcal{T}$ or $\mathcal{I}$ [37–40]. The minimal time reversal symmetry breaking model, consists of a Dirac-like dispersion around two distinct points in the first Brillouin zone, where the conduction and the valence bands touch. These Weyl points or Weyl nodes are topological charges acting as a source or a sink for Berry curvature [38, 41, 42]. They occur in opposite chirality pairs by virtue of the Nielsen-Ninomiya fermion doubling theorem. The inversion symmetry breaking minimal model requires four Weyl points [37, 40]. Such materials, classed as type-I WSMs, exhibit a number of phenomena including chiral magnetic waves [43], chiral anomaly induced plasmon modes [44], and chirality induced negative magneto resistance [45].

The addition of a SO(3,1) symmetry breaking term to the low energy Hamiltonian coupled to the momentum leads to a tilt in the dispersion relation. For sufficiently large tilts, it can be shown [37] that a Lifshitz phase transition occurs, leading to a new phase i.e. type-II WSMs, with different physical properties. Type-I WSMs have

a point-like Fermi surface, whereas in type-II WSMs, the Fermi surface splits into two, one each for electrons and holes, such that the density of states at each Weyl points is finite. Reports on the experimental realizations of type-I Weyl semimetals have been presented in [46, 47], and it was shown in [48] that WTe_2 is a possible experimental candidate for the type-II WSM phase.

As compared to $n = 1$ WSMs, n can be generically greater than one in some materials, determined by the crystallographic point symmetries. These are called as multi WSMs (mWSMs). Recent theoretical reports claim $SiSr_2$ and $HgCr_2Se_4$ as possible candidates [42, 49, 50] for mWSMs with monopole charge $n = 2$. Double-Weyl ($n = 2$) and triple-Weyl ($n = 3$) semimetals have the quadratic and cubic energy dispersion relations near the Weyl points, respectively. The dispersion anisotropy in mWSMs coupled with spin-momentum locking has the potential to give rise to unique quantum effects and transport signatures [51, 52]. The respective minimal models for tilted WSMs and mWSMs are presented in Chapters 3 and 4. Their derivations from lattice models are presented in Appendix B part A.

1.3.4 Time periodic drive and Floquet theory

Most real world quantum mechanical problems are time dependent. Such is the nature of the Schrödinger equation, however, that in some cases we are able to solve it in terms of time independent functions and time dependent functions, separately. This class of problems correspond to potentials which are time independent leading to the system possessing time translation symmetry. Time dependent potentials pose a different and formidable challenge in most cases - the usual recourse being to apply time dependent perturbation theory. In some cases we find that the time dependent potentials are periodic and this particular property enables us to solve the corresponding problem by mapping to a time independent picture [53–55]. We begin by considering a Hamiltonian $H(t)$ which is periodic with a time period T such that

$$H(t+T) = H(t). \tag{1.22}$$

The Hamiltonian possesses the symmetry of discrete time translations. We assume that the Hamiltonian consists of a time independent piece H_0 with a complete set of orthonormal eigenstates $\{\phi_n(x)\}$, and a time dependent piece $V(t)$. Similar in spirit to Bloch's theorem, one can then apply Floquet's theorem to show that there exist solutions $\psi(x,t)$ to the full time dependent Schrodinger equation of the form

$$\psi_\alpha(x,t) = e^{-i\epsilon_\alpha t}\Phi_\alpha(t). \tag{1.23}$$

$\phi_\alpha(t)$ shares the period of the Hamiltonian, i.e., $\phi_\alpha(t+T) = \phi_\alpha(t)$. The ϵ_α's are the so called *quasi energies* and are defined only up to to integer multiples of $\hbar\omega$, where $\omega = 2\pi/T$. All of this should appear analogous to Bloch's theorem where the momenta are only defined up to reciprocal lattice vectors. The periodic piece of the solution also has the following property

$$\left[H(x,t) - i\hbar\frac{d}{dt}\right]\Phi_\alpha(x,t) = \epsilon_\alpha\Phi_\alpha(x,t). \tag{1.24}$$

The eigenvectors of the full Hamiltonian satisfy the following time-averaged orthonormality criteria:

$$\langle\langle\Phi_\alpha|\Phi_\beta\rangle\rangle = \int_0^T dt \int_{-\infty}^{\infty} dx \;\; \Phi_\alpha^*(x,t) \;\; \Phi_\beta(x,t) = \delta_{\alpha,\beta}. \tag{1.25}$$

Note that the full Hilbert space of solutions has a product structure - this will not be crucial to our current discussion and we omit this.

The Floquet time evolution operator is defined over a period as

$$U(T) = \mathcal{T}\exp\left[-\frac{i}{\hbar}\int_0^T H(t)\,dt\right], \tag{1.26}$$

where $\mathcal{T}$ represents the time-ordering operator. One can then derive a static effective Hamiltonian H_{eff}, by requiring that

$$H_{eff} = \frac{i\hbar}{T} \log \left(\exp \left[-\frac{i}{\hbar} \int_0^T dt\, H(t) \right] \right) \tag{1.27}$$

This ansatz forms the basis of the high frequency or van-Vleck expansion [54, 55]. By algebraic manipulation, one can show that the effective Hamiltonian takes the form of a series expansion in increasing powers of inverse frequency, $H_{eff} = \sum_{n=0}^{\infty} H^{(n)}$ with $H^{(n)} \sim \omega^{-n}$. We begin by expanding the Hamiltonian in frequency space as $H(t) = \sum_{l \epsilon \mathbb{Z}} H_l e^{i\omega l t}$. The forms for $H^{(n)}$ are shown below up to the second order.

$$\begin{aligned} H^{(0)} &= H_0 \\ H^{(1)} &= \frac{1}{\hbar\omega} \sum_{l=1}^{\infty} \frac{1}{l} [H_l, H_{-l}] \\ H^{(2)} &= \frac{1}{\hbar^2\omega^2} \sum_{l \neq 0} \left[\frac{[H_{-l}, [H_0, H_l]]}{2l^2} + \sum_{l' \neq 0, l} \frac{[H_{-l'}, [H_{l-l'}, H_l]]}{3ll'} \right] \end{aligned} \tag{1.28}$$

The systems that we consider in this dissertation involve periodic driving with a very high frequency laser - essentially, the laser field is used to drive the material to a steady state. This permits us to treat the van-Vleck expansion perturbatively and terminate the series to leading order. In what follows, we review the effects of Floquet theory on quantum transport.

1.3.5 Quantum Floquet transport and the anomalous quantum Hall effect

The classical Hall effect [56], discovered by Edwin Hall in 1879, is simply a consequence of the Lorentz force acting on a charged particle inside a conductor. One can envision this by imagining a 3D conductor with an electric field in the x-direction

which leads to a flow of charge. Introducing a constant magnetic field along the y-direction leads to a force acting on the particle in the z-direction given by

$$\vec{F} = q(\vec{v} \times \vec{B}) \tag{1.29}$$

Thus charges accumulate on the edges of the conductor depending on the sign of the charge and this eventually leads to equilibrium, wherein the effect of the magnetic field is canceled by the electric field generated by the accumulated charges. The corresponding transverse potential difference is called the Hall voltage.

The classical Hall effect can be modeled within the limits of Drude theory, whereby the equation of motion of the charge carriers in a conductor under the simultaneous effects of an electric field $\vec{E}$ and a magnetic field $\vec{B}$ is given by

$$m\frac{d\vec{v}}{dt} = -e\vec{E} - e\vec{v} \times \vec{B} - \frac{m\vec{v}}{\tau}. \tag{1.30}$$

m is the mass of the charge carrier, and τ models the scattering time within the material. Solving the equations of motion, one obtains a version of Ohm's law with the conductivity being a tensor instead of a single number. The off-diagonal components of this tensor represent the Hall conductivity, given in the Drude model by [8]

$$\sigma_{Hall} = \frac{ne^2\omega_B\tau^2}{1 + \omega_B^2\tau^2}. \tag{1.31}$$

The quantum Hall effect has been a subject of great interest since the early 1980's when von Klitzing explored the quantum realm of the Hall effect [8]. This led to a great number of discoveries including the integer quantum Hall effect and the fractional quantum Hall effect, the latter of which is partly responsible for the notion of topological order. The key element in both these effects is the quantization of the Hall conductivity, either in integer or in rational multiples of $\frac{e^2}{2\pi\hbar}$. Since then, many materials have been known to host quantum Hall phases.

A related effect is the quantum anomalous Hall effect [57], the classical version of which was also discovered by Edwin Hall in 1881. The quantum anomalous Hall effect (QAHE or AHE) refers to the contribution to Hall conductivity from spin-orbit coupling in ferromagnetic material. This effect is usually dependent on the magnetization of the material and comes in two flavors [58]: intrinsic or scattering between bands, and extrinsic or impurity scattering. Importantly, the time reversal symmetry broken WSM and mWSM phases studied in this dissertation support a quantum anomalous Hall phase due to their intrinsic magnetization.

An important tool to probe the effects of a perturbing field on a given system is linear response theory - the key aspect being that since the field can be treated perturbatively, the leading order response of the system is linear in the field. Within the framework of this theory is the Kubo-formula for the conductivity tensor [8]. Specifically, the component $\sigma_{\mu\nu}$ of the conductivity tensor is given by

$$\sigma_{\mu\nu}(\omega) \sim \sum_{m,n} \frac{f(E_n) - f(E_m)}{E_n - E_m} \frac{\langle n| J_\mu |m\rangle \langle m| J_\nu |n\rangle}{\omega - E_n + E_m - i\eta},$$

where continuum indices have been suppressed for brevity. We note that $f(E_m) = 1/[1+\exp(\beta(E_m-\mu))]$ represents the Fermi-Dirac distribution function, and $J_\mu = \frac{\partial H}{\partial k^\mu}$ is the current operator. The Kubo formula for conductivity can be recast into two very interesting and completely equivalent forms. The first one, called the Matsubara Green's function approach [59], is an alternative way to calculate the components of the conductivity tensor which is completely equivalent to the Kubo formula. The key component to this technique is to compute the single particle Green's function $G(i\omega, \vec{k})$. With this, one is able to compute the current-current correlation function

$$\Pi_{ij}(\Omega, \vec{q}) = T \sum_{\omega_n} J_i G(i\omega_n, \vec{k}) J_j G(i\omega_n - \Omega, \vec{k} - \vec{q})|_{i\Omega \to \Omega + i\delta}. \tag{1.32}$$

where $i, j = x, y, z$, T is the temperature (setting the Boltzmann constant to unity),

$\omega(\Omega)$ are the fermionic (bosonic) Matsubara frequencies, and the J_i's are the current operators. One can then relate the Hall conductivity to the current-current correlation function as follows:

$$\sigma_{xy} = -\lim_{\Omega \to 0} \frac{\Pi_{xy}}{i\Omega} \tag{1.33}$$

While this second formula for the Hall conductivity might seem tedious, in some cases it proves simpler and more instructive than using the Kubo formula. A second version of the Kubo formula was constructed by TKNN in their seminal 1982 work [60] relating the Hall conductivity to Berry curvature. This work connected quantum transport, geometry and topology. Their formulation can be expressed as

$$\sigma_{xy} = \frac{e^2}{\hbar} \int \frac{d^3k}{(2\pi)^3} f(E_k) \Omega_z(\vec{k}), \tag{1.34}$$

where $\Omega(\vec{k})$ is the Berry curvature. This simple formula has far reaching consequences for the physics of Weyl semimetals. For one, it can be shown that the vacuum contribution to the Hall conductivity (at zero chemical potential) is a topological invariant coupled to the strength of the WSM monopole charge. We will now introduce the central theme of the works on Weyl semimetals - Floquet transport.

Under a time periodic drive, a natural question concerns the variation of the transport properties. Essentially, control over the drive would imply control over the transport properties hence making this a viable research direction. As discussed in the previous section, Floquet's theorem permits us to map the time dependent problem to a time independent setting and indeed there turns out to be a very simple Kubo-like formula for the conductivity tensor $\sigma^F_{\mu\nu}$ in this setting [53].

$$\sigma^F_{\mu\nu} \sim \sum_{m,n} \frac{f(E_n) - f(E_m)}{E_n - E_m} \frac{\langle\langle n| J_\mu |m\rangle\rangle \langle\langle m| J_\nu |n\rangle\rangle}{E_n - E_m + i\eta}$$

This formula looks deceptively similar to the Kubo formula but has some major

differences. For starters, periodic driving introduces a non-equilibrium steady state and so the distribution functions are not the equilibrium distribution functions. Additionally, the states and energies used in this formula correspond to the eigenstates of the effective Floquet Hamiltonian and the corresponding quasi-energies. Finally, $\langle\langle\alpha|\beta\rangle\rangle = \frac{1}{T}\int_0^T \langle\alpha(t)|\beta(t)\rangle\, dt$ indicates a time average as well as an expectation value.

One might then wonder what happens to the Matsubara formalism in this Floquet-Kubo picture, and also what of the TKNN formula. The latter is addressed instantly [53]:

$$\sigma_{xy} = \frac{e^2}{\hbar}\int \frac{d^3k}{(2\pi)^3} f(E_k)[\nabla \times \mathcal{A}]_z, \tag{1.35}$$

where $\mathcal{A}$ is the Berry connection defined using the time averaged inner product mentioned above. In this dissertation, we show that for a class of Hamiltonians, the Floquet-Kubo formalism can be further simplified to a form which is indistinguishable from its static counterpart except for the use of the Floquet states and quasi-energies. We also derive a similar result for the Matsubara formalism to leading order in perturbation theory. We then explore the Floquet Hall conductivity and some associated effects using this formalism.

1.4 Summary of Results

In Chapter 2, we use Numerical Linked Cluster Expansions (NLCE) and Exact Diagonalization (ED) to study confinement transitions out of the Quantum Spin Liquid (QSL) phase in the pyrochlore-lattice Ising antiferromagnet with random transverse fields. We calculate entanglement entropies associated with local regions defined by single tetrahedra to observe these transitions. The randomness-induced confinement transition is marked by a sharp reduction in the local entanglement and a concomitant increase in Ising correlations. In NLCE, this is studied through the destruction

of loop resonances due to random transverse-fields. The confining phase is characterized by a broad distribution of local entanglement entropies, which persists to large random fields.

In Chapter 3, we study an effective spin model derived perturbatively from the random transverse-field Ising model on the pyrochlore lattice. The model consists of spin-configurations on the pyrochlore lattice, restricted to the spin-ice subspace, with spins interacting with random Ising exchange couplings as well as ring exchanges along the hexagons of the lattice. This model is studied by exact diagonalization up to N=64 site systems by restricting to the spin-ice manifold. We calculate spin-glass correlation functions and local entanglement entropy S_T between spins in a single tetrahedron and the rest of the system. We find that the model undergoes two phase transitions. At weak randomness the model is in a quantum spin-ice phase where $S_T = \ln 6$. Increasing randomness, at low transverse-fields, first leads to a frozen phase, with long-range spin-glass order and $S_T = \ln 2$ corresponding to the Cat states associated with Ising order. Further increase in randomness leads to a random resonating-hexagon phase with a frozen backbone of spins and a broad distribution of entanglement entropies. The implications of these studies for non-Kramers rare-earth pyrochlores are discussed.

In Chapter 4, we discuss the effect of a periodically driving circularly polarized laser beam in the high frequency limit, on the band structure and thermal transport properties of type-I and type-II Weyl semimetals (WSMs). We develop the notion of an effective Fermi surface stemming from the time-averaged Floquet Hamiltonian and discuss its effects on the steady-state occupation numbers of electrons and holes in the linearized model. In order to compute the transport coefficients averaged over a period of the incident laser source, we employ the Kubo formalism for Floquet states and show that the Kubo formula for the conductivity tensor retains its well known form with the difference that the eigenstates and energies are replaced by the Floquet

states and their quasi-energies. We find that for type-I WSMs the anomalous thermal Hall conductivity grows quadratically with the amplitude A_0 of the U(1) gauge field for low tilt, while the Nernst conductivity remains unaffected. For type-II WSMs, the Hall conductivity decreases non-linearly with A_0 due to the contribution from the physical momentum cutoff, required to keep finite electron and hole pocket sizes, and the Nernst conductivity falls of logarithmically with A_0^2. These results may serve as a diagnostic for material characterization and transport parameter tunability in WSMs, which are currently the subject of a wide range of experiments.

In Chapter 5, we discuss the circularly polarized light (of amplitude A_0 and frequency ω) driven thermo-electric transport properties of type-I and type-II multi-Weyl semimetals (mWSMs) in the high frequency limit. Considering the low energy model, we employ the Floquet-Kubo formalism to compute the thermal Hall and Nernst conductivities for both types of mWSMs. We show that the anisotropic nature of the dispersion for arbitrary integer monopole charge $n > 1$ plays an important role in determining the effective Fermi surface behavior; interestingly, one can observe momentum dependent corrections in Floquet mWSMs in addition to momentum independent contribution as observed for Floquet single WSMs. Apart from the non-trivial tuning of the Weyl node position $\pm Q \to \pm Q - A_0^{2n}/\omega$, our study reveals that the momentum independent terms result in leading order contribution in the conductivity tensor. This has the form of n times the single WSMs results with effective chemical potential $\mu \to \mu - A_0^{2n}/\omega$. On the other hand, momentum dependent corrections lead to sub-leading order terms which are algebraic functions of μ and are present for $n > 1$. Remarkably, this analysis further allows us to distinguish type-I mWSMs from their type-II counterparts. For type-II mWSMs, we find that the transport coefficients for $n \geq 2$ exhibit algebraic dependence on the momentum cutoff in addition to the weak logarithmic dependence as noticed for $n = 1$ WSMs. We demonstrate the variation and qualitative differences of transport coefficients between

type-I and type-II mWSMs as a function of external driving parameter ω.

Chapter 2

Local entanglement and confinement transitions in random transverse-field Ising model on the pyrochlore lattice

The results and discussion below are based on the article Phys. Rev. B **100**, 144437. This work was performed under the auspices of the U.S. Department of Energy by Lawrence Livermore National Laboratory under Contract DE-AC52-07NA27344. Document release number LLNL-JRNL-778510. The work of Dr. Rajiv R. P. Singh is supported by NSF-DMR grant number 1855111.

We study the quantum Ising-antiferromagnet on the pyrochlore lattice by Numerical Linked Cluster (NLC) expansions [32–34] and exact diagonalization (ED). We focus on the local entanglement properties of the system and examine their behavior at the confinement transitions. We find that local entanglement of the spins associated with a single tetrahedron with the rest of the system contains sharp changes associated with different confining transitions.

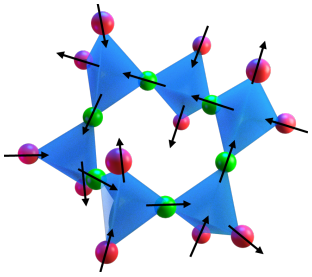

Figure 2.1: Cluster of 6 tetrahedra connected in a ring. The six interior sites of the cluster are denoted by green circles and the 12 boundary sites are denoted by red circles.

A simple NLC calculation diverges inside the QSL phase. To obtain convergent results, one must consider each cluster as embedded in a superposition of spin-ice states. The confinement transition can be observed by studying the destruction of ring-exchange resonance due to the random fields. A modification of Benton's perturbative argument [27] shows that at the phase boundary the width of the transverse-field distribution scales quadratically with the mean value in agreement with the NLC results. We also find that the confining phase [25] is characterized by a broad distribution of local entanglement entropies, a property which persists to high random fields. This means that even with increasing random fields there will be pockets of strong entanglement with local behavior of a QSL.

2.1 Model and Observables

We consider the Hamiltonian

$$\mathcal{H} = J \sum_{<i,j>} \sigma_i^z \sigma_j^z - \sum_i h_i \sigma_i^x, \tag{2.1}$$

where $J = 1$, and the transverse fields h_i are independent Gaussian random variables with mean h and standard deviation w. On a finite cluster with periodic boundary conditions, we calculate the ground state wavefunction of the system. We divide the

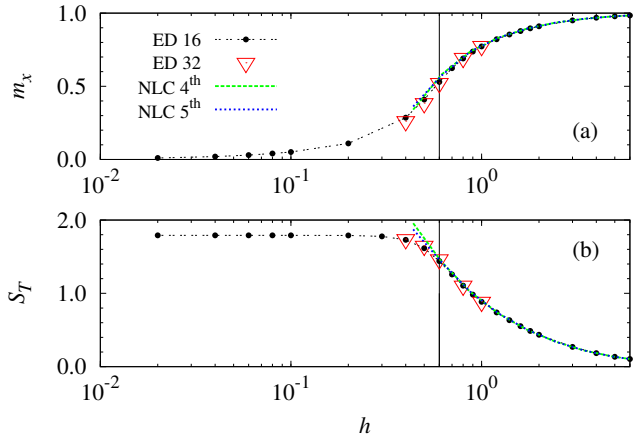

Figure 2.2: (a) Expectation value of spin along the transverse field m_x, and (b) Single-tetrahedron entanglement entropy S_T, as a function of the transverse-field h with no disorder. The data is for 16 and 32-site clusters and 4^{th} and 5^{th} order NLC. The vertical black lines denote the transition point [23, 24] between QSL and the paramagnetic phase. NLC does not converge within the QSL phase, and for this reason NLC results are not shown for small h values.

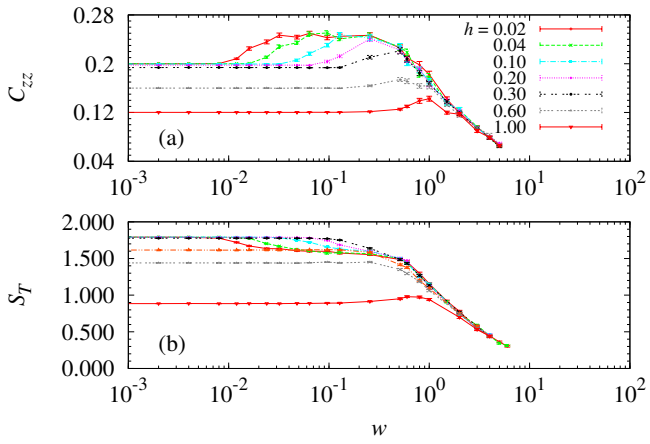

Figure 2.3: (a) Ising correlations C_{zz}, and (b) Single-tetrahedron entanglement entropy S_T as a function of width of the field distribution w for different mean values of the field h. Data have been obtained via ED on a 16-site cluster, and each data point represents the average over 100 independent random gaussian field distributions.

system into two parts A and its complement B. Let the reduced density matrix of A be ρ_A. The von-Neumann entanglement entropy between A and its complement B is:

$$S_A = S_B = -\operatorname{Tr} \rho_A \ln \rho_A. \tag{2.2}$$

In this work, A is made up of the four spins belonging to any single tetrahedron, and B is made up of all the remaining spins. This leads to the definition of single-tetrahedron entanglement entropy

$$S_T = -\operatorname{Tr} \rho_T \ln \rho_T. \tag{2.3}$$

This quantity is then averaged over the tetrahedra in the finite cluster. In addition, we study the average moment along the local field, defined as

$$m_x = [\frac{1}{N} \sum_i |\langle \sigma_i^x \rangle|]. \tag{2.4}$$

Here N is number of sites and the angular brackets throughout this study refer to ground state expectation values, while the square brackets refer to an average over disorder configurations. We also calculate the correlation sum for the Ising components:

$$C_{zz} = [\frac{1}{N(N-1)} \sum_{i,j \neq i} |\langle \sigma_i^z \sigma_j^z \rangle| \ ], \tag{2.5}$$

where the sum is over all pairs of spins.

2.2 Exact diagonalization and numerical linked cluster expansion

To obtain the results in the thermodynamic limit, we turn to NLC [32–34]. An extensive property of interest P, per site, can be calculated by a sum over connected

clusters c that can be embedded in the lattice.

$$P/N = \sum_c L(c) \times W(c), \tag{2.6}$$

where $L(c)$ is the lattice constant of the cluster, or the number of times the cluster arises in the lattice per site. The weight $W(c)$ is defined recursively as

$$W(c) = P(c) - \sum_s W(s), \tag{2.7}$$

where $P(c)$ is the property for the cluster and the subtraction is over subclusters.

To study property of spin-ice systems, it is useful to consider clusters made up of full tetrahedra [61–63]. To 5^{th} order, that is up to 5 tetrahedra, there are a total of 8 clusters. We include a 9th cluster, consisting of six tetrahedra in a ring, shown in Fig. 2.1, as it plays a special role in the spin-ice phase.

We begin with results for the uniform system ($w = 0$). In Fig. 2.2, the expectation value of the spin along the transverse field and the local entanglement entropy associated with a single tetrahedron are shown as a function of the field. The 4^{th} and 5^{th} order NLC results are indistinguishable in the plot in the high-field paramagnetic phase, showing that they represent the results in the thermodynamic limit. The ED results for 16− and 32−site clusters are also shown. In the thermodynamic limit, there may be a small discontinuity at the transition [23, 24], but finite size effects are small in the paramagnetic phase right down to the transition. This first order transition point from previous studies [23, 24] is indicated by the vertical black lines.

While the simple NLC converges well in the high-field phase right up to the transition, it diverges in the QSL phase and we need to modify it for the QSL. The physics of QSL is lost by having fluctuating spins at the boundary of the finite clusters. This is because every spin must be part of two tetrahedra in order to not mix different ice states by local fluctuations. But the boundary spins of a cluster belong to only one.

Thus, two boundary spins in the same tetrahedron can be flipped to go from one ice configuration to another already in order h^2. This is clearly incorrect.

In order to fix this problem we adopt a modified NLC scheme. We envisage local fluctuations in the interior of the QSL. Each cluster is divided into interior and boundary spins depending on whether or not the spin belongs to two or one tetrahedron in the finite cluster (See Fig. 2.1). The boundary spins feel additional longitudinal fields, coming from tetrahedra external to the cluster. It can be shown that the modified NLC in 5^{th} order gives perturbative properties correct to order h^8 except for the ring exchanges. However, these perturbative terms generate very small entanglement at small fields and ring exchanges are key to the physics of the QSL [16–18].

In order to capture the physics of ring exchanges one must consider clusters where tetrahedra form rings.

All the order one entanglement for small h arises from ring exchanges [18, 23]. This resonance can be destroyed by random fields, effectively killing the superposition and consequential entanglement. For studying this, cluster 9 consisting of six tetrahedra in a ring shown in Fig. 2.1 plays a crucial role.

In this cluster, each tetrahedron has two interior and two boundary spins. In our modified NLC, the cluster is embedded in a larger system. The Ising couplings of the spins external to the cluster result in longitudinal fields on the boundary spins of the cluster. The problem divides into different sectors corresponding to different boundary longitudinal fields. The key sector is one where in each tetrahedron one boundary spin has a positive and the other negative longitudinal field. At low energies this sector maps on to an effective $2-$level system given by the two alternating spin configurations along the hexagon of the cluster.

For a uniform system, this leads to an entanglement entropy for each tetrahedron of $\ln 2$ in the sector where the resonance occurs, and zero in all other sectors apart

from small perturbative corrections. Thus a sum over all tetrahedron gives $6 \ln 2$ in the resonating sector. The cluster has 730 total spin-ice states, 128 of which lead to the resonating state. If we assume that each one of the spin-ice states must be weighted with equal probability in the interior of the spin-ice as expected at the Rokhsar-Kivelson (RK) point [29], the weight of this cluster for the entanglement entropy per tetrahedron becomes $(6 \times 128/730) \ln 2$. This cluster has a count of one per site or two per tetrahedron. Thus, multiplying the weight by a factor of 2 gives an entanglement entropy for a tetrahedron in the thermodynamic system to be approximately 1.5. Our ED estimate for the low field entanglement entropy shown in Fig. 2.2 is less than 20 percent higher than this. One would expect the finite size calculation to be an over estimate because of a large number of short loops due to periodic boundary conditions in the small clusters. The comparison suggests that the resonating configurations are enriched relative to others by about 10 percent with respect to the RK point in the model. This is consistent with the Monte Carlo study of the ring-exchange model [18].

2.3 Results and Discussion

We now turn to the main focus of our study with random transverse fields. We present results from NLC and from ED of 16-site cluster. The Ising correlation sum and tetrahedron entanglement entropy from ED are shown in Fig. 2.3, where we see that an increase in the Ising correlation occurs concomitant with a decrease in local entanglement entropy. This shows that the confinement transition is associated with the lifting of degeneracy in the spin-ice subspace and leads to the development of Ising correlations [25]. Fig. 2.4 shows the distribution of single-tetrahedron entanglement entropies. One finds that as soon as one enters the confining phase the entanglement entropy develops a very broad distribution. Fig. 2.4 b shows a few cuts through the

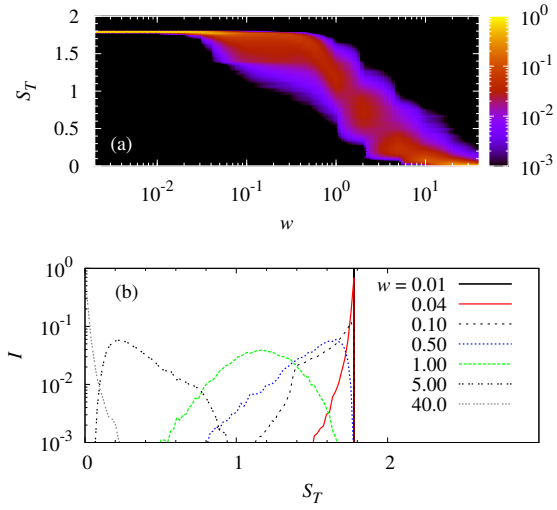

Figure 2.4: (a) Distribution of single-tetrahedron entanglement entropy S_T for $h = 0.1$ and various w values. The color scale represents the normalized intensity I. (b) Several cuts of the intensity I in (a) for selected w values. For $w = 0.01$, the intensity is a delta function shown as a solid black line at $S_T \sim 1.77$.

distribution function. In the QSL phase the entanglement entropy is essentially a delta function. In the confining phase it is very broad. There remains a substantial weight at the largest value until one gets into a paramagnetic phase around $w = 0.5$ after which the peak gradually moves to smaller values. However, the distribution remains very broad all the way up to very large randomness.

Note that ED cannot give the correct thermodynamic phase boundary because our cluster has loops of length 4 coming from periodic boundary conditions. These small loops lead to a phase boundary where w scales linearly with h.

To study the phase boundary for the thermodynamic system, we must use NLC and focus on cluster 9. The tetrahedron entanglement entropy in the resonating sector of cluster 9 is shown in Fig. 2.5. We see that the resonance, which leads to an entanglement of $\ln 2$ is killed with disorder. To further understand this, we turn to perturbation theory [27]. With disorder, the two-state problem for the cluster can be

described by an effective Hamiltonian

$$H_{\text{eff}} = a\sigma_x + b\sigma_z, \tag{2.8}$$

where $a = \frac{63}{256}h^6$, while

$$b = \frac{1}{48}\sum_t (h_{i1}^2 - h_{i2}^2)(h_{b1}^2 - h_{b2}^2), \tag{2.9}$$

where the sum is over all six tetrahedra. Here, h_{i1} and h_{i2} are the random-fields at the interior sites and h_{b1} and h_{b2} the random fields at the two boundary sites of the tetrahedra. Benton had argued [27] that the average degeneracy lifting perturbation should scale as wh^3. However, as seen from Eq. 8, there are two cancellations in each tetrahedron and b must vanish as w^2. We find that for Gaussian disorder it scales approximately as $14.7w^2h^2$. Calling the point $a = b$ as the transition point gives the phase boundary $w = ch^2$, with $c \approx 0.90$. This phase boundary is also shown in the inset of Fig. 2.5 and agrees well with our calculations, where the transition is determined by the horizontal dashed line corresponding to an S_T of 0.4165 as appropriate for $a = b$ in Eq. 7.

The suggested phase diagram is shown in Fig. 2.6 with QSL, Paramagnetic (PM) and Ising (I) phases. The latter is defined by enhanced Ising correlations. The PM-QSL boundary is indicated to be vertical. NLC results differ sharply from ED, even with non-zero w, around $h = 0.6$. Whether the phase immediately to the left of the boundary is a true thermodynamic QSL or an inhomogeneous Griffiths-like phase [64] with only pockets of QSL deserves further attention. The paramagnetic phase boundary at large w is roughly horizontal. Various properties collapse on a single scaling curve at larger w implying a local paramagnetic behavior. The confinement transition due to randomness, obtained in the finite cluster study from Ising correlations and entanglement entropy respectively are shown by open and closed triangles. The

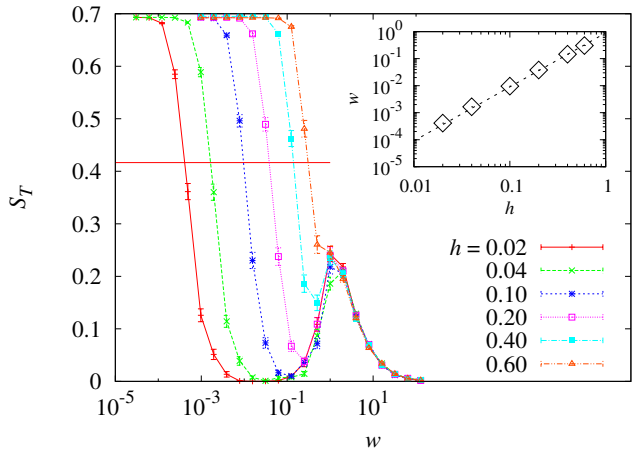

Figure 2.5: Single-tetrahedron entanglement entropy S_T obtained from cluster 9 as a function of width w for different h values. Each data point represents the average over 200 independent random gaussian field distributions The horizontal line corresponds to $S_T = 0.4165$. The inset shows the transition point obtained from these calculations (diamonds) and from perturbation theory (dashed line).

thermodynamic phase boundary, where hexagonal loop resonances are lost, is shown by diamonds and perturbation theory results are indicated by a dashed line. The nature of the phase transitions in presence of disorder deserves further field-theory consideration.

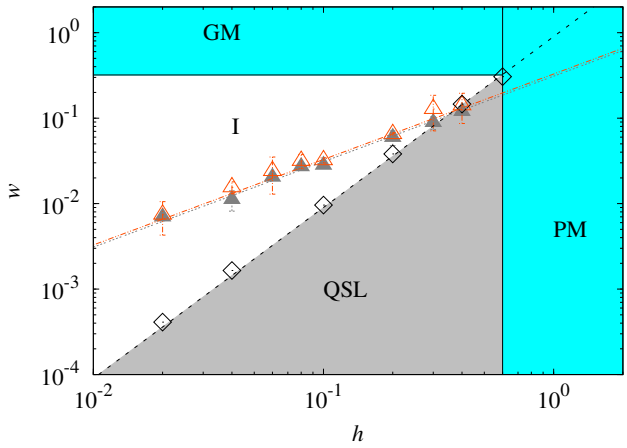

Figure 2.6: Suggested phase diagram for the random transverse-field Ising model with QSL, paramagnetic (PM) and Ising (I) phases. The triangles represent confinement phase boundary on the finite cluster. The diamonds are obtained from NLC and represent the phase boundary in the thermodynamic limit.

Chapter 3

Confinement, reduced entanglement, and spin-glass order in a random quantum spin-ice model

The results and discussion below are based on the article Phys. Rev. B **101**, 184423. This work was performed under the auspices of the U.S. Department of Energy by Lawrence Livermore National Laboratory under Contract DE-AC52-07NA27344, Document release number LLNL-JRNL-796781. This work is supported in part by National Science Foundation grant number NSF-DMR 1855111 and by grant number NSF-PHY 1748958.

We study an effective model derived perturbatively from a random transverse-field Ising model (RTFIM) on the pyrochlore lattice [26, 27]. The lattice consists of corner-sharing tetrahedra, with rare-earth spins at the vertices of the tetrahedron. The local Ising axis points along the line joining centers of neighboring tetrahedra, and crystal-field effects and strong anisotropy make it an effective two-level Ising sys-

tem [12]. RTFIM has been shown recently to be relevant for non-Kramers family of rare-earth pyrochlores [26–28]. Because two-fold degeneracy for eigenstates of non-Kramers ions is not guaranteed by time reversal symmetry, effective two-level models for these systems have random transverse-fields coming from quenched disorder. We had recently studied such a random transverse-field Ising models by exact diagonalization (ED) and numerical linked cluster expansion (NLC) methods [65], finding a phase diagram consisting of quantum spin-liquid (QSL), paramagnetic (PM), Ising (I) and Griffiths-McCoy (GM) phases. The systems studied were too small to establish whether the Ising phases had long-range spin-glass order.

Here, we use perturbation theory to derive an effective model starting from RTFIM, where spins are restricted to the spin-ice configurations [26, 27]. In the spin-ice subspace there are two types of random interactions. These are the Ising exchanges along the bonds and the cyclic ring-exchanges along the hexagonal loops of the model. Both these interactions are dependent on the configuration of random fields. The effective model can be studied up to larger systems (N=64 spins) allowing us to clearly establish the nature of the confined phases. We study a two-parameter family of models characterized by a mean value h and a width w for transverse-fields. As the width is increased at small h values, one observes two phase transitions. First, into a confined phase with long range spin-glass order and then into a partially deconfined phase, which we call a random resonating-hexagon (RRH) phase. In the latter, the resonating hexagons are randomly placed and leave a fraction of spins forming a frozen spinglass backbone. We believe the latter phase is a variant of cluster glass phases such as random singlet phase [66–69] that arise naturally in random quantum spin models. The implication of these findings to the rare earth pyrochlores will be discussed.

3.1 Models and Methods

We begin with the Hamiltonian for a transverse-field Ising model on the pyrochlore lattice [22–25]:

$$\mathcal{H} = J \sum_{<i,j>} \sigma_i^z \sigma_j^z - \sum_i h_i \sigma_i^x, \tag{3.1}$$

where the sigmas denote Pauli spin matrices, and J is the Ising exchange constant for nearest-neighbor interactions on the pyrochlore lattice. Note that the Ising axis varies from one sublattice to another and points along the line joining the centers of neighboring tetrahedron. The transverse fields h_i are assumed to be independent random variables at each site. In this work we will take the distribution of h_i to be Gaussian with mean h and standard deviation w, although details of the distribution are not critical to the study. Working in the limit of $J \to \infty$, restricts us to the Hilbert space of spin-ice states. In this space, the first perturbations that lift the degeneracy of ice states are fourth order terms that give rise to an Ising coupling on a bond given by strength proportional to $h_i^2 h_j^2$ [27]. Then, in 6th order perturbation theory we get the ring exchange term on the hexagons that can lead to a resonating QSL state.

In the spirit of effective models in a reduced subspace, like the $t - J$ model derived from the Hubbard model, we will now study the effective model in the spin-ice subspace:

$$\begin{aligned} \mathcal{H} = & \quad \tfrac{1}{48} \textstyle\sum_{<i,j>} h_i^2 h_j^2 \sigma_i^z \sigma_j^z \\ & - \tfrac{63}{256} \textstyle\sum_u K_u (\sigma_1^+ \sigma_2^- \sigma_3^+ \sigma_4^- \sigma_5^+ \sigma_6^- \ + \ h.c.), \end{aligned} \tag{3.2}$$

where h_i are quenched random variables with mean h and width w. The second sum is over all hexagons u of the lattice and $K_u = \prod_{i=1}^{6} h_i$ where h_i are the random fields at the six sites of the hexagon and σ_1 through σ_6 are the spin operators on the

hexagon in a cyclic order. Note that the cyclic term is only operative when the spins alternate along the hexagon, otherwise it destroys the state. From here onward we will study this effective model, which depends on two parameters h and w, and will allow for all values of h and w.

For $w = 0$, the Ising couplings do not cause any dispersion in the spin-ice subspace. Hence, the model reduces to the pure hexagonal ring exchange model [16, 17] simulated by several groups before [18, 19]. This model is known to have a quantum spin liquid ground state with emergent quantum electrodynamics and a collective photon excitation. Our goal is to study different phases of the model as a function of w and h.

We compute the following quantities:

1. The many-body band-width of the system, per spin, defined as

$$\frac{B}{N} = \frac{E_{max} - E_{min}}{N}, \tag{3.3}$$

where E_{max} is the energy of the highest energy state and E_{min} the energy of the lowest energy state for an N-site cluster.

2. Entanglement entropy of a tetrahedron of spins and their distribution: In a pure state, the von-Neumann entanglement entropy for subsystem A and its complement B is defined as

$$S_A = S_B = -\operatorname{Tr} \rho_A \ln \rho_A, \tag{3.4}$$

where ρ_A is the reduced density matrix for subsystem A. In this work, A is made up of the four spins belonging to any single tetrahedron. In the uniform system, it is easy to see that the tetrahedron entanglement entropy $S_T = \ln 6$. Let us label our basis states as $|\alpha, i>$, where α stands for spins inside the tetrahedron and i stands

for the spins outside. Then, a general state of the system can be expressed as

$$|\psi >= \sum_{\alpha,i} C_{\alpha,i} |\alpha, i > .$$

The reduced density matrix for the tetrahedron ρ_T has matrix elements

$$\rho_{T\,\alpha,\beta} = \sum_i (C_{\alpha,i})^* \; C_{\beta,i}.$$

It must be diagonal because, for two state $|\alpha, i>$ and $|\beta, i>$ to both lie in the spin-ice subspace, one must have $\alpha = \beta$. Furthermore, the uniform system has sublattice symmetry and all 6 states are related by a permutation of sublattices. Hence, as long as there is a non-degenerate ground state, all 6 diagonal matrix-elements of the reduced density matrix must be equal implying $S_T = \ln 6$. Our earlier exact diagonalization studies of 16 and 32 site systems [65] showed that, in the full random transverse-field model, this entropy remains very close to $\ln 6$, despite virtual dressing of the spin-ice states due to perturbative fluctuations. Only when one is near the confinement transition one sees deviations from this value.

3. Ising correlation function and correlation sum

$$C_{ij} = [\langle \sigma_i^z \sigma_j^z \rangle^2 \,], \tag{3.5}$$

$$C_{zz} = [\frac{1}{N} \sum_{i,j} \langle \sigma_i^z \sigma_j^z \rangle^2 \,], \tag{3.6}$$

where the angular brackets refer to ground state averages and square brackets to an average over the distribution of random fields. Note that we have normalized the correlation sum such that in a system with long-range (random) order the correlation sum C_{zz} should scale as N.

4. Inverse participation ratio in the many-body space defined as

$$IPR = \frac{1}{\sum_i a_i^4}, \tag{3.7}$$

where a_i are the coefficients of the ground state wavefunction in the Ising basis. In the quantum spin-ice phase this quantity should be of order D, where D is the dimension of the spin-ice space, whereas in an equal admixture Cat state of two Ising configurations, it should equal 2.

3.2 Numerical Results

We study finite clusters with periodic boundary conditions. We have looked at clusters of size 32, 40, 48 and 64. To carry out the calculations we first pick a configuration of random fields for each site from a Gaussian random distribution with mean h and uncertainty w. This allows us to determine the Ising couplings for all the bonds, as well as strength of the ring exchange for each hexagon. The ground state is then obtained by the Lanczos method. We typically include 100 to 400 different field configurations to average over random configurations. Variations from different field configurations allow us to determine the statistical error bars.

With only the ring exchanges as the off-diagonal terms, this model is known to partition into disjoint subspaces. We first determine all the disjoint parts of the Hilbert space and then obtain the ground state in each subspace. The overall ground state is obtained by comparing energies in different subspaces. In the QSL phase, the ground state typically lies in the largest connected subspace but this is not necessarily true. When the ground state is in a subspace where a state and its time reversed partner are disconnected, there must be two degenerate ground states. Since, the original transverse field model does not have a disconnected Hilbert space, in this case, we take as our ground state the symmetrized linear superposition of the two.

For $N = 64$ case, the total spin-ice subspace has dimensionality $2,249,370$ whereas the largest disjoint sector has dimensionality $194,640$.

We present the results for the 64 site cluster here, and those for smaller system sizes can be found in the Appendix A. In Fig. 3.1, the many-body band-width of the system per site, B/N, is shown. It is independent of width w in the QSL phase and depends on h as h^6 due to the ring exchange term. This is why the figures start off as horizontal. In the perturbative regime, after the first phase transition the bandwidth varies with w as w^2 as known from previous studies using NLC [65] for RTFIM. This follows from the fact that within each tetrahedron the maximum difference in the energy between any two spin-ice states goes as w^2h^2, which at constant h varies as w^2. This behavior is indicated by a dashed line. For large w the bandwidth must scale as w^6. This just follows from dimensional analysis. This scaling behavior is also indicated by a dashed line. It is clear that at the largest w and h studied, we are deep in this limit.

In Fig. 3.2, we show the average entanglement entropy S_T for a tetrahedron. It is averaged over the tetrahedron in a cluster as well as over the distribution of random fields. Two phase transitions are clearly seen in the plot at small $h = 0.1$, which turns into a single phase transitions at larger h. It equals $S_T = \ln 6$ in the QSL phase, as shown earlier from general considerations. The entanglement changes at the transitions dramatically within a small parameter range. In the intermediate phase it approaches $\ln 2$ implying that the state is reduced to a Cat state, that is a superposition of two Ising states related by spin inversion, with only global $\ln 2$ entropy and there is negligible quantum fluctuation around that state. The error-bars from the disorder averaging are small. At very large w, the entanglement entropy approaches a value somewhat below $2 \ln 2$. This is an indication of a phase which differs from the quantum spin-liquid but still has significant amount of quantum fluctuations. We will call this phase a random resonating hexagon (RRH) phase.

More discussion on this phase will be provided in the next section.

Fig. 3.3 shows a distribution of entanglement entropies. Inside the quantum spin-liquid phase, the entropy is very sharply defined. As we showed rigorously earlier, in this phase, the entanglement takes the maximal value of $S_T = \ln 6$. In the transition regions as well as in the random resonating-hexagon (RRH) phase at large w the entropy distribution becomes very broad. In the RRH phase, there is still a well-defined peak in the distribution near $S_T = 2 \ln 2$. This will help us further understand the properties of the RRH phase.

In Fig. 3.4, the Ising correlation sum is shown. The correlation sum is extensive in both phases other than the QSL phase as shown in Fig. 3.5. In Fig. 3.5, we have plotted C_{zz}/N as a function of N. The fact that it is not decaying as a function of N implies that in these phases there is long-range Ising correlation. In the middle of the intermediate phase, which we identify as Ising spin-glass phase, C_{zz}/N is close to its maximum allowed value. In other words, all the spins are fully correlated with each other. This further confirms that there is very little quantum fluctuation in this state. This is not surprising as Ising couplings dominate over ring exchanges in this regime. The fact that C_{zz} is proportional to N in the RRH phase implies that at least a subset of spins must be long-range correlated in this phase also. In other words, there is a backbone of long-range Ising ordered spins. This observation would allow us to further understand the RRH phase in the next section.

In Fig. 3.6, the inverse participation ratio is plotted. In the spin-glass phase it is only slightly larger than 2, further confirming that only two Ising ordered states are contributing to the ground state in this phase. In the other two phases, IPR is strongly size dependent. In the QSL phase it must scale with the dimension of the Hilbert space, and hence must be exponential in N. This is, indeed, found to be true. In the random resonating-hexagon phase also it grows with the size of the system. We have found that it varies exponentially with N as a^N, but with a value of a only

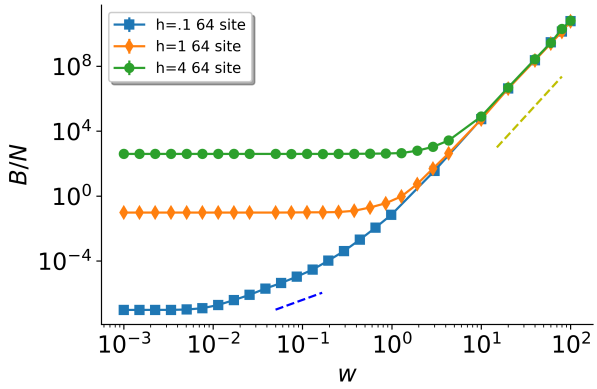

Figure 3.1: The total bandwidth of the spin-ice subspace per spin plotted on a log-log scale for the 64 site cluster. The yellow dashed line represents the scaling as w^6 in the RRH phase, and the blue dashed line represents the ISG scaling as w^2 in the intermediate phase.

slightly larger than unity ($a \approx 1.04$). This will allow us to further understand the nature of the RRH phase in next section.

The fact that the spin-glass and random resonating hexagon phases have long-range Ising order implies that there must be a phase transition between QSL and those phases. It cannot be a smooth crossover. The phase transition can be first or second order. We have not seen evidence for finite size scaling as one might expect at a second order transition. Instead the transition point is weakly dependent on size. The entire transition region shifts weakly as one goes from one size to another. This is, at least partially, because the system sizes studied are too small, and the shape dependence of the different clusters is significant and makes it difficult to say more about the nature of the phase transition.

3.3 Discussions: Phase Diagram

Our numerical results clearly establish three phases in the model separated by phase transitions. As shown in the phase diagram in Fig. 3.7 these are the quantum spin-liquid (QSL), the Ising spin-glass (ISG) and the random resonating-hexagon (RRH)

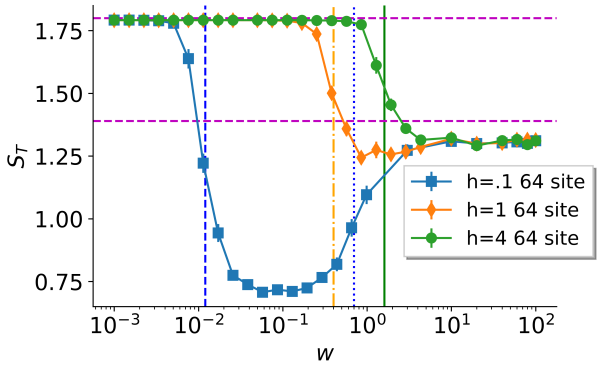

Figure 3.2: Entanglement entropy for a tetrahedron of spins, S_T, for different parameters, for the 64 site cluster. Vertical lines represent phase transitions. The blue dashed line represents the QSL to ISG phase transition for $h = .1$, the orange dashed-dot line represents the QSL to RRH transition for $h = 1$, the blue dotted line represents the ISG to RRH transition for $h = .1$, and the green solid line represents the QSL to RRH transition for $h = 4$. The horizontal dashed lines represent $\ln 6$ and $2 \ln 2$ respectively.

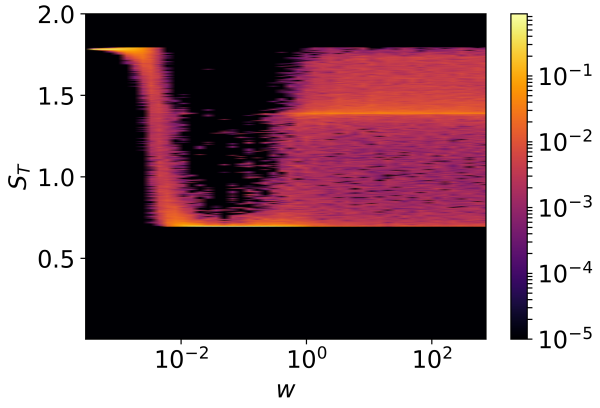

Figure 3.3: Distribution of entanglement entropies for different values of w for $h = 0.06$.

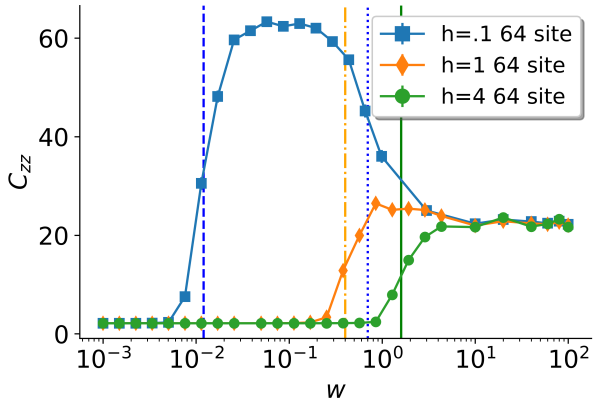

Figure 3.4: Ising correlation sum in different parameter regions for the 64 site cluster. Vertical lines represent phase transitions. The blue dashed line represents the QSL to ISG phase transition for $h = .1$, the orange dashed-dot line represents the QSL to RRH transition for $h = 1$, the blue dotted line represents the ISG to RRH transition for $h = .1$, and the green solid line represents the QSL to RRH transition for $h = 4$.

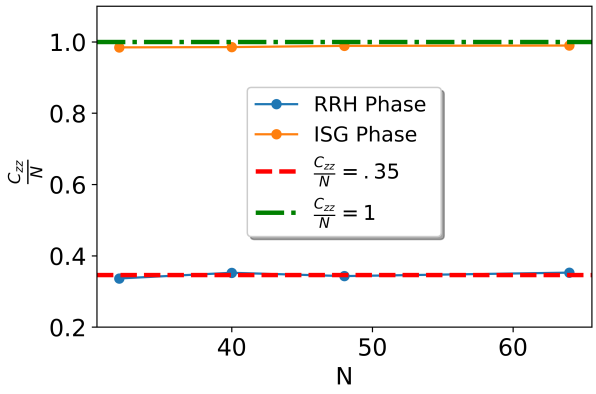

Figure 3.5: Scaling of Ising correlation sum with N, the size of the system.

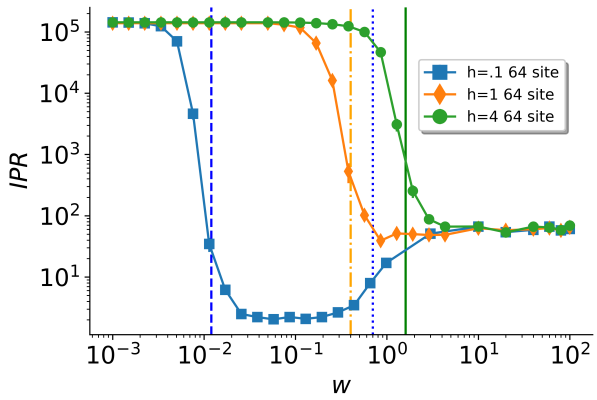

Figure 3.6: Inverse Participation Ratio for different parameters for the 64 site cluster. Vertical lines represent phase transitions. The blue dashed line represents the QSL to ISG phase transition for $h = .1$, the orange dashed-dot line represents the QSL to RRH transition for $h = 1$, the blue dotted line represents the ISG to RRH transition for $h = .1$, and the green solid line represents the QSL to RRH transition for $h = 4$.

phases. These phases are separated by sharp transition regions. When there is no disorder, that is $w = 0$, the model is in the QSL phase for all values of h. This must be separated from other phases by a thermodynamic phase transition as the other phases have long range Ising order, and hence a broken Z_2 symmetry in the thermodynamic limit. At small h and w, the middle of the Ising spin-glass phase has negligible quantum fluctuations. This is not surprising as the Ising couplings arise in lower order of perturbation theory than the ring exchange term [27, 65]. Hence they totally dominate, and as argued in the previous chapter 2 all the ring terms are frozen out by disorder. In our perturbative model, at large h, the Ising couplings become negligible and the model becomes a random ring-exchange model. In this case one has a direct transition from the quantum spin-liquid to a random resonating hexagon phase.

The transition is not a simple level crossing as clearly the transition region is broad. However, we do not see evidence for crossing of physical properties for different sizes as expected at a critical transition. Instead there is a weak size dependence of the transition point. Yet, the transition region is characterized by substantial fluc-

tuations, and the entanglement entropy develops a broad distribution there. Hence, we conclude that the transition maybe weakly first order. Savary and Balents [26] suggested a weakly first order confinement transition due to randomness even when no spin-glass order develops on the other side. The development of an additional order is even more likely to make it first order. However, the nature of the phase-transitions in the model, deserves further consideration.

The novel phase, found in our study, is the random resonating-hexagon (RRH) phase. This phase has a broad distribution of entanglement entropy with a peak near $2\ln 2$. The many-body inverse participation ratio suggests that it still grows exponentially with system size, although very slowly 1.04^N. Moreover, this phase has Ising correlation sum which scales as N implying long-range order. This implies that there must be a backbone of spins that have long-range Ising correlations. To understand this phase, we focus on large-h, where our model reduces to a random ring-exchange model. The ground state of this model can be understood along the lines of real-space renormalization group (RSRG) approaches to understanding random quantum spin problems [66–69]. As the distribution of couplings becomes very broad (being a product of 6 field terms), one can first pick out the strongest hexagon and make it into a resonating cluster. The strong resonance of one hexagon makes these six spins ineligible for additional entanglement, and can render neighboring spins frozen into certain configurations as otherwise they would interfere with this resonance [65]. This resonating cluster is like a singlet formation in a random-singlet phase, except it involves six spins and is unrelated to any SU(2) symmetry. Then one can pick out the next strongest resonating hexagon. When this process is continued, it will lead to a random configuration of hexagons placed in the lattice and it can leave a backbone of spins that must be fixed, apart from an overall spin-inversion, in order to maintain compatibility with the resonance in the hexagons and be in the spin-ice subspace. Our numerical results suggest that the backbone of Ising ordered spins is percolating

and has a finite fraction of spins. Otherwise the Ising correlation sum would not scale linearly with number of spins.

The participation ratio should scale as 2^{N_c}, where N_c is number of resonating clusters. The calculated value 1.04^N implies one resonating cluster per about 16 spins. This further confirms that some fraction of spins are not participating in resonances and are forming a frozen backbone. Furthermore, one would expect the phase to have a large distribution of entanglement entropies with a substantial weight around $2\ln 2$, corresponding to the four spins in a tetrahedron dividing into two groups of two and participating in two independent resonances, one of them being the Ising backbone, which in a finite system will form a Cat state and also add $\ln 2$ to entanglement entropy.

In the random transverse-field Ising model (RTFIM), such an RRH phase can only arise at intermediate values of disorder w of order unity and h not too large [65]. We know that too large an h in the RTFIM model leads to a different confining phase with a condensation of spinons and the system moves away from the spin-ice subspace altogether. That physics is absent in the effective model studied here, since the model is defined in the restricted spin-ice subspace. Also, if the disorder w becomes much larger than order one in RTFIM, one would once again enter a local phase where the spins simply point along the local random fields and will no longer be in the spin-ice subspace. Thus, this second limit is also absent in the effective model studied here. The comparison of our results with the earlier ED study of the RTFIM model suggests that some aspects of the RRH phase is possible in the RTFIM. However, the Ising ordered backbone may be only short-range correlated in RTFIM due to the effect of the local transverse fields.

It is interesting to consider this study from the perspective of rare-earth magnetic pyrochlore materials, where RTFIM has been argued to be relevant [26–28]. First of all, our work implies that if $h = 0$ and one only has weak random fields, the system

will be in a frozen spin-glass phase. A variety of measurements such as NMR or μSR can easily confirm that. Indeed restricted subspace generally promotes spin-glass order [70]. However, if disorder becomes a fraction of J, then one is away from the perturbative regime and the possibility of random resonating-hexagon phase becomes likely. While not a true QSL, such a phase has a lot of quantum fluctuations and local entanglement and should show interesting power-law temperature, magnetic field and frequency dependence [68, 69] in various responses. These can be dominated by just the behavior of single hexagons, and can be easily calculated. Indeed this physics can survive up to very large randomness.

For the material $Pr_2Zr_2O_7$, it has been argued [27, 28] that the width of the random-field distribution can be much larger than the Ising couplings. The actual distribution of random-fields, in the materials, was found to not be Gaussian but Lorentzian. We have studied a Lorentzian distribution as well. It does not qualitatively change the phases discussed here but makes numerical data more noisy due to the tails of the Lorentzian distribution. It is clear from our work that significantly reduced randomness is needed to obtain a QSL phase. It would be interesting if evidence for local resonating hexagons is observed in the experimental systems.

In order to obtain a true U(1) QSL phase, it is not enough to just reduce the strength of the disorder or w. It is important to have a uniform component of the transverse-field that is at least of order the randomness. The kind of impurities or imperfections that can lead to this deserves further attention from a materials point of view. It is more likely that when non Kramers ions have two nearby non-degenerate crystal-field states that it can then be modeled as two level systems in a uniform transverse-field. If such a system still has spin-ice physics, it would be a good candidate for a QSL. Another possibility is that disorder is correlated over lengths much larger than the lattice constant for example due to strain. In that case, the system can behave effectively as having a uniform field in any region.

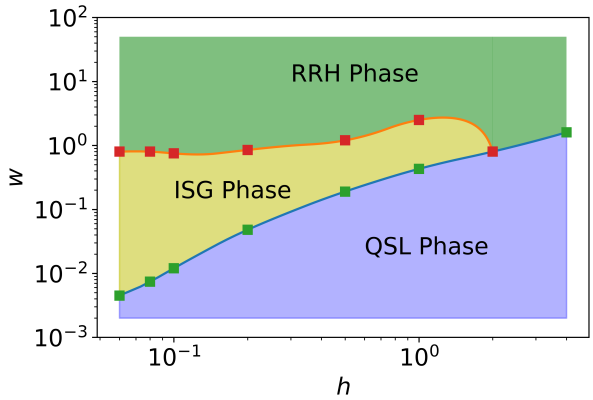

Figure 3.7: Phase diagram of the perturbative model studied here in the $w - h$ plane consisting of quantum spin-liquid (QSL), Ising spin-glass (ISG) and random resonating hexagon (RRH) phases. We expect the perturbative model to agree with the RTFIM when both h and w are much less than unity.

Chapter 4

Photo-induced tunable Anomalous Hall and Nernst effects in tilted Weyl Semimetals using Floquet theory

4.1 The model Hamiltonian

The results and discussion below are based on the article Phys. Rev. B **98**, 205109.

In this chapter, we consider the effects of a circularly polarized beam of laser on the Floquet transport properties of Weyl semimetals. Consider a time reversal symmetry breaking tilted Weyl semimetal with two Weyl nodes of opposite chirality. The linearized Hamiltonian for such a system around each Weyl node $s = \pm$ is given by [71]

$$H_s = \hbar C_s(k_z - sQ) + s\hbar v\boldsymbol{\sigma} \cdot (\boldsymbol{k} - sQ\boldsymbol{e}_z) \tag{4.1}$$

where C_s is the tilt parameter, which also is associated with the type of the Weyl

point. Here, v denotes the Fermi velocity in the absence of the tilting term, $2Q$ is the distance between the Weyl points in momentum space along $\boldsymbol{e}_z$, and $\boldsymbol{\sigma}$ is the vectorized Pauli matrix.

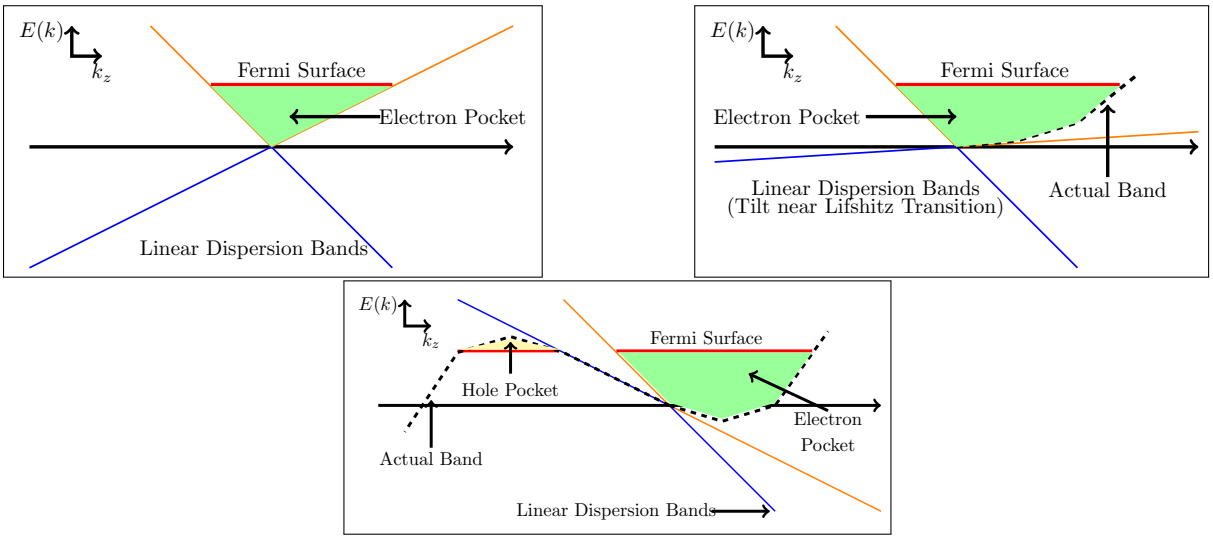

Figure 4.1: (a) Fermi surface relative to Weyl node for type-I WSM away from the Lifshitz transition. The upper band is in orange and the lower band is in blue. (b) Type-I WSM - failure of the linearized model near the Lifshitz transition. (c) Fermi surface relative to Weyl node for type-II WSM showing how the linearized model can give us qualitatively correct results by imposing a physical momentum cutoff since the actual band structure (dashed lines) have finite electron and hole pockets.

For type-I WSMs shown in Figs. 4.1(a) and 4.1(b), the blue and orange lines indicate the linearized band structure near the Weyl nodes (with their meeting point being the Weyl point), the red lines indicate the Fermi energy or highest occupied level, and the green pockets indicate the zone filled by electrons. It is clear from Fig. 4.1(b) that as we increase the tilt the higher order momentum terms in the Hamiltonian become relevant and while the actual electron pocket size is finite as indicated by the the green zone (the dashed boundary corresponds to the actual band structure with higher order corrections), the linearized model predicts infinite electron pocket sizes. Fig. 4.1(c) shows that for type-II WSMs, past the Lifshitz transition, a physical momentum cutoff needs to be introduced since the true band structure admits only finite pocket sizes.

4.2 Circular polarized light and Floquet theory

We use a polarized beam of form $E(t) = E_0(\cos\omega t, -\sin\omega t)$, where E_0 and ω are the amplitude and frequency of the optical field. The Pierels substitution leads to $\hbar k_i \to \hbar k_i + eA_i$, where $\vec{A}(t+T) = \vec{A}(t)$, with $T = 2\pi/\omega$ as the periodicity. The full time-dependent Hamiltonian has the form [72–77]

$$H_s(k,t) = H_0(k) + \mathcal{V}_s(t) \tag{4.2}$$

with $H_0(k) = H_s = \hbar C_s(k_z - sQ) + s\hbar v\boldsymbol{\sigma}\cdot(\boldsymbol{k} - sQ\boldsymbol{e}_z)$ and $\mathcal{V}_s(t) = s\hbar\nu A_0(\sigma_x \sin\omega t + \sigma_y \cos\omega t)$. In the HFL, we map to a time-independent problem (See Appendix B part 1) by using Floquet theory [78] and employ the HFE [55, 77, 79–82].

The effective time independent Hamiltonian for our system can be obtained as,

$$\begin{aligned} H_F^s = {} & \hbar C_s[k_z - s(Q+\Delta)] + s\hbar v\boldsymbol{\sigma}\cdot[\boldsymbol{k} - s(Q+\Delta)\boldsymbol{e}_z] \\ & + s\hbar C_s\Delta, \end{aligned} \tag{4.3}$$

where $\Delta = \frac{\hbar v A_0^2}{2\omega}$, is the contribution of the radiation field. It is to be noted here from eqn.(4.3) that the form of the effective Hamiltonian is similar to the original Hamiltonian in eqn.(4.1), with the Weyl nodes being further displaced by a distance 2Δ in momentum space. We restrict to the inversion symmetric case, $sC_s = C, \forall s = \pm$, and so there is an overall shift in the total energy of both nodes by an amount equal to $\hbar C\Delta$.

4.3 Floquet-Matsubara formalism

In order to analyze the Nernst conductivities [83] and anomalous thermal Hall conductivities [84–86] in both the regimes of WSMs, we can now use the Kubo formalism modified for Floquet theory [87–89]. The modification to the standard form of the Kubo formula, used to calculate the time-averaged conductivity tensor for periodically driven systems, lies in the use of Floquet states, quasi-energies, and the time averaging integral. For a Hamiltonian linear in momentum, this can be simplified to the form (for the detailed derivation of the modified Kubo formula for a Hamiltonian linear in momentum see Appendix B part 2)

$$\sigma_{ab} = i \int \frac{d\mathbf{k}}{(2\pi)^3} \sum_{\alpha \neq \beta} \frac{f_\beta(\mathbf{k}) - f_\alpha(\mathbf{k})}{\epsilon_\beta(\mathbf{k}) - \epsilon_\alpha(\mathbf{k})} \times \frac{\langle e_\alpha(\mathbf{k})|J_b|e_\beta(\mathbf{k})\rangle \langle e_\beta(\mathbf{k})|J_a|e_\alpha(\mathbf{k})\rangle}{\epsilon_\beta(\mathbf{k}) - \epsilon_\alpha(\mathbf{k}) + i\eta}, \tag{4.4}$$

which resembles exactly the standard form of the Kubo formula where $J_a(b)$ represents the current operator, the e_α's represent the states of the effective Floquet Hamiltonian, and the ϵ's represent the corresponding quasi-energies. The f_α's represent the occupations which in general could be non-universal in systems which are out of equilibrium. However, the steady-state occupations resemble the Fermi-Dirac distribution with the quasi-energies for a certain class of system-bath couplings [90], and our results are valid for such cases.

In general, Mott's relationship defines the anomalous thermal Hall and Nernst

conductivities as [83–86],

$$\alpha_{xy} = eLT\frac{d\sigma_{xy}}{d\mu}, \quad K_{xy} = LT\sigma_{xy}, \tag{4.5}$$

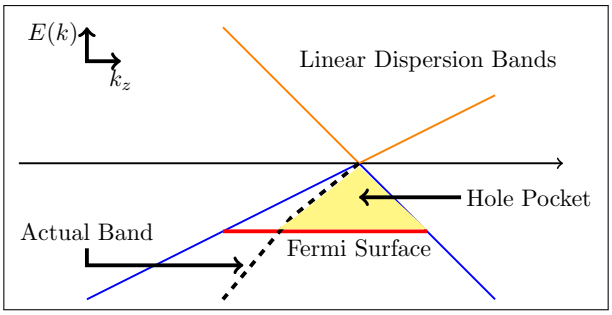

Figure 4.2: Fermi surface relative to Weyl node for type-I WSM showing that on lowering the effective chemical potential we eventually get incorrect estimates of the hole pocket size.

where $L = \pi^2 k_B^2/3e^2$ is the Lorentz number, e is the electronic charge, and k_B is the Boltzmann constant. It is to be noted here that the electric field, sourced by the small d.c. bias needed to measure transport properties in the linear response regime, has been suppressed in eqn.(4.2), and we account for it in the conductivity tensor σ_{xy} calculation, done using the Matsubara approach (see Appendix B part 3).

4.4 Thermal Hall and Nernst effects in type-I WSMs

From eqn.(4.5), the Nernst and thermal Hall conductivities in the $T \to 0$ limit for a type-I WSM, are obtained as,

$$\begin{aligned} \alpha_{xy} &= \frac{-ek_B^2 TC}{18\hbar^2 v^2} \\ K_{xy} &\approx \frac{k_B^2 T}{6\hbar}\left[\Big(Q+\Delta\Big) - \frac{C(\mu - C\Delta)}{3\hbar v^2}\right]. \end{aligned} \tag{4.6}$$

Firstly, we note that K_{xy} varies smoothly around the point $\mu = C\Delta$, and that

setting $\Delta = 0$ gives us back the results in [37]. We rewrite the Hall conductivity in a suggestive manner which shows that the Hall conductivity grows monotonously with Δ.

$$K_{xy} = \frac{k_B^2 T}{6\hbar}[Q - \frac{\mu}{3\hbar v^2}C] + \frac{k_B^2 T}{6\hbar}[1 + \frac{C^2}{3\hbar v^2}]\Delta = K_{xy}^0 + K_{xy}^\Delta, \tag{4.7}$$

where K_{xy}^0 is the Hall conductivity in the absence of irradiation and K_{xy}^Δ is the positive contribution of the laser field. Since both nodes get an energy boost of $C\hbar\Delta$, the chemical potential which shows up in the Fermi-Dirac distribution function is offset by it, and it's instructive to think of this as fixing the chemical potential and moving the band structure for both nodes vertically. It's clear that as we increase the amplitude of the radiation field, the effective chemical potential $\mu - C\Delta$ decreases and ultimately becomes negative. Since moving the effective chemical potential further down amounts to increasingly incorrect hole pocket size estimations in the linearized model (Fig. 4.2), with the dashed line indicating the actual band structure, one might worry about the limit of validity of the result. However, the free carrier contribution is a second order effect, supressed by $\frac{C^2}{v^2}$, and the dominant contribution to Hall conductivity comes from the shift in node spacing, i.e. Δ, which is part of the vacuum contribution, known to be cutoff independent. Thus we can conclude that the Hall conductivity grows with the amplitude of the irradiation field far away from the linear regime. In Figs. 4.3(a) & (b), the anomalous thermal Hall conductivity is plotted in units of $(k_B^2/\hbar)$ as a function of optical frequency and temperature.

Since the linearized model predicts a linear dependence of K_{xy} on μ in the type-I regime, the Nerst conductivity is predictably constant and remains unchanged by the optical field.

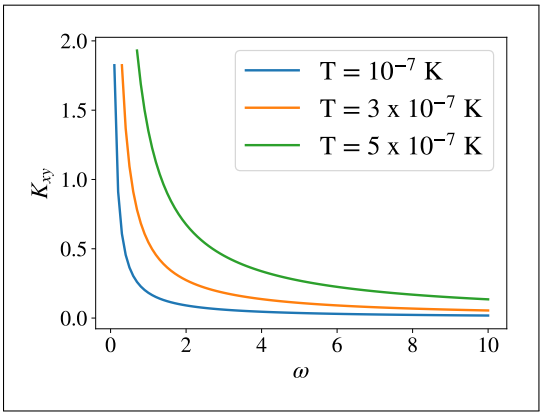

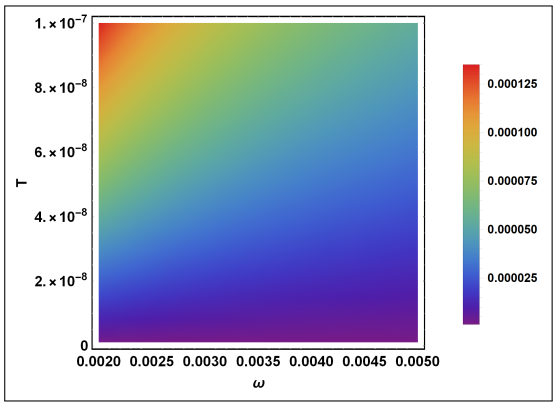

Figure 4.3: (a) Variation of thermal Hall conductivity with optical frequency for three different values of the temperature for type-I WSM. The frequency axis is in units of 10^{12} Hz. (b) Variation of thermal Hall conductivity with optical frequency and temperature for type-I WSM. The frequency axis is in units of 10^{16} Hz, and the temperature axis is in units of $10^4 K$.

4.5 Thermal Hall and Nernst effects in type-II WSMs

The Hall and Nernst conductivities for type-II WSMs are presented below.

$$\alpha_{xy} = -\frac{ek_B^2 Tv}{6\hbar^2 C^2}\left[\ln\left(\frac{C^2\Lambda}{v(C\Delta-\mu)}\right)-1\right]$$
$$K_{xy} = \frac{ek_B^2 Tv}{6C\hbar}\left[\left(Q+\Delta\right)-\frac{(\mu-C\Delta)}{\hbar C}\ln\left(\frac{C^2\Lambda}{v(C\Delta-\mu)}\right)\right]. \tag{4.8}$$

Considering the expression for K_{xy}, which depends nonlinearly on the chemical potential, it is clear that it decreases for increasing Δ, and we find that changing the amplitude of the photon field affects the Nernst conductivity, which decreases logarithmically with increasing Δ. For the correct qualitative description of the transport coefficients, the momentum cutoff needs to be modified for increasing A_0 .

Finally, while the physical momentum cutoff is difficult to estimate without using a non-linear model, we can provide a way to experimentally verify our findings independent of the cutoff. Notice that we can eliminate the Λ dependence from eqns.(4.8) to get:

$$[-\frac{6\hbar C}{k_B^2 T v} K_{xy} + Q + \Delta]\frac{\hbar C}{C\Delta - \mu} = \frac{6\hbar^2 C^2}{e k_B^2 T v}\alpha_{xy} + 1 \tag{4.9}$$

Figs. 4.4(a) & 4.4(b) show the anomalous Hall conductivities for a range of Nernst conductivities and driving frequency at fixed temperature, as defined by eqn.(4.9).

A pump-probe experiment (see Appendix B part 4) is a potential candidate setup for the verification of the results stated here. Such setups have been used to create stable WSMs from Dirac metals and allow for the steering of Weyl points [91]. Since the timescale for amplitude modulation is orders of magnitude larger than the oscillation of the field, the position of the Weyl nodes is dictated by the frequency of the optical field, with small variations due to amplitude modulation. Similar experiments have been also proposed for the transport properties of other driven topological phases [92–98]. The effective Floquet band close to the Weyl node can be experimentally confirmed using time-resolved photo emission spectrosocopy [82, 91, 99, 100].

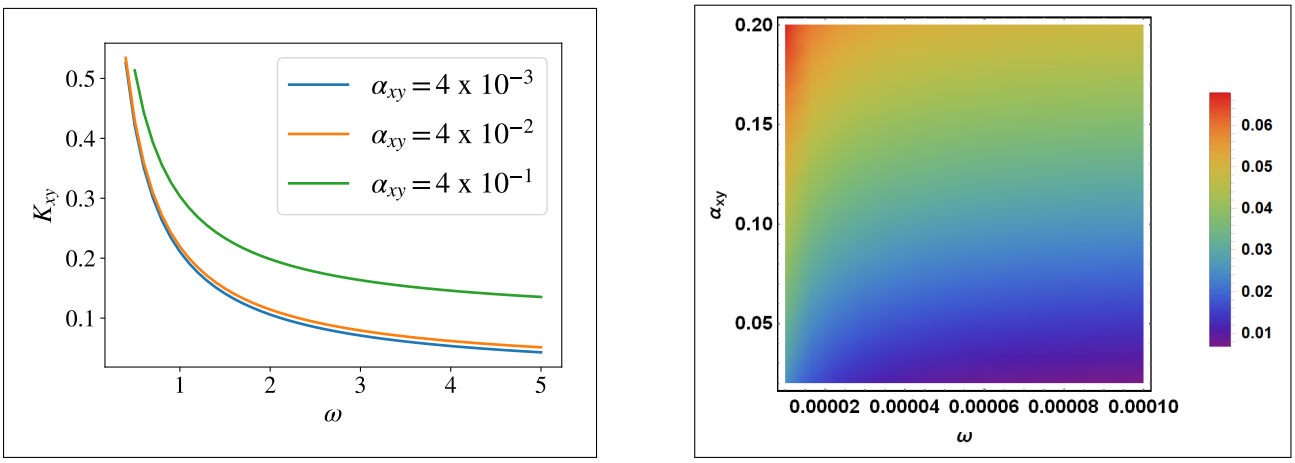

Figure 4.4: (a) Variation of thermal Hall conductivity with optical frequency for three different values of Nernst conductivity for type-II WSM. The frequency axis is in units of 10^{10} Hz. (b) Variation of thermal Hall conductivity with optical frequency and Nernst conductivity for type-II WSM. The frequency axis is in units of 10^{16} Hz.

Chapter 5

Thermo-electric transport properties of Floquet multi-Weyl Semimetals

The results and discussion below are based on the article Phys. Rev. B **102**, 014307.

5.1 Effective Floquet Hamiltonian

In this chapter, we consider the effects of a circularly polarized beam of laser on the Floquet transport properties of Weyl semimetals. The low energy Hamiltonian for a multinode WSM of monopole charge n near each Weyl point is given by[52, 101, 102]

$$H^s_{\mathbf{k}} = \hbar C_s(k_z - sQ) + s\hbar\alpha_n \boldsymbol{\sigma}\cdot(\mathbf{n_k} - s\mathbf{e}) \tag{5.1}$$

The derivation of the above model is shown explicitly in the SI, Sec. I. Here, $s = \pm$ indicates the chirality of nodes, $\mathbf{n_k} = [k^n_\perp \cos(n\phi_{\mathbf{k}}), k^n_\perp \sin(n\phi_{\mathbf{k}}), \frac{vk_z}{\alpha_n}]$. $\mathbf{e} = (0, 0, Q)$, and $2Q$ is the separation between two Weyl nodes. $\boldsymbol{\sigma} = [\sigma_x, \sigma_y, \sigma_z]$ is the vectorized Pauli matrix, and α_n is the mWSM coupling which reduces to the Fermi velocity

v when $n = 1$. We define the $x - y$ plane azimuthal angle $\phi_{\mathbf{k}} = \arctan(\frac{k_y}{k_x})$, and the in-plane momentum $k_\perp = \sqrt{k_x^2 + k_y^2}$. The Hamiltonian (5.1) represents the two Weyl nodes $(0, 0, \pm Q)$, located at the same energy and separated by a distance $2Q$, while C_s indicates the tilt parameter associated with s Weyl node. Type-I mWSMs corresponds to $|C_s|/v \ll 1$ while for type-II mWSMs we have $|C_s|/v \gg 1$. We restrict to the inversion symmetric tilt given by $sC_s = C$. We cast the above Hamiltonian in matrix notation:

$$H^s_{\mathbf{k}} = \begin{bmatrix} \hbar C_s(k_z - sQ) + s\hbar v(k_z - sQ) & s\hbar\alpha_n(k_x - ik_y)^n \\ s\hbar\alpha_n(k_x + ik_y)^n & \hbar C_s(k_z - sQ) - s\hbar v(k_z - sQ) \end{bmatrix}. \tag{5.2}$$

Hereafter, we use Natural units and set $\hbar = c = k_B = 1$. We now examine the effect of circularly polarized light on the mWSM. Under the influence of a periodic optical driving with electric field of frequency ω, $\mathbf{E}(t) = E_0(-\cos\omega t, \sin\omega t, 0)$, the Hamiltonian transforms via the Pierel's substitution $k_i \to k_i - A_i$, where the vector potential is given by $\mathbf{A}(t) = \frac{E_0}{\omega}(\sin\omega t, \cos\omega t, 0)$, in the Landau gauge. The gauge dependent momenta transform as $k_x \to k'_x = k_x - A_0 \sin\omega t$,

$k_y \to k'_y = k_y - A_0 \cos\omega t$,and $k_z \to k'_z = k_z$. The driving amplitude of the vector potential is related to the amplitude of the electric field by $A_0 = \frac{E_0}{\omega}$. Considering the fact that $(k'_x \pm ik'_y)^n = \sum_{m=1}^{n} (k_\perp e^{\pm i\phi})^{n-m} (A_0)^m e^{\pm im(\frac{\pi}{2} - \omega t)}\ {}^nC_m$, where ${}^nC_m = \frac{n!}{(n-m)!m!}$ represents the combinatorial operator, the time dependent Hamiltonian takes the form

$$\begin{aligned} H^s_{\mathbf{k}}(\mathbf{A}, t) &= s\sigma_+(k'_x + ik'_y)^n + s\sigma_-(k'_x - ik'_y)^n \\ &+ C(k_z - sQ) + v(k_z - sQ)\sigma_z \end{aligned} \tag{5.3}$$

Solving the problem with a time-dependent potential may be out of the reach of analytical tractability. Instead, we resort to using Floquet's theorem and the extracting the sub-leading order term in the high frequency van-Vleck expansion, to obtain a closed form expression for the effective Hamiltonian $H^F_{\mathbf{k}}$.

We note that one can numerically solve an extended Floquet Hamiltonian, defined in the Hilbert space $\mathcal{T} \otimes \mathcal{H}$ (with $\mathcal{H}$ being the Hilbert space of static Hamiltonian and $\mathcal{T}$ being the Hilbert space associated with multi-photon dressed states), to obtain the quasi-states and quasi-energies [103]. From mathematical point of view, one can also use Lie algebra techniques and a decomposition of the evolution on each group generator to obtain an effective Hamiltonian [104]. However, the van-Vleck expansion is more tractable as the Hilbert space of the time-independent Hamiltonian gets projected onto the zero-photon subspace: $\mathcal{T} \otimes \mathcal{H} \to \mathcal{T}_0 \otimes \mathcal{H} = \mathcal{H}$. Corrections to the Floquet Hamiltonian can be obtained to all orders in perturbation theory using the van-Vleck expansion.

In this limit, one can describe the dynamics of the driven system over a period T in terms of the effective Floquet Hamiltonian: $H^F_{\mathbf{k}} \approx H^s_{\mathbf{k}} + V^s_{\mathbf{k}}$, where $V^s_{\mathbf{k}}$ represents perturbative driving term. We restrict to contributions of order $1/\omega$ throughout the manuscript, and the form of $V^s_{\mathbf{k}}$ is given by

$$V^s_{\mathbf{k}} = \sum_{p=1}^{\infty} \frac{[V_{-p}, V_p]}{p\omega}, \tag{5.4}$$

with $V_p = \frac{1}{T}\int_0^T H^s_{\mathbf{k}}(\mathbf{A}, t)\, e^{ip\omega t}\, dt$ and $\omega = \frac{2\pi}{T}$. Evaluating $V^s_{\mathbf{k}}$ for our system, we arrive at

$$
\begin{aligned}
V_p &= s\alpha_n \sum_{m=1}^{n} (k_\perp)^{n-m} (-A_0)^m \ {}^nC_m \\
&= \begin{bmatrix} 0 & e^{-i[(n-m)\phi + m\frac{\pi}{2}]}\delta_{p,-m} \\ e^{i[(n-m)\phi + m\frac{\pi}{2}]}\delta_{p,-m} & 0 \end{bmatrix}. \qquad (5.5)
\end{aligned}
$$

Using the result in (5.5) and evaluating the commuatator in (5.4), we find that the effective Floquet Hamiltonian takes the form

$$
\begin{aligned}
H^F_{\mathbf{k}} &= H^s_{\mathbf{k}} + V^s_{\mathbf{k}} \\
&= C_s(k_z - sQ) + s\alpha_n \boldsymbol{\sigma} \cdot (\mathbf{n}_{\mathbf{k}} - sQ\hat{e}_z) \\
&+ \frac{\alpha_n^2}{\omega} \sum_{p=1}^{n} \frac{1}{p} \left({}^nC_p A_0^p \right)^2 k_\perp^{2n-2p} \sigma_z \\
&= C_s(k_z - sQ) + s\alpha_n (\mathbf{n}'_{\mathbf{k}} - sQ\hat{e}_z) \cdot \boldsymbol{\sigma} \qquad (5.6)
\end{aligned}
$$

with $\mathbf{n}'_{\mathbf{k}} = (k_\perp^n \cos(n\phi_k), k_\perp^n \sin(n\phi_k), T_{\mathbf{k}}/\alpha_n)$. We define $T_{\mathbf{k}} \equiv vk_z + \frac{\alpha_n^2}{\omega} \sum_{p=1}^{n} \beta_p^n k_\perp^{2(n-p)} \equiv \Delta_n + T'_{\mathbf{k}}$, with $T'_{\mathbf{k}} \equiv vk_z + \frac{\alpha_n^2}{\omega} \sum_{p=1}^{n-1} \beta_p^n k_\perp^{2(n-p)}$, and $\beta_p^n = ({}^nC_p A_0^p)^2/p$. The momentum independent contribution to the Floquet Hamiltonian acquires the form $\Delta_n = \frac{\alpha_n^2 A_0^{2n}}{n\omega}$. It clear from the construction of (5.6) that the effective Hamiltonian embodies terms which couple higher momentum modes (modes which diverge faster than k as $k \to \infty$) of the Weyl fermion to the photon. The extra terms, absent for $n = 1$, appears due to the anisotropic energy dispersion of the static mWSM Hamiltonian (5.1). A close inspection of effective Hamiltonian (5.6) suggests that circularly polarized light can not open up a gap in WSM as the time reversal symmetry is intrinsically broken in static Hamiltonian (5.1); instead the position of the Weyl points shifts from $(0, 0, sQ) \to (0, 0, sQ - \Delta_n)$. We note here $T'_{\mathbf{k}} = vk_z$ for $\mathbf{k} = (0, 0, k_z)$. Interestingly, unlike the single Weyl case where the shift Q quadratically varies with driving amplitude A_0^2, the shift in the Weyl point for mWSMs Δ_n is coupled with monopole charge

n as $\Delta_n = \frac{\alpha_n^2 A_0^{2n}}{n\omega}$. The terms containing $k_\perp$ in $T'_{\mathbf{k}}$ would lead to subleading corrections in transport properties.

The effective quasi-energies obtained from Floquet Hamiltonian (5.6), are thus

$$E^F_{\mathbf{k}} = C_s(k_z - sQ) \pm s\sqrt{\alpha_n^2 k_\perp^{2n} + T^2_{\mathbf{k}}}, \tag{5.7}$$

leading to the established result: $E^F_{\mathbf{k}}(n=1) = C_s(k_z - sQ) \pm s\sqrt{v^2k_\perp^2 + (vk_z + \Delta_1)^2}$ as $\alpha_1 = v$. One can observe that $k_\perp$ term in $T_{\mathbf{k}}$ is absent for conical dispersion while for $n > 1$, the anisotropy in conical dispersion leads to terms dependent on $k_\perp$ in $T_{\mathbf{k}}$. For completeness, we note that the static energy of an mWSM Hamiltonian with no driving is obtained by diagonalizing the Hamiltonian (5.1) to obtain $E^0_{\mathbf{k}} = C_s(k_z - sQ) \pm \sqrt{\alpha_n^2 k_\perp^{2n} + v^2 k_z^2}$. Therefore, one can clearly see that the external optical field paramters get coupled with momentum $k_\perp$ leading to the complex form of $T_{\mathbf{k}}$ in Eq. (5.7). In particular, the nature of the Floquet dispersion (5.7) changes due to the coupling of the incident light parameter A_0 and ω with the momentum $k_\perp$ and the topological charge n. Another interesting feature of the Floquet dispersion is that k_z gets coupled to $k_\perp$ that is not noticed for irradiated single WSMs. The static and Floquet dispersion are extensively analyzed in SI, Sec. II.

5.2 Berry Curvature

It is crucial to study geometric phases in any topological system as anomalous response functions are usually related to the Berry curvature. Here our aim would be to investigate the effect of the driving on the Berry curvature and subsequently on the anomalous transport. Before going into detail, we begin by defining the Berry curvature associated with the Floquet Hamiltonian $H^F_{\mathbf{k}}$. The Berry curvature of the

m$^{\text{th}}$ band for a Bloch Hamiltonian $H(k)$, defined as the Berry phase per unit area in the k space, is given by [105]

$$\Omega_a^m(\mathbf{k}) = (-1)^m \frac{1}{4|n_{\mathbf{k}}|^3} \epsilon_{abc} \mathbf{n}_{\mathbf{k}} \cdot \left(\frac{\partial \mathbf{n}_{\mathbf{k}}}{\partial k_b} \times \frac{\partial \mathbf{n}_{\mathbf{k}}}{\partial k_c} \right). \tag{5.8}$$

The explicit form of the Berry curvature associated with the Weyl node having chirality $s = \pm 1$ as obtained from Floquet effective Hamiltonian (5.6) is given by

$$\begin{aligned} \Omega_F^{\pm,s}(\mathbf{k}) &= \pm \frac{1}{2} \frac{1}{|E_{\mathbf{k}}^F|^3} (nv\alpha_n^2 k_\perp^{2n-1} \cos\phi_{\mathbf{k}}, nv\alpha_n^2 k_\perp^{2n-1} \sin\phi_{\mathbf{k}}, \\ &- n\beta_{\mathbf{k}} \alpha_n^2 k_\perp^{2n} + T_{\mathbf{k}} n^2 \alpha_n^2 k_\perp^{2n-2}), \end{aligned} \tag{5.9}$$

with $\beta_{\mathbf{k}} = \frac{\alpha_n^2}{\omega} \sum_{p=1}^{n} (2n-2p) \beta_p^n k_\perp^{2n-2p-2}$. We note that $+(-)$ sign refers to the valence (conduction) band. The Berry curvature remains unaltered irrespective of the chirality of the Weyl nodes, i.e., $\Omega^{\pm,+} = \Omega^{\pm,-}$. One obtains the regular static Berry curvature when $A_0 = 0$, $\beta_{\mathbf{k}} = 0$ and $T_{\mathbf{k}} = vk_z$. The static Berry curvature using Hamiltonian (5.1) becomes

$$\begin{aligned} \Omega_0^{\pm,s}(\mathbf{k}) &= \pm \frac{1}{2} \frac{1}{|E_{\mathbf{k}}^0|^3} (nv\alpha_n^2 k_\perp^{2n-1} \cos\phi_{\mathbf{k}}, nv\alpha_n^2 k_\perp^{2n-1} \sin\phi_{\mathbf{k}}, \\ &n^2 v \alpha_n^2 k_\perp^{2n-2} k_z), \end{aligned} \tag{5.10}$$

Therefore, one can observe that $\Omega_z(\mathbf{k})$ is modified due to the driving, while the remaining two components of $\Omega_F^{\pm}(\mathbf{k})$ receive the correction from the effective energy $E_{\mathbf{k}}^F$ appearing in the denominator. This suggests that anomalous conductivity σ_{xy}^a would be modified due to the driving as compared to σ_{xz}^a and σ_{yz}^a. We shall analyze this extensively in the what follows.

Now, turning to $n = 1$ case, the Berry curvature for driven single WSM case is given by $\Omega_F^{\pm,s}(\mathbf{k}, n=1) = (k_x, k_y, k_z + v^3\Delta_1)/|E_{\mathbf{k}}^0(n=1)|^3$. Importantly, even for $\Omega_z(\mathbf{k})$ in single WSMs, the momentum independent term $\Delta_1 \sim A_0^2$ bears the signature

of periodic driving. For $n > 1$, the topological charge gets coupled with the driving parameter which leads to a more complex form of $\Omega_z(\mathbf{k})$ as compared to the $n = 1$ case.

We shall compute the anomalous Hall conductivity $\sigma^a_{F,xy}$, considering the effective Floquet Hamiltonian, from the z-component of Berry curvature in Eq. (5.10). In order to obtain a closed form results in the leading order, we neglect $\beta_{\boldsymbol{k}}$ as $\omega \to \infty$ as the effective energy in the denominator bears the correction terms due to driving as shown in Eq. (5.7). We, on the other hand, consider the effect of the Floquet driving on the cut-off limit of k_z integration. In particular, $z_l = -\Lambda - sQ \to z'_l$ and $z_u = \Lambda - sQ \to z'_u$ with $z'_l = -\Lambda - sQ + s\Delta_n$ and $z'_u = \Lambda - sQ + s\Delta_n$. Therefore, one can safely consider the static energy in the denominator, and we shall motivate this assumption extensively while discussing the vacuum contribution Sec. 5.3.1. The anomalous contribution to leading order is thus given by

$$\begin{aligned}
\sigma^a_{F,xy} &= e^2 \int \frac{d\boldsymbol{k}}{4\pi^2} \sum_s \Omega_F^{-,s}(\boldsymbol{k}) \\
&\simeq -\frac{ne^2}{4\pi^2} \int_{z'_l}^{z'_u} \int_0^\infty dk_\perp dk_z \frac{k_z k_\perp}{(k_z^2 + k_\perp^2)^{3/2}} \\
&\simeq -\frac{ne^2}{2\pi^2}(Q + \Delta_n) \qquad (5.11)
\end{aligned}$$

We have considered cylindrical polar co-ordinates for the convenience of the integration along with the following rescaling: $k_z \to k_z/v$ and $k_\perp \to k_\perp^{1/n} \alpha_n^{-1/n}$. It is noteworthy that this anomalous Hall coefficient is a topological property due to the appearance of the monopole charge. For the static system, it is just given by $-\frac{ne^2}{2\pi^2}Q$. Since the Berry curvature of the filled valence band remains same for both the nodes with opposite chiralities. The results obtained considering these two nodes is just the double of that of the obtained in single node.

We now connect our findings to the transport phenomena in the mWSMs. It has been shown that there exist n number of Fermi arcs for a mWSM with topological charge n [52], and we know the transport is mainly governed by the surface states present in the Fermi arc for WSMs. Interestingly, driving shifts the position of Weyl points $\pm Q \to \pm Q + \Delta_n$; this leads to the modification in Fermi arc for irradiated case as compared to the static case. As a result, transport properties receive additional corrections from driving. It has been shown that Fermi arc can be tuned using Floquet replica technique when a WSM is irradiated with circularly polarized light [92]. The factor n in front of Eq. (5.11) signifies that effective Floquet Hamiltonian still supports n number of Fermi arcs. We here mention that the neglected $\beta_{\boldsymbol{k}}$ term would give rise to sub-leading non-topological contributions. Since we wish to probe the question of transport due to laser driving, it would be appropriate to investigate the optical conductivity using Floquet-Kubo formalism. However, we note at the outset that one can find similar expression as given in Eq. (5.11) while calculating the vacuum contribution of optical conductivity up to leading order.

5.3 Conductivity tensor

Having derived the Berry curvature induced anomalous Hall conductivity, we shall now systematically formulate the conductivity tensor using the current-current correlation function. This is constructed using the Matsubara Green's function method. The current-current correlation is written as

$$\begin{aligned} \pi_{\mu\nu}(\Omega, \mathbf{k}) &= T \sum_{\omega_n} \sum_{s=\pm} \int \frac{d^3k}{(2\pi)^3} J_\mu^{(s)} G_s(i\omega_n, \mathbf{k}) \\ & \quad J_\nu^{(s)} G_s(i\omega_n - i\Omega_m, \mathbf{k} - \mathbf{q})|_{i\Omega_m \to \Omega + i\delta} \end{aligned} \tag{5.12}$$

Here, $\mu, \nu = \{x, y, z\}$, T is the temperature, ω_n and Ω_n are the fermionic and bosonic Matsubara frequencies and G is the single particle Green's function. The Hall conductivity can now be derived from the zero frequency $\Omega \to 0$ and zero wave-vector limit.

Using the current-current correlation (5.12), one can define the static conductivity tensor σ^0_{ab}. We here use the form of the time-averaged conductivity tensor σ^F_{ab} in the form of the Kubo formula, modified for the Floquet states as

$$\begin{aligned} \sigma^F_{ab} = \quad & i \quad \int \frac{d^3\mathbf{k}}{(2\pi)^3} \sum_{\alpha \neq \beta} \frac{f_\beta(\mathbf{k}) - f_\alpha(\mathbf{k})}{\epsilon_\beta(\mathbf{k}) - \epsilon_\alpha(\mathbf{k})} \\ & \times \quad \frac{\langle \Phi_\alpha(\mathbf{k}) | J_b | \Phi_\beta(\mathbf{k}) \rangle \langle \Phi_\beta(\mathbf{k}) | J_a | \Phi_\alpha(\mathbf{k}) \rangle}{\epsilon_\beta(\mathbf{k}) - \epsilon_\alpha(\mathbf{k}) + i\eta} \end{aligned} \tag{5.13}$$

which resembles the standard form of the Kubo formula where $J_{a(b)}$ represents the current operator, the $|\Phi_\alpha(\mathbf{k})\rangle$ represents the states of the effective Floquet Hamiltonian (5.6), and ϵ_α represent the corresponding quasi-energies. The f_α represent the occupations which in general could be non-universal in systems which are out of equilibrium. In such cases, the steady-state occupations can take the form of Fermi-Dirac distribution associated with the quasi-energies of the Floquet states, depending on the characteristics of the drive. The Matusubara formalism turns out to hold for Floquet states as well [106] and we use this method in the current work. The Floquet-Kubo formalism has been widely used in calculating optical Hall conductivity in open and closed quantum systems. [107–110].

One can start from Luttinger's phenomenological transport equations [111] for the electric and energy DC currents. The energy current is originated from the combination of heat current J_Q and energy transported by the electric current J_E in presence of electromagnetic field while the underlying system is characterized by a

finite chemical potential μ and temperature T. Within the Fermi liquid limit $k_B T \ll |\mu|$, the Mott rule and the Wiedemann-Franz law relate the thermopower α and thermal conductivity K, respectively, to the electric conductivity σ [37, 112, 113]:

$$\alpha_{ab} = eLT\frac{d\sigma_{ab}}{d\mu}, \qquad K_{ab} = LT\sigma_{ab}. \tag{5.14}$$

Here, α_{ab} is the Nernst conductivity and K_{ab} is the thermal Hall conductivity and $L = \pi^2 k_B^2/3e^2$ is the Lorentz number. These formulas are assumed to be valid for the effective time-independent Floquet Hamiltonian setup [106], and we shall investigate them in what follows.

One can define the current operator from the effective Floquet Hamiltonian $H^F_{\mathbf{k}}$ Eq. (5.6)

$$J_\mu = e\frac{\partial H^F_{\mathbf{k}}}{\partial k_\mu} \tag{5.15}$$

In order to derive J_μ, we consider the leading order term neglecting $\partial T_{\mathbf{k}}/\partial k_\mu$ term as it contains $1/\omega$ factor. We note that the current operator obtained in this manner would be the same as the static current operator for mWSM Hamiltonian. This leading order term can be further confirmed by the zeroth order Fourier component of the current operator as shown in Appendix C part 3. The effect of $T_{\mathbf{k}}$ term is also encoded in the single particle Greens function G_s. We compute the optical conductivity by using the complete expression of G_s and approximated current operator.

In terms of the Pauli matrices, we can write upto leading order as

$$J_x \approx esn\alpha_n k_\perp^{n-1}[\cos((n-1)\phi_{\mathbf{k}})\sigma_x + \sin((n-1)\phi_{\mathbf{k}})\sigma_y] \tag{5.16}$$

$$J_y \approx esn\alpha_n k_\perp^{n-1}[\cos((n-1)\phi_{\mathbf{k}})\sigma_y - \sin((n-1)\phi_{\mathbf{k}})\sigma_x] \tag{5.17}$$

The point to note here is that J_x and J_y both depend on k_x and k_y which is in contrast to the single WSM case where $J_i \sim k_i \sigma_i$. The anisotropic nature of dispersion of the mWSM Hamiltonian thus engraves its effect on the current operator.

Employing the current-current correlation and performing a detailed calculation (see Appendix C part 4), we arrive at the conductivity tensor as

$$\begin{aligned}\sigma_{xy} &= \frac{e^2 n^2 \alpha_n^2}{4\pi^2} \sum_{s=\pm} \int_0^\infty dk_\perp k_\perp^{2n-1} \int_{-\Lambda}^{\Lambda} dk_z \\ &\quad \frac{sv(k_z - Q) + \frac{s\alpha_n^2}{\omega} \sum_{p=1}^n \beta_p^n k_\perp^{2(n-p)}}{[(\frac{s\alpha_n^2}{\omega} \sum_{p=1}^n \beta_p^n k_\perp^{2(n-p)} + sv(k_z - sQ))^2 + \alpha_n^2 k_\perp^{2n}]^{3/2}} \\ &\times \quad [n_F(E_{\mathbf{k}}^{F,-}) - n_F(E_{\mathbf{k}}^{F,+})] \end{aligned} \tag{5.18}$$

where Λ is the ultra-violet cut-off of k_z integral, $n_F(E) = \frac{1}{e^{\beta(E-\mu)}+1}$ is the Fermi-Dirac distribution function, and $\beta = 1/T$ is inverse temperature. The total optical conductivity (5.18) is the sum of vacuum and Fermi surface contributions which we shall calculate below. We note that due to the existence of external and internal energy scale ω and μ, the cut-off Λ plays an important role in achieving physically meaningful results. This cut-off is ultra-violet in nature and can in principle depend on the detail of the material.

5.3.1 Vacuum contribution

In this section, we investigate the vacuum contribution which is obtained in the limit $[n_F(E_{\mathbf{k}}^{F,-}) - n_F(E_{\mathbf{k}}^{F,+})] \to 1$. Physically this means that valence (conduction) band is completely filled (empty). This vacuum contribution is topological and amounts to an intrinsic contribution that remains finite for $\mu \to 0$. With suitable re-definitions and linear integration variable shifts, we arrive at

$$\begin{aligned}\sigma_{xy}^{vac} &= \frac{e^2 n^2 \alpha_n^2}{4\pi^2}\sum_{s=\pm}\int_0^{\infty} dk_\perp k_\perp^{2n-1}\int_{-\Lambda-sQ+\frac{s\alpha_n^2}{\omega}A_0^{2n}}^{\Lambda-sQ+\frac{s\alpha_n^2}{\omega}A_0^{2n}} \\ &\times \frac{[svk_z+\frac{\alpha_n^2}{\omega}\sum_{p=1}^{n-1}\beta_p^n k_\perp^{2(n-q)}]}{[(\frac{\alpha_n^2}{\omega}\sum_{q=1}^{n-1}\beta_q^n k_\perp^{2(n-q)})^2+\alpha_n^2 k_\perp^{2n}]^{3/2}}.\end{aligned} \tag{5.19}$$

We will compute the vacuum contribution using two separate procedures involving suitable approximations and then compare the obtained results.

5.3.1.1 Coordinate Transformation Method

The method prescribed in this section relies on the fact that while several quantities are set to infinity in a computation, in order to get physically plausible answers one might need to define the order in which the limits are taken. For computation of the integrals, the following coordinate map $\mathcal{M}:\mathbb{R}^2\to\mathbb{R}^2$ is prescribed with the action $k_\perp \to k'_\perp = k_\perp^{\frac{1}{n}}\alpha_n^{-\frac{1}{n}}$, and $k_z \to k_z$. With this coordinate transformation, the vacuum contribution of the conductivity tensor looks like

$$\sigma_{xy}^{vac} = -\frac{e^2 n \alpha_n^{2-\frac{2}{n}}}{4\pi^2}\sum_{s=\pm} s\int_{z_l}^{z_u}\int_{x_l}^{x_u}\frac{k_\perp T_{\mathbf{k}}}{(k_\perp^2+T_{\mathbf{k}}^2)^{3/2}}dk_\perp dk_z \tag{5.20}$$

Here, the upper and lower limits of the integrals have been determined with appropriate physical justifications (see Appendix C part 4):

$$\begin{aligned} x_l &= 0, \quad x_u = \Lambda_\perp \\ z_u &= v(\Lambda - sQ) + s\left(\Delta_n + \frac{\alpha_n^2}{\omega}\sum_{p=1}^{n-1}\beta_p^n \alpha_n^{\frac{2(p-n)}{n}}\Lambda_\perp^{\frac{2(n-p)}{n}}\right) \\ z_l &= v(-\Lambda - sQ) + s\left(\Delta_n + \frac{\alpha_n^2}{\omega}\sum_{p=1}^{n-1}\beta_p^n \alpha_n^{\frac{2(p-n)}{n}}\Lambda_\perp^{\frac{2(n-p)}{n}}\right)\end{aligned} \tag{5.21}$$

$\Lambda_\perp$ is the cut-off for $k_\perp$ integral. One can segregate $z_{l,u}$ from $\Lambda_\perp$: $z_{l,u} = z'_{l,u} + s\frac{\alpha_n^2}{\omega} X_{\Lambda_\perp}$ with $X_{\Lambda_\perp} = \sum_{p=1}^{n-1} \beta_p^n \alpha_n^{\frac{2(p-n)}{n}} \Lambda_\perp^{\frac{2(n-p)}{n}}$ and $z'_{l,u} = v(\mp\Lambda - sQ) + s\Delta_n$. Hence one has to handle this cut-off with care, and the issue reduces to the order of taking limits. We again stress that the high frequency Floquet effective Hamiltonian is valid when ω is larger than the bandwidth not permitting any real electronic transitions. Keeping this in mind, the sub-leading $1/\omega$ order correction that we want to extract is preserved as we execute the $k_\perp$ integral followed by the k_z integral. We note that while solving the $k_\perp$ integral, without loss of generality $\Lambda_\perp$ is considered to be large as compared to Λ. Importantly, $\Lambda_\perp/\omega$ is small compared to Λ and hence $X_{\Lambda_\perp}$ is a sub-leading term since ω sets the dominant energy scale in the problem. Taken collectively, the subleading $X_{\Lambda_\perp}$ term is held finite during the $k_\perp$ integration and this leads to the $\Lambda_\perp$ dependence reappearing through the limits of the k_z integral. In a nutshell, our resullt is applicable when $\omega \gg \Lambda_\perp \gg \Lambda$. We justify the above assumptions for the high frequency Floquet effective Hamiltonian $H^F_{\boldsymbol{k}}$ (5.6) that is derived from a low energy minimal model (5.1).

Finally, we obtain the vacuum contribution of conductivity in mWSM,

$$\sigma_{xy}^{vac} = n\frac{e^2 Q \alpha_n^{2-\frac{2}{n}}}{2\pi^2} - n\frac{e^2 \alpha_n^{2-\frac{2}{n}}}{2\pi^2}\left[\Delta_n - \frac{\alpha_n^2}{\omega v}\sum_{p=1}^{n-1}\beta_p^n \Lambda_\perp^{2(n-p)}\right] \tag{5.22}$$

Here, Δ_n and β_p^n are the contributions appearing as an effect of irradiated light. One can easily recover the $n = 1$ behavior of gap where Δ_1 varies quadratically with the amplitude of driving A_0 [106]. For $n > 1$ further corrections, due to higher order curvature of the Floquet Hamiltonian, contribute via the cut-off of the low-energy model.

5.3.1.2 Series Expansion Method

We shall now proceed with a physically justified alternative method to compute $\Lambda_\perp$ in terms of the k_z cut-off. The idea here is to expand the denominator around its unperturbed static energy in increasing powers of driving period $1/\omega \to 0$ as $\omega \to \infty$. The perturbative expansion is then given by

$$k_\perp^2 + T_{\mathbf{k}}^2 \approx E_{\mathbf{k}}^2 + \frac{2vk_z\alpha_n^2}{\omega}\sum_{p=1}^{n-1}\beta_n^p \alpha_n^{\frac{2(p-n)}{n}} k_\perp^{\frac{2(n-p)}{n}} \tag{5.23}$$

One can then note that for $n = 2$, only β_1^n exists while for $n = 3$, β_1^n and β_2^n both exist. $E_{\mathbf{k}} = \sqrt{k_\perp^{2n} + v^2k_z^2}$ is the bare static energy of mWSM in the absence of tilt. Considering $X_{k_\perp} = \sum_{p=1}^{n-1}\beta_p^n \alpha_n^{\frac{2(p-n)}{n}} k_\perp^{\frac{2(n-p)}{n}}$, we now express the integrand as

$$\begin{aligned}\frac{T_{\mathbf{k}}}{(k_\perp^2 + T_{\mathbf{k}}^2)^{3/2}} &\approx \frac{1}{E_{\mathbf{k}}^3}\Bigg[vk_z - \frac{3v^2k_z^2\alpha_n^2}{E_{\mathbf{k}}^2\omega}X_{k_\perp} \\ &+ \frac{\alpha_n^2}{\omega}X_{k_\perp}\left(1 - \frac{3vk_z\alpha_n^2}{E_{\mathbf{k}}^2\omega}X_{k_\perp}\right)\Bigg]\end{aligned} \tag{5.24}$$

We explicitly write σ_{xy}^{vac} for $n = 2$ (neglecting $1/\omega^2$ term) as,

$$\begin{aligned}\sigma_{xy}^{vac}(n=2) &= -\frac{e^2n\alpha_n^{2-\frac{2}{n}}}{4\pi^2}\sum_{s=\pm}s\int_{z_l'}^{z_u'}\int_0^\infty \frac{k_\perp T_{\mathbf{k}}}{(k_\perp^2 + T_{\mathbf{k}}^2)^{3/2}}dk_\perp dk_z \\ &\approx -\frac{e^2n\alpha_n^{2-\frac{2}{n}}}{4\pi^2}\sum_{s=\pm}s\left(v(z_l + z_u) + v^2\alpha_n\beta_1^n(z_l' - z_u')\right) \\ &\approx -\frac{e^2n\alpha_n^{2-\frac{2}{n}}}{4\pi^2}\left(v(-2Q + 2\Delta_n) + \frac{2v^2\alpha_n\beta_1^n}{\omega}\Lambda\right)\end{aligned} \tag{5.25}$$

In this derivation, we ignore the divergent contributions coming from the integrals having higher powers of $k_\perp$ in the numerator. These types of terms, being artifacts of the underlying low-energy model, do not appear in the lattice model. In order to obtain $\Lambda_\perp$, we equate the coefficient of $1/\omega$ from Eq. (5.25) and Eq. (5.22). We find

$\Lambda_\perp$ linearly depends on Λ': $\Lambda_\perp = 2v^2\Lambda'$. For $n = 3$, we find

$$\begin{aligned}\sigma_{xy}^{vac}(n=3) = & -\frac{e^2 n\alpha_n^{2-\frac{2}{n}}}{4\pi^2}\Bigg[v(-2Q+2\Delta_n) \\ & - \frac{2v^2\alpha_n^{\frac{2}{n}}\beta_1^n}{\omega\sqrt{\pi}}\Gamma\Big(\frac{5}{6}\Big)\Gamma\Big(\frac{5}{3}\Big)\Big(\frac{|z_l|^{\frac{4}{n}}+z_u^{\frac{4}{n}}}{4/3}\Big) \\ & + \frac{\beta_2^n}{\omega}\Bigg[-\frac{3v^2\alpha_n^{\frac{4}{n}}}{2\sqrt{\pi}}\Gamma\Big(\frac{7}{6}\Big)\Gamma\Big(\frac{7}{3}\Big)\Big(\frac{|z_l|^{\frac{2}{n}}+z_u^{\frac{2}{n}}}{2/3}\Big) \\ & + \frac{\alpha_n^{\frac{4}{n}}}{\sqrt{\pi}}\Gamma\Big(\frac{1}{6}\Big)\Gamma\Big(\frac{4}{3}\Big)\Big(\frac{|z_l|^{\frac{2}{n}}+z_u^{\frac{2}{n}}}{2/3}\Big)\Bigg]\Bigg] \end{aligned} \tag{5.26}$$

It is noted that contrary to the $n = 2$ case, $\Lambda_\perp$ is non-linearly related to Λ' for $n = 3$: $\Lambda_\perp^{\frac{4}{n}} = \eta_1[|z_l|^{\frac{4}{n}} + z_u^{\frac{4}{n}}]$ and $\Lambda_\perp^{\frac{2}{n}} = \eta_2[|z_l|^{\frac{2}{n}} + z_u^{\frac{2}{n}}]$ where $\eta_{1,2}$ can be obtained by matching the coefficient of β_1^n/ω and β_2^n/ω. The relationship between Λ and $\Lambda_\perp$ derived here are consistency conditions for the model parameters.

5.3.2 Fermi-surface contribution

We take a note of the point that for the calculation of the Fermi surface contribution, one has to consider the finite upper limit in the $k_\perp$ integral as b, a parameter which we compute below. The Fermi surface contribution for a given n becomes

$$\begin{aligned}\sigma_{xy}^{FS}(n) &= n\alpha_n^{2-2/n}\sum_s s\int_{z_l'}^{z_u'} dk_z \int_0^b \frac{k_\perp T_{\mathbf{k}}}{(k_\perp^2+T_{\mathbf{k}}^2)^{3/2}}dk_\perp \\ &\times \{\Theta(v^2k_z^2+(Ck_z+sC\Delta_n-\mu)^2)-1\}\end{aligned} \tag{5.27}$$

In the equation above, $\Theta(x)$ represents the Heaviside function which arises from the zero-temperature Fermi-Dirac distribution. It is then more convenient to write $T_{\mathbf{k}}$ explicitly for $n = 2$ as $T_{\mathbf{k}} = vk_z+\beta_1^n\alpha_n^{-2/n}k_\perp^{2/n}$ and for $n = 3$ as $T_{\mathbf{k}} = vk_z+\beta_1^n\alpha_n^{-4/n}k_\perp^{4/n}+\beta_2^n\alpha_n^{-2/n}k_\perp^{2/n}$. In a more compact notation, for $n = 3$, we define $\beta_2' = \beta_2^n\alpha^{-2/n}$, $\beta_3' = \beta_1^n\alpha_n^{-4/n}$ and for $n = 2$, we define $\beta_2' = \beta_1^n\alpha^{-2/n}$ and $\beta_3' = 0$. On the other hand,

$b = \{Ck_z + sC\beta_1 - \mu)^2 - v^2k_z^2\}^{1/2}$. Below we shall exprees all our findings in terms of β_2' and β_3' for a general n.

In the leading order approximation, $\beta_1 = \mathcal{O}(\frac{1}{\omega})$, $k_z \to 0$ and μ is held finite. We shall consider the cases for type-I and type-II cases separately: $|C| \gg v, b = \mu - Ck_z$ and $|C| \ll v, b = (\mu^2 - v^2k_z^2)^{1/2}$. We resort to leading order method once again, where we permit only the $\mathcal{O}(1/\omega)$ order term and obtain the following:

$$\sigma_{xy}(n) = \frac{n\alpha_n^{2-2/n}}{v} \int_{z_l'}^{z_l'} dk_z \int_0^b dk_\perp k_\perp (F_{\mathbf{k},1} + F_{\mathbf{k},2} + F_{\mathbf{k},3}) \tag{5.28}$$

with $F_{\mathbf{k},1} = \frac{k_z}{E_{\mathbf{k}}^3}, F_{\mathbf{k},2} = \frac{\beta_2' k_\perp^{\frac{2}{n}} + \beta_3' k^{\frac{4}{n}}}{E_{\mathbf{k}}^3}, F_{\mathbf{k},3} = -\frac{3k_z^2 F_{\mathbf{k},2}}{E_{\mathbf{k}}^5}$. We note that in Eq. (5.28) the leading order term $F_{\mathbf{k},1}$ is also present for the $n = 1$ Weyl node case. Similar to the vacuum contribution of optical conductivity, the multi Weyl nature appears here through a multiplicative factor $n\alpha_n^{2-2/n}$. The additional anisotropic and band bending corrections appear in terms of $1/\omega$ in $F_{\mathbf{k},2}$ and $F_{\mathbf{k},3}$. To obtain a minimal expression, the above derivation is simplified by neglecting the term $F_{\mathbf{k},3}$ as $k_z^2/E_{\mathbf{k}}^3 \to 0$ for $k_z \to 0$ considered for low-energy model. A close inspection suggests that $F_{k,3}$ contains $\mathcal{O}(k_\perp^p/\omega^{p'})$ and $\mathcal{O}(k_z^q/\omega^{q'})$ with $p, q(p', q') < 1(> 1)$. As a result, for $\omega \to \infty$, $F_{k,3}$ can be neglected compared to the leading order terms $F_{k,1}$.

For type-I mWSM, one can keep in mind the fact that b remains always positive.

The total contribution from the Fermi surface is given by

$$\begin{aligned}\sigma_{xy}^{FS(I)} \approx & -\frac{e^2 n\alpha_n^{2-2/n}}{4\pi^2}\Bigg[(\mu - C\Delta_n)\Big[\frac{v}{C^2}\ln\Big(\frac{v+C}{v-C}\Big) - 2\Big] \\ + & \ \beta_2' a(M)\Big(\mu^{\frac{2M}{n}-3}\frac{2v(\mu - C\Delta_n)}{v^2 - C^2} \\ - & \ \Big(\frac{2M}{n} - 3\Big)v^2\mu^{\frac{2M}{n}-5}\Big(\frac{\mu - C\Delta_n}{v^2 - C^2}\Big)^3(3C^2 + v^2)\Big) \\ + & \ \beta_3'\{M \to 2M\}\Bigg]\end{aligned} \tag{5.29}$$

with

$$a(M) = \frac{\Gamma(\frac{M}{n} + 2)}{(\frac{2M}{n} + 2)(\frac{2M}{n} - 3)\Gamma(\frac{M}{n} + 1)} \tag{5.30}$$

with $M = 1$. Therefore, the leading contribution is not just given by $n\alpha_n^{2-2/n}$ multiplied to $n = 1$ contribution. In this first term μ gets shifted to $\mu - C\Delta_n$ while Δ_n depends on topological charge n. The other sub-leading order terms are of order $1/\omega$. We can write a closed form expression for $v \gg |C|$ as follows,

$$\begin{aligned}\sigma_{xy}^{FS(I)} = & \ n\frac{\alpha_n^{2-2/n}}{v}\cdot\frac{e^2}{4\pi^2}\Bigg[\frac{C(\mu - C\Delta_n)}{6v^2} \\ + & \ 4\beta_2' a(M)\Big(\frac{(2\mu)^{2/n-2}}{v} + \frac{(2/n-3)\mu^{2/n-2}}{v}\Big) \\ + & \ 4\beta_3' a(2M)\Big(\frac{2\mu^{4/n-2}}{v} + \frac{(4/n-3)\mu^{4/n-2}}{v}\Big)\Bigg]\end{aligned} \tag{5.31}$$

Therefore, total conductivity of type-I mWSM for a given n is expressed as

$$\begin{aligned}\sigma_{xy}^{I}(n) = & \ n\frac{e^2}{4\pi^2}\frac{\alpha_n^{2-2/n}}{v}\Bigg[(Q + \Delta_n) + C\Big(\frac{\mu - C\Delta_n}{6v^2}\Big) \\ + & \ 4\beta_2'' a(M)\mu^{2/n-2} + 4\beta_3'' a(2M)\mu^{4/n-2}\Bigg]\end{aligned} \tag{5.32}$$

with $\beta_2'' = \beta_2'(\frac{2}{v} + \frac{2/n-3}{v})$ and $\beta_3'' = \beta_3'(\frac{2}{v} + \frac{4/n-3}{v})$. This helps us to write the anomalous thermal Hall conductivity K_{xy}^I and Nernst conductivity α_{xy}^I respectively for the type-I

mWSMs as ,

$$\begin{aligned} K^I_{xy}(n) &= \frac{\pi^2}{3e^2}k_B^2 T\sigma^I_{xy} \\ &= n\frac{Tk_B^2}{12}\frac{\alpha_n^{2-2/n}}{v}\Bigg[(Q+\Delta_n) - C\Big(\frac{\mu - C\Delta_n}{6v^2}\Big) \\ &+ 4\beta_2'' a(M)\cdot\mu^{2/n-2} + 4\beta_3'' a(2M)\cdot\mu^{4/n-2}\Bigg] \end{aligned} \tag{5.33}$$

One can find

$$\begin{aligned} \alpha^I_{xy}(n) &= \frac{\pi^2}{3e^2}k_B^2 T\frac{d\sigma^I_{xy}}{d\mu} \\ &= n\frac{ek_B^2}{12}\cdot\frac{\alpha_n^{2-2/n}}{v}\Bigg[-\frac{C}{6v^2} + 4\beta_2'' a(M)\Big(\frac{2}{n}-2\Big) \\ &\quad \mu^{2/n-3} + 4\beta_3'' a(2M)\Big(\frac{4}{n}-2\Big)\mu^{4/n-3}\Bigg] \end{aligned} \tag{5.34}$$

One can now easily derive the expressions for σ^I_{xy}, K^I_{xy} and α^I_{xy} for $n = 2$ by considering $\beta_3' = 0$. Comments on the new results for $n = 2$ and $n = 3$ and their characteristic dissimilarities from the $n = 1$ case are now in order. In general, nonlinear μ dependence comes from order $1/\omega$ term in $n > 1$ multi Weyl case while the linear μ dependence term only appear for $n = 1$.

Let us now explore the thermal responses for the type-II case of mWSM where sign of $k_\perp$ momentum cut-off b depends on k_z. Handling of the $k_\perp$ integral requires extra care as sgn(b) becomes $+$ $(-)$, depending on k_z being $-(+)$. $|C| \gg v$, refers to

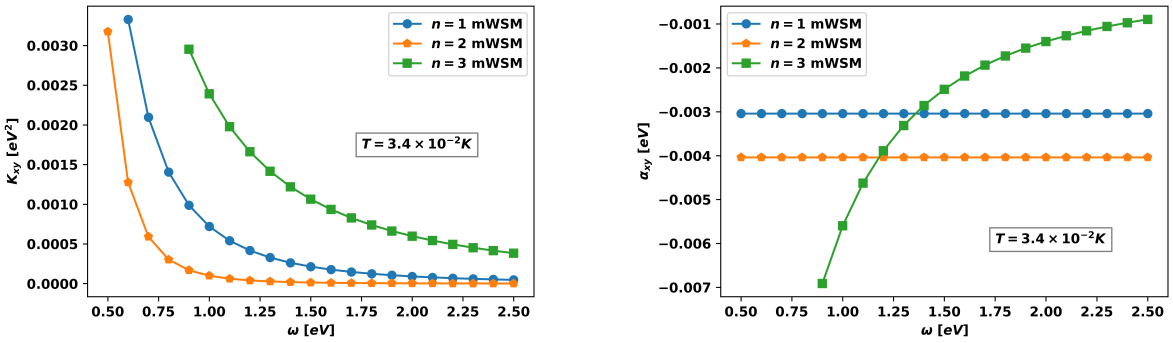

(a) (b)

Figure 5.1: Type-I WSM: (a) Variation of thermal anomalous Hall conductivity with optical frequency, for three different values of the monopole charge. (b) Variation of anomalous Nernst conductivity with optical frequency, for three different values of the monopole charge. The values of the various parameters are specified in Natural units as follows: $v_F = 0.005$, $\alpha_1 = v_F$, $\alpha_2 = 0.00012$ eV^{-1}, $\alpha_3 = 0.00012$ eV^{-2}, $E_0 = \omega A_0 = 1000.0$ eV^2, $C = 0.1$, $\mu = 1.0$ eV, $Q = 2.0$ eV, and $T = 3.4 \times 10^{-2}$K.

the fact $v^2k_z^2 - (Ck_z + sC\Delta_n - \mu)^2 < 0$. Recalling the $k_\perp$ integral, we find

$$\begin{aligned}\sigma_{xy}^{II}(n) = n\frac{e^2}{4\pi^2}\frac{\alpha_n^{2-2/n}}{v}\Bigg[&(\Delta_n+Q)\Big(-1+\frac{v}{C}\Big)\\ -\ &\frac{v(C\Delta_n-\mu)}{C^2}\ln\Big[\frac{C^2\Lambda}{v(C\Delta_n-\mu)}\Big]+\beta_2' a(M)\\ &\Big(\mu^{\frac{2M}{n}-3}\Big(\frac{2\Delta_n v}{C}-2Q\Big)+\Big(\frac{2M}{n}-3\Big)\frac{C\mu^{\frac{2M}{n}-4}}{2}\\ &\Big(\frac{4\Delta_n^2 v}{C}-2\Lambda^2-2Q^2\Big)\Big)+\beta_3'\{M\to 2M\}\Bigg]\end{aligned} \tag{5.35}$$

with $M = 1$. The remarkable point to note here is that the momentum cut-off Λ shows up algebraically in the Fermi surface contribution. However, this is accompanied with the sub-leading term $\mathcal{O}(1/\omega)$. This is indeed a new feature for the anisotropic character of the dispersion in type-II mWSMs. In type-II single WSMs, the momentum cut-off can only appear logarithmically.

Using the results obtained above, we write the anomalous thermal Hall conduc-

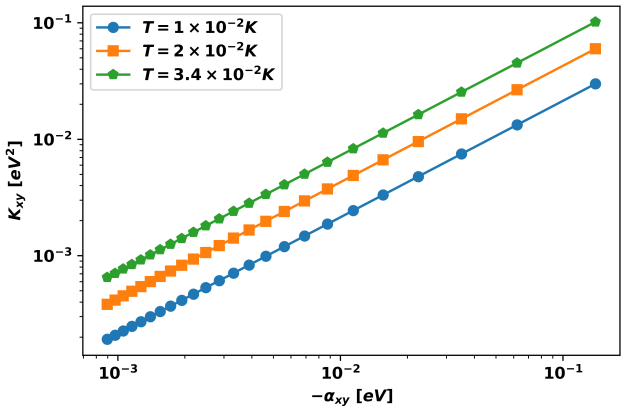

Figure 5.2: Type-I WSM: Variation of thermal anomalous Hall conductivity with Anomalous Nernst conductivity, for $n = 3$ mWSM. The frequency range sampled is 0.50eV - 2.50eV The temperature values sampled are $T = 1\times10^{-2}, 2\times10^{-2}, 3.4\times10^{-2}$ K. The values of the other various parameters are the same as Fig. 5.1.

tivity for type-II mWSMs:

$$\begin{aligned} K_{xy}^{II}(n) = nT\frac{k_B^2}{12}\alpha_n^{2-2/n}\Bigg[&(\Delta_n+Q)\left(\frac{v}{C}-1\right) \\ -\ &\frac{v}{C^2}(C\Delta_n-\mu)\ln\left[\frac{C^2\Lambda}{v(C\Delta_n-\mu)}\right]+\beta_2' a(M) \\ &\left(\mu^{2M/n-3}a_2(M)+\mu^{2M/n-4}a_3(M)\right) \\ +\ &\beta_3'\{M\to 2M\}\Bigg] \end{aligned} \tag{5.36}$$

with $a_2(M) = (2\Delta_n v/C - 2Q)$, $a_3(M) = C(2M/n-3)(4\Delta_n^2 v/C - 2\Lambda^2 - 2Q^2)$ and $M = 1$. On the other hand, the Nernst conductivity is given by

$$\begin{aligned} \alpha_{xy}^{II}(n) = ne\frac{k_B^2\alpha_n^{2-2/n}}{12}\Bigg[&\frac{1}{C^2}\left[-1+\ln\left[\frac{C^2\Lambda}{v(C\Delta_n-\mu)}\right]\right] \\ +\ &\beta_2' a(M)\Bigg(\left(\frac{2M}{n}-3\right)\mu^{2M/n-4}a_2(M) \\ +\ &\left(\frac{2M}{n}-4\right)\mu^{2M/n-5}a_3(M)\Bigg)+\beta_3'\{M\to 2M\}\Bigg] \end{aligned} \tag{5.37}$$

One can easily obtain the $n = 2$ results by considering $\beta_3' = 0$.

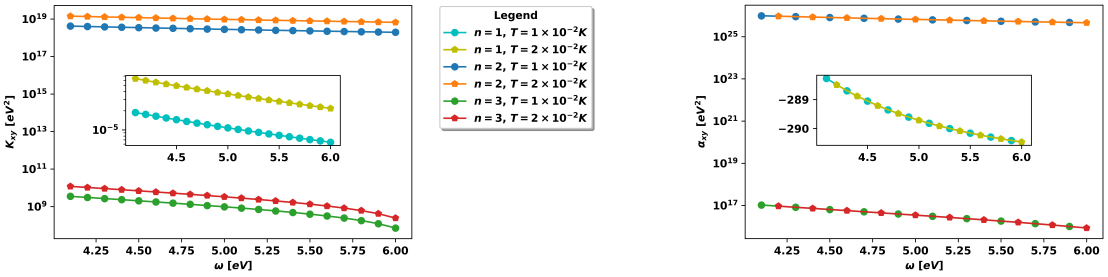

(a) (b)

Figure 5.3: Type-II WSM: (a) Variation of thermal anomalous Hall conductivity with optical frequency, for three different values of the monopole charge. (b) Variation of anomalous Nernst conductivity with optical frequency, for three different values of the monopole charge. The plot (b) shows a strong overlap between the curves for fixed n as a function of temperature. To highlight this issue, the data points sampled for overlapping curves are at distinct values of frequency. The values of the various parameters are specified in Natural units as follows: $v_F = 0.005$, $\alpha_1 = v_F$, $\alpha_2 = 0.00012$ eV^{-1}, $\alpha_3 = 0.00012$ eV^{-2}, $E_0 = \omega A_0 = 1000.0$ eV^2, $C = 0.1$, $\mu = 1.0$ eV, $Q = 2.0$ eV, $\Lambda = 900.0$ eV, and $T = 1 \times 10^{-2}, 2 \times 10^{-2}$ K.

5.4 Discussion of Results

We now discuss some important aspects of our findings on the distinguishable transport features of type-I and type-II mWSMs. First of all, we emphasize on the significant results that show the characteristically different features of the effective chemical potential μ and the cut off Λ for two different types of mWSMs. We also narrate the key roles played by the topological charge n and the tilt C in the thermo-electric transport properties of mWSMs. We note that dispersion becomes anisotropic due to the multi Weyl nature; tilt can additionally make it anisotropic in the tilt direction. Floquet driving can lead to complicated deformations of the static Fermi surface. Moreover, it influences the distribution of chiral Weyl fermions in the electron and hole pockets. Therefore, Floquet transport can noticeably be altered upon the introduction of the tilt. In terms of the physical parameters, the differences in

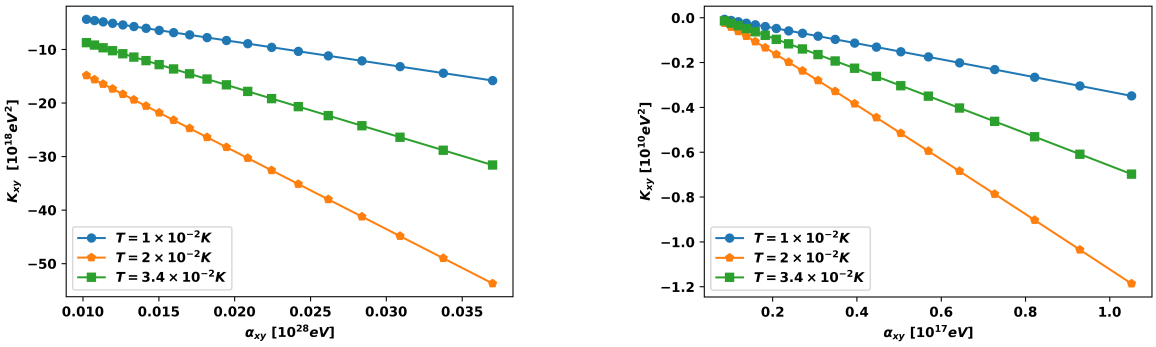

(a) (b)

Figure 5.4: Type-II WSM: (a) Variation of thermal anomalous Hall conductivity with Anomalous Nernst conductivity, for $n = 2$ mWSM. (b) Variation of thermal anomalous Hall conductivity with Anomalous Nernst conductivity, for $n = 3$ mWSM. For both cases, the frequency range sampled is 4.1eV - 6eV. The temperature values sampled are $T = 1 \times 10^{-2}, 2 \times 10^{-2}, 3.4 \times 10^{-2}$ K. The values of the other various parameters are the same as Fig. 5.3.

transport are clearly visible, originating from the nature of the Fermi surface. Having qualitatively analyzed the differences, we below present their quantitative nature.

It is to be noted that Λ^2 is associated with $\mu^{2M/n-4}$ and $\mu^{2M/n-5}$, (with $M = 1, 2$) for optical Hall conductivity, and Nernst conductivity in case of type-II mWSMs, respectively. Therefore, the transport properties in this phase are heavily influenced by the coupling of μ and Λ. This is contrary to the type-I mWSM where only μ can affect the transport in addition to the driving field; Λ does not appear in the transport coefficients. For type-II single WSM, a purely logarithmic cut-off dependence is only observed. Hence, the anisotropy in the tilted dispersion non-trivially couples with the field parameters to generate the unusual cutoff dependence. The shape of the Fermi pockets for type-II mWSMs is very different from type-I mWSM as it evident from the cut-off dependence of transport coefficients. Notably, in case of irradiated tilted mWSMs, the topological charge establishes its effect not only in a simple multiplicative fashion but also in a much more fundamental way, by coupling to the tilt dependent effective chemical potential, where Λ appears algebraically. This algebraic cut-off dependent term is associated with the additional corrections of $\mathcal{O}(1/\omega)$. The

leading order term in the off-diagonal conductivity is given by n times the single Weyl result; here, the anisotropic nature of the dispersion is partially encoded in the shifted chemical potential $\mu \to \mu - C\Delta_n$, where $\Delta_n = \mathcal{O}(A_0^{2n}/\omega)$. The effective chemical potential is also dependent on the frequency of the driving potential and the monopole charge.

Having discussed the implication of cut-off, we now consider the non-linear μ dependence that arises in the conductivity tensor, besides the effective μ. In type-I mWSMs, considering $v \gg |C|$, the vacuum contribution σ_{xy}^{I} associated with $\beta'_{2,3}$ term becomes decreasing function of μ for both for $n = 2$ and $n = 3$; β'_2 term decays inversely (as μ^{-1}) for $n = 2$ and $\beta'_{2,(3)}$ decays non-linearly $\mu^{-4/3}(\mu^{-2/3})$ for $n = 3$. The Nernst conductivity on the other hand, goes as μ^{-2} for $n = 2$, and for $n = 3$ it becomes decreasing function of μ (as $\mu^{-7/3}$ and $\mu^{-5/3}$). In type-II mWSMs, considering $|C| \gg v$, the vacuum contribution σ_{xy}^{II} associated with $\beta'_{2,3}\Lambda^2$ term becomes decreasing function of μ for both the $n = 2$ and $n = 3$ cases. We note that the sub-leading correction decays more rapidly with μ for type-II as compared to type-I mWSMs. In particular, the cut-off independent contributions asscociated with β'_2 term vary as μ^{-2} and μ^{-3} for $n = 2$. While for $n = 3$, these contributions associated with $\beta'_{2,(3)}$ term go as $\mu^{-7/3}$ and $\mu^{-10/3}$ ($\mu^{-5/3}$ and $\mu^{-8/3}$). The Nernst conductivity in this regime becomes strongly decreasing function of μ for both $n = 2$ and $n = 3$ with the lowest power as μ^{-3} and $\mu^{-8/3}$, respectively.

After investigating the transport behavior analytically, we illustrate them as a function of driving frequency to analyze some salient qualitative features. We note that our aim is to pictorially differentiate the type-I from type-II mWSM based on our low-energy model. Hence, at the outset, we confess that certain lattice effects might not be captured following our analysis. However, our study uncovers some

trends which we believe can be probed in real materials.

We now discuss the transport coefficients for type-I mWSMs as shown in Fig. 5.1(a) for thermal Hall conductivity and Fig. 5.1(b) for Nernst conductivity. We depict the high frequency behavior of K_{xy} and α_{xy}, calculated using Eq. (5.33) and Eq. (5.34), respectively. Noticeably the response from the external field for a general $n > 1$ mWSM is not related to $n = 1$ single WSM by a simple multiplicative factor. This is also very clearly evident from the variation of K_{xy} and α_{xy} with driving frequency ω. The sub-leading terms play an important role due to the fact that the chemical potential μ gets non-trivially coupled to the frequency; these terms are associated with the factors β_2', β_3'. The important point to note here is that K_{xy} decreases and eventually saturates with optical frequency ω; while $|\alpha_{xy}|$ remains unchanged with ω for $n = 2$. In the case with $n = 3$, $|\alpha_{xy}|$ increases followed by a saturation at sufficiently large frequency. We note that even though $\beta_2'' = \beta_3'' = 0$ for both $n = 1$ and $n = 2$, K_{xy} depends on ω as first two terms in Eq. (5.33) due to the term Δ_n. The ω-independent nature of $\alpha_{xy}^{n=1}$ and $\alpha_{xy}^{n=2}$ stems from the fact that $\beta_2'' = \beta_3'' = 0$ in the leading order; the first term in Eq. (5.34) does not depend on ω. $\beta_2'', \beta_3'' \neq 0$ results in a further ω-dependent behavior of $\alpha_{xy}^{n=3}$. The absence and lower degree of anisotropy can thus lead to ω-independent nature of $\alpha_{xy}^{n=1}$ and $\alpha_{xy}^{n=2}$, respectively; substantial amount of anisotropy can significantly modify the light induced transport as observed in $\alpha_{xy}^{n=3}$. However, the crossing of $\alpha_{xy}^{n=3}$ with $\alpha_{xy}^{n=1}$ and $\alpha_{xy}^{n=2}$ might be restricted to the leading order and higher order corrections may be frequency dependent. We note that one needs to investigate the lattice model to get a more complete picture.

It is now important to analyze the behavior of K_{xy} as a function of α_{xy} since it could be useful from the experimental perspective. One can understand that K_{xy} and α_{xy} behave in an independent manner for $n = 1$ and $n = 2$ as K_{xy} depends on ω while α_{xy} does not. Interestingly, we see that this no longer holds for $n = 3$ and we plot

this in Fig. 5.2. Here, K_{xy} increases with $|\alpha_{xy}|$. A qualitative change in the transport character is observed with the increase in the degree of anisotropy, characterized by n.

Similarly, for type-II mWSMs, we depict the behavior of K_{xy}, obtained from Eq. (5.36), in Fig. 5.3 (a) and α_{xy}, obtained from Eq. (5.37), in Fig. 5.3 (b), respectively. One can find here for type-II mWSM, unlike the type-I mWSM, that K_{xy} and α_{xy} both decrease with ω. This may be due to the fact that they are influenced by the quadratic momentum cutoff Λ^2 dependent sub-leading term in addition to the terms containing the function $f(\mu, \omega, n)$.

Having thoroughly investigated the transport coefficients type-I and type-II mWSMs, we would now like to comment on the differences between these two phases in single WSM as far as the other magneto-transport conductivities are concerned. As a start, planar Hall coefficients vary quadratically (linearly) for type-I (type-II) single WSMs [114]. The type-I single WSMs can be differentiated from type-II while the anomalous Nernst and anomalous Hall conductivities are studied [38, 115]. The tilt also causes distinguishably different optical activities in Kerr and Faraday rotation as compared to the non-tilted case [116, 117]. Our study considering the low energy irradiated mWSM model further strengthens the list of distinction between these two types of mWSMs. The distinct behavior coming from type-I and type-II single Weyl lattice models which do not suffer from any cut-off dependence can thus be related to the different cut-off characteristics as derived in low energy model. Therefore, the tilt even in the presence of anisotropy is able to influence the transport properties in a different manner as compared to non-tilted case.

We now propose a relevant experimental setup where our predictions can be tested. One can have candidate double ($HgCr_2Se_4$) and triple WSM ($Rb(MoTe)_3$) materials as the samples. The Floquet driving can be realized by the conventional pump (strong beam)-probe (weak beam) optical set up where ultrafast electron dynamics

of the samples are observed as a function of time delay between the arrival of pump and probe pulses. Recently, using polarized photons at mid-infrared wavelengths, Floquet-Bloch states and photo-induced band gaps have been shown to be clearly visible in time-and-angle-resolved photoemission spectroscopy [95]. We believe that using similar arrangements with suitably chosen frequency ranges of pump laser, one can experimentally measure the transport properties derived here. One can also consider a non-optical substrate-terminal based closed circuit measurement of Nernst conductivity and thermal Hall conductivity [96] The electric and heat current can be measured considering a mutually perpendicular arrangement of DC power source and thermocouple, respectively.

Chapter 6

Conclusion

In this chapter, we summarize and make concluding remarks about the contents of this dissertation. Additionally, possible future research directions are addressed. The chapter is divided into two sections: the first section deals with quantum spin liquids while the second concerns Weyl semimetals.

6.1 Random Transverse Field Ising Model

In chapter 2, we have studied the random transverse-field Ising model on the pyrochlore lattice using NLC and ED. This model has a deconfined QSL phase, which is subject to two types of confining transitions. Large transverse-fields lead to confinement where spins are locked along the field direction. On the other hand, a distribution of random fields leads to a selection within the ice manifold also leading to a loss of entanglement and confinement. We have shown that local entanglement associated with a single-tetrahedron contains sharp changes associated with these transitions.

The simple NLC converges well in the high-field phase, right up to the transition. But, it diverges in the QSL phase. The QSL phase can be studied within NLC formalism by embedding each cluster inside a larger spin-ice. Nearly all the entanglement in

the QSL phase arises from ring-exchange resonances. These can be frozen by random transverse-fields leading to confinement.

In the confining phase, there is a broad distribution of local entanglement, a property which persists to large random fields. This suggests that such local behavior may be present in the material $Pr_2Zr_2O_7$, which has rather large random fields compared with exchange interactions, although a material with smaller random fields would be a better candidate for a QSL.

In chapter 3 we have studied an effective model derived perturbatively from the random transverse-field Ising model (RTFIM) on the pyrochlore lattice. The reduced Hilbert space of the effective model allows us to study larger system sizes and thus deduce the nature of different phases. We find three different phases. A U(1) QSL phase occurs for sufficiently small randomness at all h. At weak transverse-fields, increased randomness leads to an Ising spin-glass (ISG) phase, with nearly frozen spins and very little quantum fluctuations. Increased random-fields can lead to a random resonating hexagon (RRH) phase, which is a kind of a cluster-glass phase where quantum fluctuations and entanglement are restricted to small clusters.

We have discussed possible relevance of this study to rare-earth pyrochlores where RTFIM have been argued to be relevant. It is clear that a broad distribution of transverse-fields, with width exceeding the mean, will not lead to a QSL phase. But, it is possible for it to still be in a random resonating hexagon phase. It would be interesting if evidence of local resonating hexagons is observed in $Pr_2Zr_2O_7$. A true U(1) QSL would need a material where the magnitude of the transverse-field is nearly uniform at least at nearby sites, which could be the case if strain is the dominant source of disorder.

My current work focuses on the pyrochlore lattice, but in principle there are other frustrated geometries (for example the triangular lattice, Kagome lattice) that potentially host a degenerate space of vacuua. This manifold of ground states maybe

identified and then deformed (to mimic the effects of disorder) to give rise to macroscopic entanglement which can be studied using ED techniques and associated methods already present in my armory. Further, restricting to the reduced Hilbert space of degenerate ground states permits the study of much larger system sizes, otherwise inaccessible if the full Hilbert space of the underlying theory is necessary. The construction of phase diagrams for different classes of materials and geometries would be possible thereby equipping experimentalists with a potentially large set to choose from and identify the elusive QSLs.

One can also envision the properties of the QSL system under excitations induced by neutron scattering that may reveal signatures of the local structure of entanglement. A candidate observable to assess this is the dynamical structure factor (DSF), which could be compared to neutron-scattering data to identify such excitations. DSFs can becomputed to great accuracy without access to the full Hilbert space of states making it compatible with methods like the Lanczos algorithm. The DSF can also be used to compare the scattering based excitations existing in the phases neighboring the QSL as functions of the parameters, and very interestingly near the phase boundaries. Another viable option would be to compute the DSF in position space in the different phases of the candidate material, corresponding to the results obtained from NMR data.

6.2 Anomalous Floquet Transport in Weyl semimetals

In chapter 4 we have considered the effects of an incident circularly polarized optical field (CPL) on two distinct classes of Weyl Semimetals in the HFL using Floquet theory. The corresponding changes in thermal Hall conductivity and Nernst conductivity have been calculated for the linearized model, with closed form expressions for

the $T \to 0$ case. These results and the underlying physics can be summed up as follows.

For the effective Floquet Hamiltonian, we find that the Weyl nodes separate further due to the radiation field dependent parameter Δ. This also gives rise to a constant term in the Hamiltonian proportional to Δ, which leads to distinct shifts in the spectrum of each Weyl node and is shown to be equal in the inversion symmetric case. Thus, the effect of the latter is to change the effective Fermi surface leading to an array of consequences for the transport coefficients. The time-averaged transport coefficients are computed using the modified Kubo formalism applicable to Floquet states, and we show that the conductivity tensor can be computed using the Matsubara Green's function formalism, the key point being that the Kubo formula can be used in it's standard form with the states and energies in the expression being interpreted as the states and quasi energies of the effective Floquet Hamiltonian.

For the type-I WSM case, we find that the leading correction to the Hall conductivity arises from the Floquet parameter Δ. There exist subleading order corrections stemming from the true band structure which may not be accurately captured by the linearized model. The Nernst conductivity remains unchanged by the optical field because the Hall conductivty in the type-I regime shows a linear dependence on the chemical potential.

In the type-II case, we find that the Hall conductivity decreases with the amplitude of the incident laser beam, holding the frequency fixed. The Nernst conductivity for this type of WSM is affected by the radiation field as the thermal Hall conductivity depends non-linearly on the chemical potential. With increasing Δ, the Nernst conductivity falls off logarithmically. The qualitative and quantitative analyses of the transport properties of WSMs presented here aims to the characterization of the two types of WSMs.

In chapter 5 we have investigated the circularly polarized light (of amplitude A_0

and frequency ω) induced contributions to the thermo-electric transport coefficients in type-I and type-II mWSM with topological charge $n > 1$ considering the low energy minimal model. Using the high frequency expansion ($\omega \to \infty$) and appropriately employing the non-equilibrium Floquet-Matsubara formalism, where the energies and states of the Hamiltonian are replaced with the quasi-energy and quasi-states of the effective Hamiltonian, we study the anomalous thermal Hall conductivity and Nernst conductivity. The effective Floquet Hamiltonian suggests that the Weyl nodes, separated by Q in the momentum space for the static case, are further displaced by a distance $2\Delta_n \sim A_0^{2n}/\omega$. Importantly, the low energy Hamiltonian of Floquet mWSMs receive momentum dependent corrections in addition to the constant A_0^2 shift in the single $n = 1$ Floquet WSMs. This results in a change in the effective Fermi surface which in turn leads to an array of non-trivial consequences for the transport coefficients. The leading order contribution varies linearly with the topological charge and the chemical potential μ is displaced to $\mu - C\Delta_n$. The light induced transport phenomena in type-I, and type-II mWSMs become significantly different. In particular, one can show that optical conductivity increases with A_0 for type-I mWSMs, while it decreases with A_0 in the case of type-II mWSM. However, the leading order vacuum contribution to σ_{xy} remains topological, which we verify by calculating the Berry curvature induced anomalous Hall conductivity.

Going beyond the leading order contribution, we compute the effect of the momentum dependent correction term in the Fermi surface effects to the conductivity tensor. We find Floquet driving induced sub-leading contribution can show non-trivial algebraic dependence on the chemical potential μ as $\mu^{f(n)}$. Most surprisingly, unlike the case of type-II single WSMs, for type-II mWSMs, the Nernst and thermal Hall conductivity depends algebraically on the momentum cut-off. However, for type-I mWSMs, the Fermi surface contribution remain cut-off independent. Unlike the type-I single WSM, the Nernst conductivity for type-I mWSM depends on μ.

Combining all these, we graphically represent the variation of the total thermal Hall and Nernst conductivities as a function of the optical driving frequnecy by evaluating the analytical expression numerically. These suggest that type-I and type-II mWSM exhibit distinct behavior while the multi Weyl nature can also be captured vividly.

Next, we consider possible research avenues for the future. While we have considered the leading order contribution in perturbation theory to the tilted Weyl Hamiltonian, it may be possible to sum the van-Vleck series exactly to all orders in perturbation theory. This might also hold true for other topological systems in their respective minimal models, and exactly summing perturbation theory contributions to all orders may lead to interesting non-perturbative results, which may have far reaching consequences for the transport properties of such materials.

Also, the already developed formalism maybe useful in examining the properties of other exotic materials like nodal line semimetals (NLSM) and the more recent variant - surface line semimetals , using their effective low energy theories. In this context, we are currently examining the effect of circularly polarized light on a tilted NLSM. We find that the CPL induces a WSM phase with tilt correlated with the NLSM! This leads to a richer phase diagram with a gapped phase, a type-I WSM and a type-II WSM which are separated by a Lifshitz transition.

In conjunction with this, an examination of the non-equilibrium distribution functions generated due to the irradiation of a material is needed to derive transport coefficients which can be accurately compared to experimental measurements. While there has been some work in this direction using the Master equation formalism, more work is needed to rigorously establish the class of distributions that can exist in such out of equilibrium systems, and their potential experimental realization.

Based on the research avenues presented above, I look forward to more adventures with topological materials in my future career, and on that note this treatise is terminated.

Appendix A

Spin Ice - II: data

A.1 Results for different cluster sizes: 32 sites, 40 sites, 48 sites, and 64 sites

Here we present the results for 32 site, 40 site, 48 site, and 64 site lattice on the same plot for each physical quantity.

A.1.1 Bandwidth

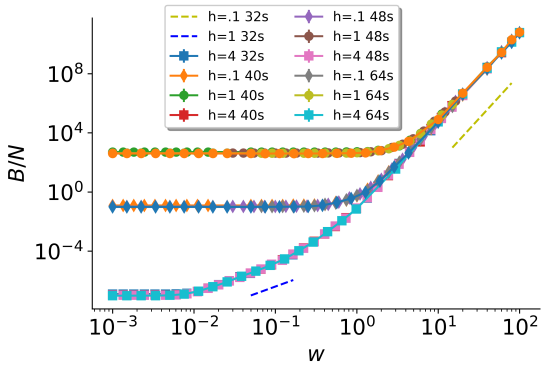

Figure A.1: The total Bandwidth of the spin-ice subspace per spin plotted on a log-log scale in the 32 site (32s), 40 site (40s), 48 site (48s), and 64 site (64s) clusters respectively. The yellow dashed line represents the scaling as w^6 in the RRH phase and the blue dashed line represent the ISG scaling as w^2.

A.1.2 Entanglement Entropy

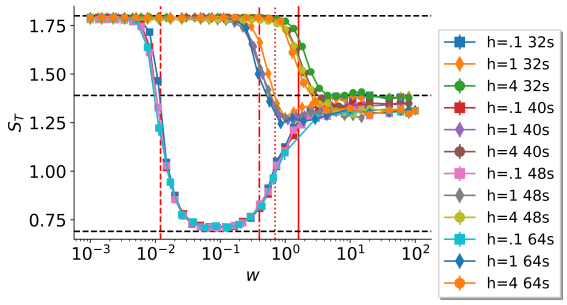

Figure A.2: Entanglement entropy for a tetrahedron of spins, S_T, for different parameters in the 32 site (32s), 40 site (40s), 48 site (48s), and 64 site (64s) clusters respectively. Vertical lines represent phase transitions. The red dashed lines represent the QSL to ISG phase transition for $h = .1$, the red dashed-dot line represents the QSL to RRH transition for $h = 1$, the red dotted line represents the ISG to RRH transition for $h = .1$, and the red solid line represents the QSL to RRH transition for $h = 4$. The horizontal dashed lines represent $\ln 6$, $2 \ln 2$, and $\ln 2$.

A.1.3 Ising Correlation

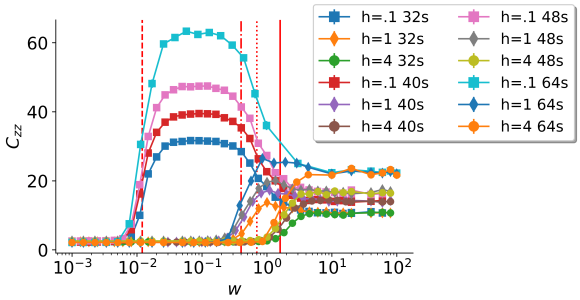

Figure A.3: Ising correlation sum in different parameter regions in the 32 site (32s), 40 site (40s), 48 site (48s), and 64 site (64s) clusters respectively. Vertical lines represent phase transitions. The red dashed lines represent the QSL to ISG phase transition for $h = .1$, the red dashed-dot line represents the QSL to RRH transition for $h = 1$, the red dotted line represents the ISG to RRH transition for $h = .1$, and the red solid line represents the QSL to RRH transition for $h = 4$.

A.1.4 Inverse Participation Ratio

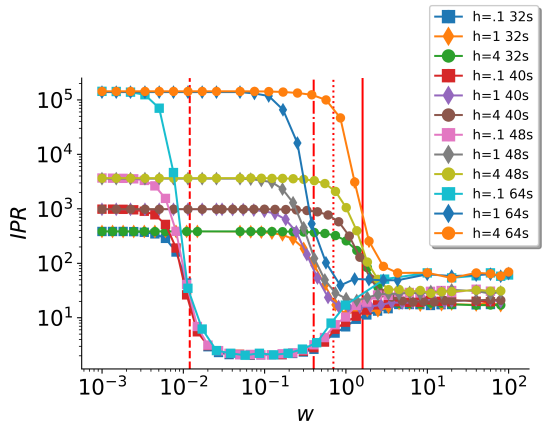

Figure A.4: Inverse Participation Ratio for different parameters in the 32 site (32s), 40 site (40s), 48 site (48s), and 64 site (64s) clusters respectively. Vertical lines represent phase transitions. The red dashed lines represent the QSL to ISG phase transition for $h = .1$, the red dashed-dot line represents the QSL to RRH transition for $h = 1$, the red dotted line represents the ISG to RRH transition for $h = .1$, and the red solid line represents the QSL to RRH transition for $h = 4$.

Appendix B

Floquet Weyl Semimetal

B.1 Floquet effective Hamiltonian

For the sake of completeness we provide a brief review of the Floquet theory. The off resonant condition (i.e. the presence of only virtual photon processes)[118, 119] is maintained here, which effectively makes the system stationary, and the static effective Hamiltonian in terms of the evolution operator U [77] is obtained as

$$\mathcal{H}_{eff}(k) = \frac{i\hbar}{T} \log U, \tag{B.1}$$

where,

$$U = T_{time} \exp[\frac{1}{i\hbar} \int_0^T \mathcal{H}(k,t)dt] \tag{B.2}$$

with T_{time} as the time-ordering operator. The effective Hamiltonian $\mathcal{H}_{eff}$ describes the dynamics of the system on the time scale much longer than a period T, thus the response is described well by an average over a period of oscillation. The matrix

elements of the time-dependent Floquet Hamiltonian is [72–77]

$$\mathcal{H}_F^{m,m'} = \mathcal{H}_0\delta_{m,m'} + m\hbar\omega\delta_{m,m'} + \mathcal{H}'_{m,m'} \tag{B.3}$$

where $\mathcal{H}'_{m,m'} = V_n = \frac{1}{T}\int_0^T \mathcal{V}(t)e^{i(m-m')t}dt = \frac{1}{T}\int_0^T \mathcal{V}(t)e^{in\omega t}dt$, where $\mathcal{V}(t)$ is the time dependent periodic perturbation term. Considering terms upto order $1/\omega$, the static time independent effective Hamiltonian is as follows

$$\mathcal{H}_{eff} = \mathcal{H}_0 + \frac{[V_{-1}, V_{+1}]}{\hbar\omega}. \tag{B.4}$$

Note that all higher multi-photon state contributions vanish identically for our system.

B.2 Modified Kubo Formula in the context of Floquet Theory

Given a time dependent Hamiltonian $\mathcal{H}(t)$ influenced by a driving periodic potential $A_d(t) = A_d(T + t)$, with T being the period, one can exploit the periodicity of the gauge potential to write the eigenstates of $\mathcal{H}(t)$ in the form [87]

$$|\Psi(t)\rangle = e^{-i\epsilon_\alpha t}\,|\Phi_\alpha(t)\rangle\,. \tag{B.5}$$

The states $|\Phi(t)\rangle$ are called Floquet states (analogous to the Bloch states for spatially periodic potentials) and they satisfy $|\Phi(t+T)\rangle = |\Phi(t)\rangle$. These states also satisfy the Schrodinger equation with ϵ_α's being the quasi-energies.

$$\mathcal{H}(t)\,|\Phi(t)\rangle = \epsilon_\alpha\,|\Phi(t)\rangle\,. \tag{B.6}$$

The Floquet states are orthonormal under a time averaged inner product defined as

$$\langle\langle \Phi_\alpha(t)|\Phi_\beta(t)\rangle\rangle := \frac{1}{T}\int_0^T dt\, \langle \Phi_\alpha(t)|\Phi_\beta(t)\rangle = \delta_{\alpha\beta}. \tag{B.7}$$

When applied to a system driven by an off-resonant optical field (i.e. the frequency ω of the field is larger than the bandwidth), real processes of photon absorption and emission cannot occur - this is why we stick to the high frequency regime, so that there is no dissipation. However, the off-resonant light can affect the system via virtual photon processes as described in [78]. The physics of such virtual processes can be captured order by order by Fourier transforming the Floquet states to momentum space.

$$|\Phi(t)\rangle = \sum_m e^{-im\Omega t}\,|u_\alpha^m\rangle \tag{B.8}$$

In the equation above, m is the Floquet index and it describes the order of the virtual photon process, while α is the band index for the full Hamiltonian. The states $|u_\alpha^n\rangle$ are related to the Floquet Hamiltonian as [87]

$$\sum_n \mathcal{H}_F^{mn}\,|u_\alpha^n\rangle = (\epsilon_\alpha + m\Omega)\,|u_\alpha^m\rangle\,, \tag{B.9}$$

with the Floquet Hamiltonian matrix elements defined as

$$\mathcal{H}_F^{mn} = \frac{1}{T}\int_0^T dt\mathcal{H}(t)e^{-i(m-n)\Omega t}. \tag{B.10}$$

The full Floquet Hamiltonian has a Sambe space [78] (equivalent to a Hilbert space but used in context of Floquet theory) given by $\mathbf{F} = \mathbf{\Omega} \otimes \mathbf{H_{2x2}}$, where $\mathbf{H_{2x2}}$ is the Hilbert space of the undriven Hamiltonian, and $\mathbf{\Omega}$ is the space corresponding which captures the different virtual photon processes. This Hamiltonian can be ap-

proximated to linear order in perturbation theory in the high frequency expansion (HFE) as $\mathcal{H}^F_{eff} = H_{0,0} + \frac{1}{\Omega}[\mathcal{H}^{-10}, \mathcal{H}^{10}]$, as used in our manuscript. The point of the effective Floquet Hamiltonian is that it shares the same quasi-energies and states of the full Floquet Hamiltonian to leading order in perturbation theory. The eigenstates of the effective Floquet Hamiltonian are defined as

$$\mathcal{H}^F_{eff} \left|e_\alpha\right\rangle = \epsilon_\alpha \left|e_\alpha\right\rangle , \tag{B.11}$$

and they are related to the Floquet states $|u^n_\alpha\rangle$ as

$$\left|e_\alpha\right\rangle = \sum_n \left|u^n_\alpha\right\rangle , \tag{B.12}$$

as shown in [55]. The authors of [87] state the form of the time-averaged conductivity tensor σ_{ab} in the form of the Kubo formula, modified for the Floquet states in Eqn. (B.6) as

$$\sigma_{ab} = i \int \frac{d\mathbf{k}}{(2\pi)^d} \sum_{\alpha \neq \beta} \frac{f_\beta(\mathbf{k}) - f_\alpha(\mathbf{k})}{\epsilon_\beta(\mathbf{k}) - \epsilon_\alpha(\mathbf{k})} \times \frac{\langle\langle \Phi_\alpha(\mathbf{k}) | J_b | \Phi_\beta(\mathbf{k}) \rangle\rangle \langle\langle \Phi_\beta(\mathbf{k}) | J_a | \Phi_\alpha(\mathbf{k}) \rangle\rangle}{\epsilon_\beta(\mathbf{k}) - \epsilon_\alpha(\mathbf{k}) + i\eta} \tag{B.13}$$

This is very similar to the Kubo formula with the following modifications: The energies have been replaced with the Floquet quasi-energies and the current correlation functions are time averaged. The f's are the Fermi distribution function which take on a non-universal character out of equilibrium. Given the system described in our work, the current operator defined as $J = \frac{\partial \mathcal{H}(t)}{\partial A^\mu} = \hbar C_s \delta_{\mu z} + s\hbar v \sigma_\mu$ is independent of time. We evaluate the current correlation function above using the Fourier decomposition of Eqn.(B.8) as

$$\begin{aligned}\langle\langle\Phi_\beta(\mathbf{k})|J|\Phi_\alpha(\mathbf{k})\rangle = \frac{1}{T}\int_0^T dt \sum_m \sum_n e^{-i\Omega(n-m)t}\langle u_\alpha^m|J|u_\beta^n\rangle \\ = \sum_m \sum_n \delta_{nm}\langle u_\alpha^m|J|u_\beta^n\rangle \\ = \sum_n \langle u_\alpha^n|J|u_\beta^n\rangle\,, \end{aligned} \tag{B.14}$$

where the simplification arises because the time dependent parts factor out.

As derived in [55] (section III), in the HFE we find that $|u_\alpha^n\rangle \sim \mathcal{O}(\omega^{-n})$, and so to leading order only the zeroth level Floquet states $|u_\alpha^0\rangle$ contribute. Now, $|u_\alpha^0\rangle$ is given in terms of the eigenstates of the effective Floquet Hamiltonian from Eqn.(B.12), and thus the current correlator in Eqn. (B.14) can be re-expressed as

$$\langle\langle\Phi_\beta(\mathbf{k})|J|\Phi_\alpha(\mathbf{k})\rangle = \sum_n \langle u_\alpha^n|J|u_\beta^n\rangle = \langle u_\alpha^0|J|u_\beta^0\rangle = \langle e_\alpha|J|e_\beta\rangle\,. \tag{B.15}$$

The main point here is that the expectation value of observables are correctly computed using the eigenstates of the effective Hamiltonian to leading order in perturbation theory. This brings the expression for the conductivity tensor on the r.h.s. of Eqn.(B.13) to exactly the Kubo form for the undriven case with the use of effective Floquet states and quasi-energies.

$$\sigma_{ab} = i\int \frac{d\mathbf{k}}{(2\pi)^d}\sum_{\alpha\neq\beta}\frac{f_\beta(\mathbf{k}) - f_\alpha(\mathbf{k})}{\epsilon_\beta(\mathbf{k}) - \epsilon_\alpha(\mathbf{k})} \times \frac{\langle e_\alpha(\mathbf{k})|J_b|e_\beta(\mathbf{k})\rangle\langle e_\beta(\mathbf{k})|J_a|e_\alpha(\mathbf{k})\rangle}{\epsilon_\beta(\mathbf{k}) - \epsilon_\alpha(\mathbf{k}) + i\eta} \tag{B.16}$$

Since the Kubo formula as stated above is identically expressed using the Matsubara Green's function approach, using the effective Floquet states and quasi-energies in the Matusbara formalism yeilds the same conductivities as the one computed using

Eqn.(B.16). In the undriven case, the Matsubara formalism uses the Green's function derived from the Hamiltonian, and here it will correspondingly require the use of the Green's function of the effective Floquet Hamiltonian.

We note that the Fermi distribution is not universal for systems which are out of equilibrium, but we claim that the contribution of the electrode chemical potential will be tiny in the regime of linear response theory as compared to the intrinsic chemical potential of the system, and so we ignore the electrode chemical potential. This allows us to write the chemical potential in the Kubo formalism as a constant i.e. without accounting for sources at the boundary.

Note also that one could have conducted the calculation above using an additional slowly varying gauge field, which is then subsequently set to zero as we take the zero-frequency limit in the Kubo formula (i.e. the linear response regime), as done by the authors of [87]

B.3 Hall Conductivity Computation using modified Kubo Formalism

The modified form of the Kubo formula as applicable to Floquet states of a strong and periodically driven system (derived in appendix B) is used in this appendix to compute the analytical form of the zero-temperature time-averaged components of the conductivity tensor. The time-averaged anomalous Hall conductivity for the tilted WSM under the action of the circularly polarized light may now be derived from the zero frequency and zero wave-vector limit (i.e. the limit of an infinitesimal d.c. bias) of the current-current correlation function, constructed using the Matsubara Green's

function method (with $\hbar = 1$):

$$\Pi_{ij}(\Omega, \mathbf{q}) = T \sum_{\omega_n} \sum_{s=\pm} \int \frac{d^3k}{(2\pi)^3} J_i^{(s)} G_s(i\omega_n, \mathbf{k}) J_j^{(s)} G_s(i\omega_n - i\Omega_m, \mathbf{k} - \mathbf{q}) \Big|_{i\Omega_m \to \Omega + i\delta} \quad \text{(B.17)}$$

where $i, j = \{x, y, z\}$, T is the temperature (setting the Boltzmann constant as unity) and $\omega_n(\Omega_m)$ are the fermionic(bosonic) Matsubara frequencies. Here $G_s(i\omega_n, \mathbf{k})$ is the single particle Green's function of the electron and $J_i^{(s)} = e\left(C_s \delta_{iz} + sv\sigma_i\right)$ is the current operator with δ_{ij} as the Kronecker delta. One can relate the Hall conductivity to the current-current correlation function as follows,

$$\sigma_{xy} = -\lim_{\Omega \to 0} \frac{\Pi_{xy}(\Omega, 0)}{i\Omega}. \quad \text{(B.18)}$$

The one-particle Green functions have the following form

$$G_s(i\omega_n, \mathbf{k}) = \frac{1}{2} \sum_{t=\pm 1} \frac{1 - st\boldsymbol{\sigma} \cdot \frac{\mathbf{k} - s(Q+\Delta)\mathbf{e}_z}{|\mathbf{k} - s(Q+\Delta)\mathbf{e}_z|}}{i\omega_n + \mu - C_s(k_z - s(Q+\Delta) + tv|\mathbf{k} - s(Q+\Delta)\mathbf{e}_z| - sC_s\Delta}, \quad \text{(B.19)}$$

where μ is the chemical potential. We sum over the Matsubara fermion frequencies and trace over Pauli σ-matrices to obtain the following form

$$\Pi_{xy}(\Omega, 0) = \Pi_{xy}^{(+)}(\Omega, 0) + \Pi_{xy}^{(-)}(\Omega, 0), \quad \text{(B.20)}$$

where we have separated the contributions from the two Weyl cones

$$\Pi_{xy}^{(s)}(\Omega,0) = \Pi_0^{(s)}(\Omega,0) + \Pi_{\rm FS}^{(s)}(\Omega,0), \tag{B.21}$$

$$\Pi_0^{(s)}(\Omega,0) = -se^2 \int_{-\Lambda_0 - s(Q+\Delta)}^{\Lambda_0 - s(Q+\Delta)} \frac{dk_z}{2\pi} \int_0^\infty \frac{k_\perp dk_\perp}{2\pi} \frac{2v^2\Omega_m}{\Omega_m^2 + 4v^2k^2} \times \frac{k_z}{k}\bigg|_{i\Omega_m \to \Omega + i\delta}, \tag{B.22}$$

$$\Pi_{\rm FS}^{(s)}(\Omega,0) = se^2 \int_{-\Lambda - s(Q+\Delta)}^{\Lambda - s(Q+\Delta)} \frac{dk_z}{2\pi} \int_0^\infty \frac{k_\perp dk_\perp}{2\pi} \frac{2v^2\Omega_m}{\Omega_m^2 + 4v^2k^2} \times \frac{k_z}{k}\Big\{ n_F(C_s k_z + vk - \mu + sC_s\Delta) - n_F(C_s k_z - vk - \mu + sC_s\Delta) + 1 \Big\}\bigg|_{i\Omega_m \to \Omega + i\delta}. \tag{B.23}$$

Π_0 denotes the vacuum contribution for $\mu = 0$, whereas $\Pi_{\rm FS}$ is the contribution of the states at the Fermi surface. $n_F(E) = (e^{(E-\mu)/T} + 1)^{-1}$ is the Fermi distribution function and $k = \sqrt{k_z^2 + k_\perp^2}$. The cut-off Λ_0, which is introduced in the k_z integral, is known not to affect the vacuum contribution to the Hall conductivity. However, the other cutoff in Π_{FS}^s,which is denoted as Λ, is crucial for finite Fermi surface effects in both the type-I and type-II regime.

Using eqn. (C.19), we have

$$\sigma_{xy}^{(s)} = \sigma_0^{(s)} + \sigma_{\rm FS}^{(s)}, \tag{B.24}$$

$$\sigma_0^{(s)} = -e^2 \int_{-\Lambda_0 - s(Q+\Delta)}^{\Lambda_0 - s(Q+\Delta)} \frac{dk_z}{2\pi} \int_0^\infty \frac{k_\perp dk_\perp}{2\pi} \frac{sk_z}{2k^3}, \tag{B.25}$$

$$\sigma_{\rm FS}^{(s)} = e^2 \int_{-\Lambda - s(Q+\Delta)}^{\Lambda - s(Q+\Delta)} \frac{dk_z}{2\pi} \int_0^\infty \frac{k_\perp dk_\perp}{2\pi} \times \frac{sk_z}{2k^3}\Big[n_F(C_s k_z + vk - \mu + sC_s\Delta) - n_F(C_s k_z - vk - \mu + sC_s\Delta) + 1 \Big]. \tag{B.26}$$

Importantly, one should note that $sk_z/2k^3$ is the z-component of the Berry curvature of the Weyl cone with chirality s. Interestingly, both the tilt C_s and the Floquet parameter Δ term has no effect on the Berry curvature component, but only affect

the Fermi-Dirac distribution function.

Taking the $T \to 0$, and performing the $k_\perp$ integration, we get

$$\sigma_0^{(s)} = -\frac{se^2}{8\pi^2}\int_{-\Lambda_0-s(Q+\Delta)}^{\Lambda_0-s(Q+\Delta)} dk_z\,\mathrm{sign}(k_z), \tag{B.27}$$

$$\sigma_{\mathrm{FS}}^{(s)} = -\frac{se^2}{8\pi^2}\int_{-\Lambda-s(Q+\Delta)}^{\Lambda-s(Q+\Delta)} dk_z\left[\mathrm{sign}(k_z) - \frac{vk_z}{|C_sk_z-\mu+sC_s\Delta|}\right] \times\left[\left(\Theta\left(v^2k_z^2-(C_sk_z+sC_s\Delta-\mu)^2\right)-1\right]\right., \tag{B.28}$$

where $\Theta(x)$ is the Heaviside function.

$$\sigma_{xy} = \sigma_0 + \sigma_{\mathrm{FS}} \tag{B.29}$$

$$\sigma_0 = -\frac{e^2}{4\pi^2}\int_{-\Lambda_0-(Q+\Delta)}^{\Lambda_0-(Q+\Delta)} dk_z\,\mathrm{sign}(k_z) = \frac{e^2}{2\pi^2}(Q+\Delta) \tag{B.30}$$

Noticeably, the optical field has lead to a positive offset to σ_0. In this case the Fermi surface contribution to the Hall effect can be written as

$$\sigma_{FS}^{s} = \frac{-se^2}{8\pi^2}\int_{-\Lambda-s(Q+\Delta)}^{\Lambda-s(Q+\Delta)} dk_z\left[\mathrm{sign}(k_z) - \frac{vk_z}{|C_sk_z-\mu+sC_s\Delta|}\left[\theta\Big(v^2k_z^2-\Big(C_sk_z+sC_s\Delta-\mu\Big)^2\Big)-1\right]\right] \tag{B.31}$$

The eq. (B.31) is nonzero only for $v^2k_z^2 - \Big(C_sk_z + sC_s\Delta - \mu\Big)^2 < 0$. Under this condition there will be two cases for type-I WSMs: i)$\mu - C\Delta > 0$ ii)$\mu - C\Delta < 0$

B.4 Schematic Design for Experimental Realization

We propose the use of the experimental setup in Fig. B.1 (of the appendix) above to test the validity of our results, where the WSM sample is connected to two metallic

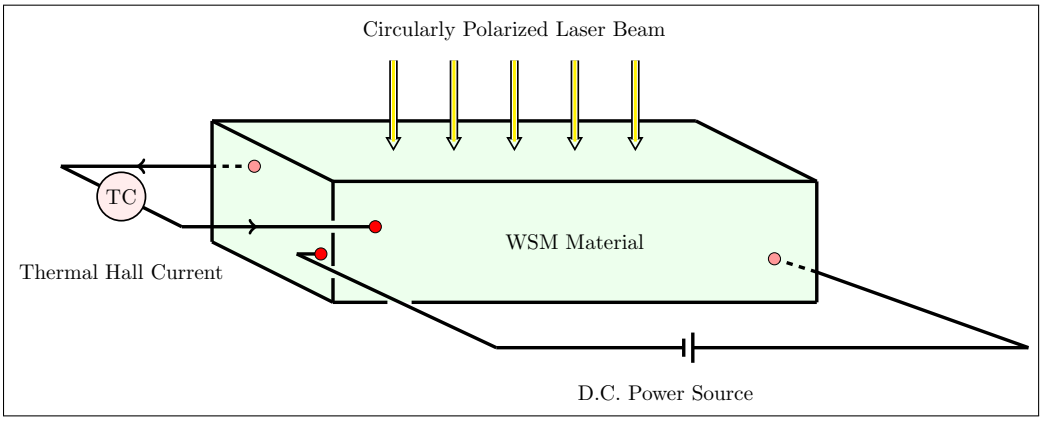

Figure B.1: A schematic for an pump-probe experiment to measure the anomalous thermal Hall conductivity of a WSM sample. TC represents a thermocouple which may be used to determine the temperature gradient which maps to the thermal Hall current.

leads which introduce a small d.c. bias (consistent with the use of linear response theory), and the thermocouple measures the transverse temperature gradient which is directly related to the thermal Hall current [37]. The circularly polarized irradiation field should possess a frequency governed by $-\omega/2 < E < \omega/2$, where E represents the band energy close to the Weyl points, i.e. in the linear dispersion regime. The purpose of the d.c. source is to induce a transverse Hall, and consequentially, an anomalous thermal Hall current.

In principle, one can design a pump-probe experiment, which serves the dual purpose of driving the system into a non-equilibrium state with high temporal resolution, as well as measuring the transport properties of the WSM sample. Note that the frequency of the pump pulse (ω_{pump}) is usually significantly smaller than the frequency of the optical field (ω), i.e. $\omega_{\text{pump}} << \omega$, and the high frequency ω implies that the Floquet bands are well separated [82], additionally increasing the precision of the high frequency expansion. For a choice of polarization of the optical field, the dispersion relation for this system can be verified using *time-resolved* angle-resolved photoemission spectroscopy (tr-ARPES [99, 100]. It is also possible to directly mea-

sure the Nernst and anomalous thermal Hall conductivities by conventional transport experiments [96–98], using the two distinct classes of WSMs used as samples.

Appendix C

Floquet multi-Weyl Semimetal

C.1 Lattice Hamiltonian

We now discuss a prototype lattice model for type-I mWSM that breaks TRS but remains invariant under inversion. Generalizing the low-energy effective Hamiltonian of a mWSM with broken TR symmetry, the corresponding lattice model can be written as [102]

$$H = \mathbf{N_k} \cdot \boldsymbol{\sigma} \tag{C.1}$$

For the single-WSM with $n = 1$, $\mathbf{N_k}$ takes the form $N_0 = t_0(\cos k_z + \cos k_x - 1)$, $N_x = t \sin k_x$, $N_y = t \sin k_y$, and $N_z = t_z \cos k_z - m_z + t_0(2 - \cos k_x - \cos k_y)$. We define $\boldsymbol{\sigma} = [\sigma_0, \sigma_x, \sigma_y, \sigma_z]$. In this model, the Weyl nodes are located at $\mathbf{k} = (0, 0, \pm k_0)$ with

$$\cos(k_0) = \frac{t_0}{t_z}\big[\frac{m_z}{t_0} + \cos k_x + \cos k_y - 2\big] \tag{C.2}$$

This model is found to be type-I for $t_0 < t_z$ and type-II for $t_0 \geq t_z/3$. One can expand the above Hamiltonian for $k_0 = \pm\pi/2$ with $m_z = 0$ to obtain the low energy Weyl Hamiltonian: $H_{n=1,s} \simeq t_0 k_z \sigma_0 + t(\sigma_x k_x + \sigma_y k_y) + t_z \sigma_z k_z$. The above Hamiltonian represents the single Weyl Hamiltonian around a given node s. Now combining the

chirality of the nodes and complete Weyl Hamiltonian, comprised of two nodes, looks like $H_{n=1} \simeq +\tau_z\sigma_0 t_0 k_z + t(\tau_z\sigma_x k_x + \tau_z\sigma_y k_y) + t_z\tau_z\sigma_z k_z$. Here, $\tau_z = \pm 1$ represents the chirality of the node, and it turns out the Hamiltonian is block diagonal. Therefore, one can simply work with a single 2×2 block Hamiltonian of the $H_{n=1,s} \simeq s(t_0 k_z\sigma_0 + t(\sigma_x k_x + \sigma_y k_y) + t_z\sigma_z k_z)$ with $s = \pm 1$. Since the Weyl points are located $(0, 0, \pm\pi/2)$ and the low energy model is considered around $(0, 0, 0)$ for convenience, one can write a single Weyl Hamiltonian without loss of generality in the following way:

$$H_{n=1,s} = C_s(k_z - sQ)\sigma_0 + s(v\sigma_x k_x + v\sigma_y k_y) + v'\sigma_z(k_z - sQ) \tag{C.3}$$

with $C_s = st_0, v = t, v' = st_z, Q = \pi/2$ and $s = \pm 1$. When $|C_s/v'| \ll 1$ ($|C_s/v'| \gg 1$), this model becomes type-I (type-II) single WSM. In the main text, Hamiltonian (1) reduces to the above form with $n = 1$.

On the other hand, in the case of double-WSM ($n = 2$), the form of N_k becomes $N_0 = t_0(\cos k_z + \cos k_x - 1)$, $N_x = t(\cos k_x - \cos k_y)$, $N_y = t \sin k_x \sin k_y$ and $N_z = t_z \cos k_z - m_z + t_0(6 + \cos 2k_x + \cos 2k_y - 4\cos k_x - 4\cos k_y)$. The lattice model of double-WSM contains two Weyl nodes at $(0, 0, \pm k_0)$ with

$$\cos(k_0) = \frac{t_0}{t_z}\big[\frac{m_z}{t_0} - (6 + \cos 2k_x + \cos 2k_y - 4\cos k_x - 4\cos k_y)\big] \tag{C.4}$$

One can similarly expand the above Hamiltonian around $k_0 = \pm\pi/2$ and $m_z = 0$. In this case, the low energy Hamiltonian for double-WSM with a given chirality s is written as $H_{n=2,s} \simeq t_0 k_z\sigma_0 + \frac{t}{2}(\sigma_x(k_x^2 - k_y^2) + \sigma_y k_x k_y)) + t_z\sigma_z k_z$. The complete Hamiltonian, comprised of two nodes s and s' is then given by $H_{n=2,s,s'} = \tau_z H_{n=2,s=+1}$. Therefore, the 2×2 compact form of the Hamiltonian where the Weyl points are located at $(0, 0, sQ)$ is given by

$$H_{n=2} = C_s(k_z - sQ)\sigma_0 + s(v\sigma_x(k_x^2 - k_y^2) + 2v\sigma_y k_x k_y)) + v'\sigma_z(k_z - sQ) \tag{C.5}$$

with $C_s = st_0, v = t/2, v' = st_z, Q = \pi/2$ and $s = \pm 1$. When $|C_s/v'| \ll 1$ ($|C_s/v'| \gg 1$), this model becomes type-I (type-II) single WSM. In the main text, Hamiltonian (1) reduces to the above form with $n = 2$.

Similarly, for a triple-WSM with topological charge $n = 3$, one should replace N_k by $N_0 = t_0(\cos k_z + \cos k_x - 1)$, $N_x = t \sin k_x(1 - \cos k_x - 3(1 - \cos k_y))$, $N_y = -t \sin k_y(1 - \cos k_y - 3(1 - \cos k_x))$ and $N_z = t_z \cos k_z - m_z + t_0(6 + \cos 2k_x + \cos 2k_y - 4\cos k_x - 4\cos k_y)$. Here, the Weyl points are appeared at $\mathbf{k} = (0, 0, \pm k_0)$. The gap closing point can be found at $m_z = 0$ with $k_z = \pi/2$. The low energy triple-WSM Hamiltonian is given by $H_{n=3,s} \simeq t_0 k_z \sigma_0 + \frac{t}{2}(\sigma_x(k_x^3 - 3k_x k_y^2) - \sigma_y(k_y^3 - 3k_x^2 k_y)) + v_z \sigma_z k_z$. The complete Hamiltonian, comprised of two nodes s and s' is then given by $H_{n=3,s,s'} = \tau_z H_{n=3,s=+1}$. Therefore, the 2×2 compact form of the Hamiltonian where the Weyl points are located at $(0, 0, sQ)$ is given by

$$H_{n=3} = C_s(k_z - sQ)\sigma_0 + s(v\sigma_x(k_x^3 - 3k_x k_y^2) + v\sigma_y(k_y^3 - 3k_x^2 k_y)) + v'\sigma_z(k_z - sQ) \quad \text{(C.6)}$$

with $C_s = st_0, v = t/2, v' = st_z, Q = \pi/2$ and $s = \pm 1$. When $|C_s/v'| \ll 1$ ($|C_s/v'| \gg 1$), this model becomes type-I (type-II) single WSM. In the main text, Hamiltonian (1) reduces to the above form with $n = 3$. Therefore, a minimal block diagonal four-band model such that the two blocks describe two minimal mWSM Hamiltonian of opposite chiralities $s = \pm 1$ whose Weyl nodes are located at different points in momentum space. We note that the Weyl nodes appear at the same energy for both the types of mWSMs.

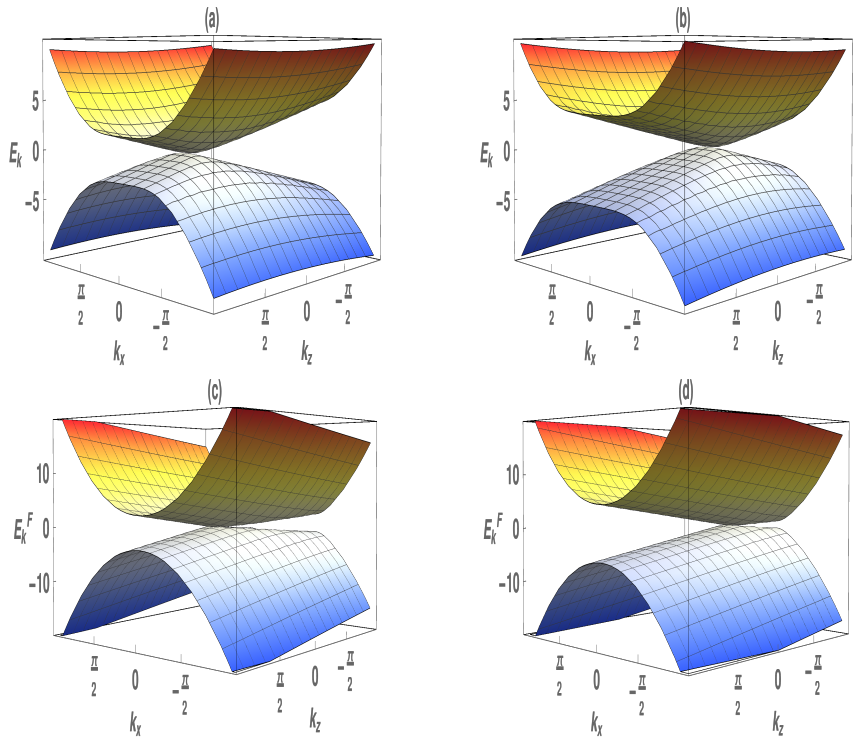

Figure C.1: (Color online) Plot shows the static double Weyl dispersion for $s = +1$ in (a) and $s = -1$ in (b) while the Floquet double Weyl dispersion are depicted for $s = +1$ in (c) and $s = -1$ in (d). The parameters considered here are $A_0 = 1.0$, $\omega = 10.0$, $k_y = 0.0$, $Q = 1.0$, $C_s = 0.0$ and $v = \alpha_n = 1$. The Floquet dispersion clearly shows the chirality dependent movement of the Weyl points. As is convention throughout the manuscript, all values are considered in Natural units.

C.2 Comparison between static and Floquet dispersion

C.2.1 Numerical Analysis

In what follows, we analyze the static and the Floquet dispersions for type-I and type-II m-WSMs. We first the study $n = 2$ type-I case in Fig. C.1 (a), (b) for static case and Fig. C.1 (c), (d) for irradiated case. The anisotropic nature is clearly visible from the static dispersion, obtained from Eq. (1) of the main text, for both the chirality $s = \pm 1$. Investigating the Floquet dispersion, calculated using Eq. (6), one can find that the Weyl nodes receive a chirality dependent shift in their position inside the Brillouin zone. In addition, the nature of Floquet dispersion is characteristically different from static dispersion as the driving term consists of $k_\perp$, n, A_0 and ω. Therefore, the static anisotropic multi Weyl nature of dispersion becomes ever more complex after the introduction of light. For type-II, we repeat the calculation in Fig. C.2. The anisotropic nature of multi Weyl dispersion gets tilted in the k_z direction. Two Weyl nodes with opposite chirality have opposite tilt orientation. The light can modify the position of the Weyl nodes; however, orientation of the tilt remains unaltered. Similar to the type-I case, the dispersion changes as far as the anisotropic nature is concerned. Therefore, Floquet driving does not open up a gap for Weyl systems irrespective of the types rather it moves the Weyl points in an anisotropic manner.

We now analyze the triple Weyl semi-metal in Fig. C.3 for type-I and Fig. C.4 for type-II. In both the cases, we observe a shift in the Weyl point position and the nature of the dispersion gets non-trivially modified upon the introduction of the light. Compared to $n = 2$ case, the static and Floquet dispersion near the Weyl points appear to be less dispersive as the higher $k_\perp$ momentum modes changes slowly $k_\perp \to 0$. On the other hand, away from Weyl points with finite $k_\perp$, the energy grows

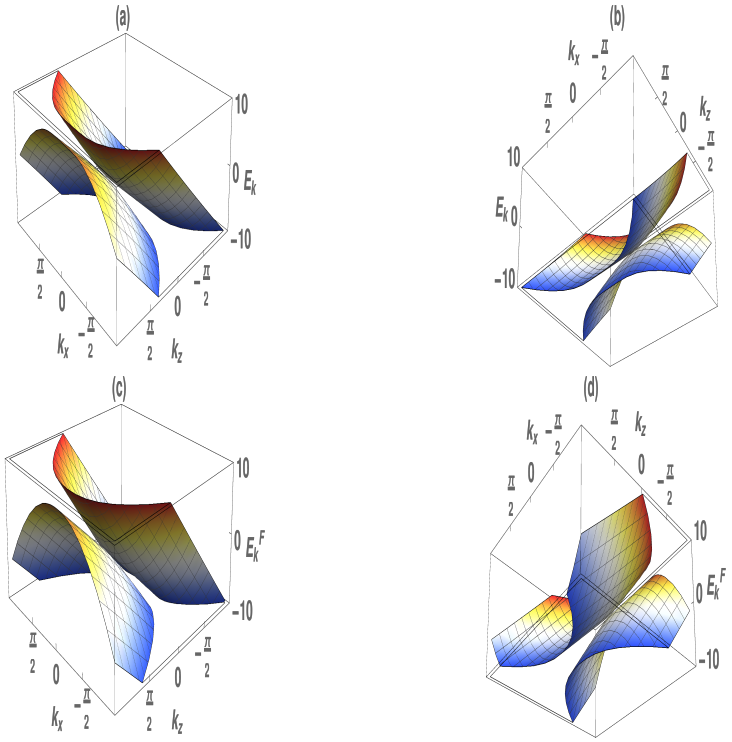

Figure C.2: (Color online) We repeat Fig. C.1 with the tilt parameter $C_s = 5.0$. The position of the Weyl nodes changes from their static positions. As is convention throughout the manuscript, all values are considered in Natural units.

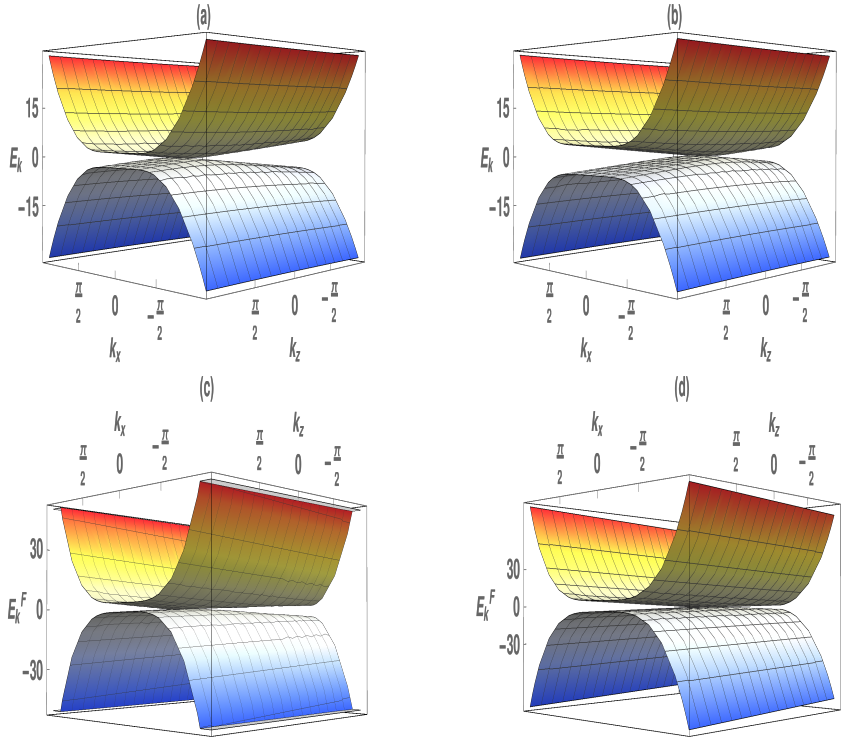

Figure C.3: (Color online) Plot shows the static triple Weyl dispersion for $s = +1$ in (a) and $s = -1$ in (b) while the Floquet triple Weyl dispersion are depicted for $s = +1$ in (c) and $s = -1$ in (d). The parameters considered here are $A_0 = 0.50$, $\omega = 10.0$, $k_y = 0.0$, $Q = 1.0$, $C_s = 0.0$ and $v = \alpha_n = 1$. The Floquet dispersion clearly shows the chirality dependent movement of the Weyl points. As is convention throughout the manuscript, all values are considered in Natural units.

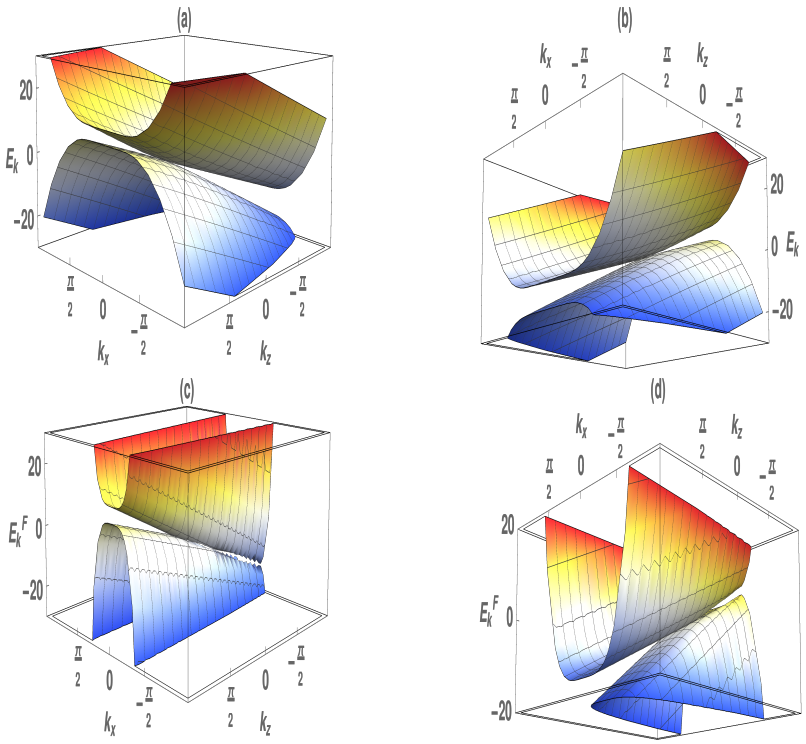

Figure C.4: (Color online) We repeat Fig. C.3 with the tilt parameter $C_s = 5.0$. The position of the Weyl nodes changes from their static positions. As is convention throughout the manuscript, all values are considered in Natural units.

faster for $n = 3$ as compared to $n = 2$. The light induced modification would make the transport properties to be dependent on chemical potential μ and parameters of the light i.e., A_0 and ω. We note that Weyl points of opposite chirality for both the types of irradiated mWSMs appear at the same energy. The single WSMs also exhibits similar feature under irradiation. The striking difference of $n > 1$ mWSMs from $n = 1$ single WSM is that k_z couples with $k_\perp$ in the Floquet dispersion of mWSMs.

C.2.2 Analytical proof of ungapped Floquet spectrum

We present an analytical proof that the Floquet spectrum of the mWSMs used in our system remains ungapped. To do this we note that the spectrum is given by,

$$E^F_{\mathbf{k}}(n,t,s) = C_s(k_z - sQ) + st\sqrt{\alpha_n^2 k_\perp^2 + T_{\mathbf{k}}^2}, \tag{C.7}$$

which is identical to Eq. (7) of the manuscript, with $t = \pm$ representing the valley degrees of freedom, and $T_{\mathbf{k}}$ being defined as

$$T_{\mathbf{k}} = v(k_z - sQ) + \frac{\alpha_n^2}{\omega}\sum_{p=1}^{n-1}\beta_p^n k_\perp^{2(n-p)} + \Delta_n. \tag{C.8}$$

Note that $k_\perp = \sqrt{k_x^2 + k_y^2} \geq 0$. In order for the system to be ungapped the upper band ($t = +$, conduction band), must touch the lower band ($t = -$, valence band) at atleast one point for a fixed chirality s. Imposing the condition $E^F_{\mathbf{k}}(n,+,s) = E^F_{\mathbf{k}}(n,-,s)$, we find that:

$$\alpha_n^2 k_\perp^2 + \left[(k_z - sQ) + \frac{\alpha_n^2}{\omega}\sum_{p=1}^{n-1}\beta_p^n k_\perp^{2(n-p)} + \Delta_n\right]^2 = 0. \tag{C.9}$$

We note that this equation has a solution at $k_\perp = 0$ and $k_z = sQ - \Delta_n$. Here, we have rescaled $k_z \to k_z/v$ as also used in the main text. Thus the mWSM Floquet spectrum is always ungapped for both type-I and type-II phases. In agreement with the previous discussion, we find that the Weyl nodes appear at the same energy.

C.3 Alternative definition of current operator

One can alternatively obtain the above current operator by using the Floquet-Kubo formula. We use Fourier component J_l^μ instead of the real time version $J_\mu(\mathbf{A},t)$. Here, $J_\mu(\mathbf{A},t)$ is defined from $H^s_{\mathbf{k}}(\mathbf{A},t)$ in Eq.(3) of the manuscript.

$$J_\mu(\mathbf{A},t) = e\frac{\partial H^s_{\mathbf{k}}(\mathbf{A},t)}{\partial k_\mu} \tag{C.10}$$

We define the Fourier expansion of $\hat{\mathbf{J}}$ in frequency space as $J_\mu(\mathbf{A},t) = \sum_l e^{-il\Omega t} J_l^\mu$. We get

$$J_x(\mathbf{A},t) = sen\alpha_n \sum_{q=0}^{n-1} \begin{bmatrix} 0 & {}^{n-1}C_q (ieA_0 e^{i\omega t})^{n-q-1} (k_\perp e^{-i\phi})^q \\ {}^{n-1}C_q (-ieA_0 e^{-i\omega t})^{n-q-1} (k_\perp e^{i\phi})^q & 0 \end{bmatrix}$$

$$J_y(\mathbf{A},t) = sen\alpha_n \sum_{q=0}^{n-1} \begin{bmatrix} 0 & -i^{n-1}C_q (ieA_0 e^{i\omega t})^{n-q-1} (k_\perp e^{-i\phi})^q \\ i^{n-1}C_q (-ieA_0 e^{-i\omega t})^{n-q-1} (k_\perp e^{i\phi})^q & 0 \end{bmatrix}$$

The time averaged current operators are given by

$$\begin{aligned} \langle\langle \Phi_\alpha(k)|J_\mu|\Phi_\beta(k)\rangle\rangle &= \frac{1}{T}\int_0^\infty dt \\ &\times \sum_{m,n,l} e^{-i\Omega(m-n-l)t} \langle u_\alpha^m|J_\mu|u_\beta^n\rangle \\ &\approx \langle u_\alpha^0|J_\mu^0|u_\beta^0\rangle \end{aligned} \tag{C.11}$$

Here, we take into account that the leading order contribution can only come from the zeroth level Floquet states $|u_\beta^0\rangle$ as $|u_\beta^n\rangle \sim \mathcal{O}(\omega^{-n})$.

C.4 Hall Conductivity Computation using modified Kubo Formalism

The modified form of the Kubo formula as applicable to Floquet states of a strong and periodically driven system (derived in appendix B) is used in this appendix to compute the analytical form of the zero-temperature time-averaged components of the conductivity tensor. The time-averaged anomalous Hall conductivity for the tilted WSM under the action of the circularly polarized light may now be derived from the

zero frequency and zero wave-vector limit (i.e. the limit of an infinitesimal d.c. bias) of the current-current correlation function, constructed using the Matsubara Green's function method (with $\hbar = 1$):

$$\Pi_{ij}(\Omega, \mathbf{q}) = T \sum_{\omega_p} \sum_{s=\pm} \int \frac{d^3k}{(2\pi)^3} J_i^{(s)} G_s(i\omega_p, \mathbf{k}) J_j^{(s)} G_s(i\omega_p - i\Omega_m, \mathbf{k} - \mathbf{q}) \Big|_{i\Omega_m \to \Omega + i\delta} \quad \text{(C.12)}$$

where $i, j = \{x, y, z\}$, T is the temperature (setting the Boltzmann constant as unity) and $\omega_p(\Omega_m)$ are the fermionic(bosonic) Matsubara frequencies. Here $G_s(i\omega_p, \mathbf{k})$ is the single particle Green's function of the electron and $J_i^{(s)} = esn\alpha_n k_\perp^{n-1}[(\cos(n-1)\phi_{\mathbf{k}})\sigma_i \pm (\sin(n-1)\phi_{\mathbf{k}})\sigma_j]$ is the current operator with $i, j = \{x, y\}$. For mWSM, $J_{x,y}$ both depends on $\sigma_{x,y}$ unlike the $n = 1$ case. Using the short hand notation $J_{x(y)} = esn\alpha_n k_\perp^{n-1}(J_{x(y),1}\sigma_1, J_{x(y),2}\sigma_2)$, one can find $J_{x,1} = \cos(n-1)\phi_{\mathbf{k}}$, $J_{x,2} = \sin(n-1)\phi_{\mathbf{k}}$, $J_{y,1} = -\sin(n-1)\phi_{\mathbf{k}}$, $J_{y,2} = \cos(n-1)\phi_{\mathbf{k}}$. One can relate the Hall conductivity to the current-current correlation function as follows,

$$\sigma_{xy} = -\lim_{\Omega \to 0} \frac{\Pi_{xy}(\Omega, 0)}{i\Omega}. \quad \text{(C.13)}$$

The one-particle Green functions have the following form

$$\begin{aligned} G_s(i\omega_p, \mathbf{k}) &= \frac{1}{2} \sum_{t=\pm 1} \frac{1 - t\mathbf{n}'_{\mathbf{k}}/|\mathbf{n}'_{\mathbf{k}}|}{\mathcal{X} - t\mathbf{n}'_{\mathbf{k}}} \\ &= \frac{1}{2} \sum_{t=\pm 1} \frac{1 - st\boldsymbol{\sigma} \cdot \frac{\mathbf{n}'_{\mathbf{k}} - s(Q+\Delta_n)\mathbf{e}_z}{|\mathbf{n}'_{\mathbf{k}} - s(Q+\Delta_n)\mathbf{e}_z|}}{i\omega_p + \mu - C_s(k_z - s(Q+\Delta_n) + tv|\mathbf{n}'_{\mathbf{k}} - s(Q+\Delta_n)\mathbf{e}_z| - sC_s\Delta_n} \end{aligned} \quad \text{(C.14)}$$

where μ is the chemical potential. Here, $\mathbf{n}'_{\mathbf{k}} = (\alpha_n k_\perp^n \cos(n\phi_{\mathbf{k}}), \alpha_n k_\perp^n \sin(n\phi_{\mathbf{k}}), T'_{\mathbf{k}}/\alpha_n)$. We refer, $T'_{\mathbf{k}} = vk_z + \frac{\alpha_n^2}{\omega} \sum_{p=1}^{n-1} \beta_p^n k_\perp^{2(n-p)}$ and $\Delta_n = \frac{\alpha_n^2}{n\omega} A_0^{2n}$. Here, $\beta_p^n = ({}^nC_p A_0^2)^p/p$. $\mathcal{X} = i\omega_p + \mu - C_s(k_z - sQ - s\Delta_n)$. We note that in the main text, we refer $T_{\mathbf{k}} = T'_{\mathbf{k}} + \Delta_n$ and $\mathbf{n}_{\mathbf{k}} = (\alpha_n k_\perp^n \cos(n\phi_{\mathbf{k}}), \alpha_n k_\perp^n \sin(n\phi_{\mathbf{k}}), T_{\mathbf{k}}/\alpha_n) = \mathbf{n}'_{\mathbf{k}} + (0, 0, \Delta_n/\alpha_n)$. Since Δ_n is independent of $k_\perp$, we can absorb Δ_n in the k_z momentum cut off Λ:

$\Lambda \to \Lambda - \Delta_n$. We here note that we shall use the cylindrical polar co-ordinate $\int d^3k \to \int k_\perp dk_\perp \int dk_z \int d\phi$. After a few steps of detail calculation, considering the fact $\int_0^{2\pi} d\phi \sin(M\phi) = \int d\phi \cos(M\phi) = 0$ with $M \geq 1$, the $\Pi_{xy}(\Omega, 0)$ becomes

$$\Pi_{xy}(\Omega,0) = T\frac{e^2n^2\alpha_n^2}{4\pi^2}\sum_{s,t,u}\int_0^\infty dk_\perp k_\perp^{2n-1}\int_{-\Lambda-s(Q+\Delta_n)}^{\Lambda-s(Q+\Delta_n)} dk_z \int_0^{2\pi} d\phi \frac{\frac{i}{2}(t-u)[\epsilon^{abc}J_{x,a}J_{y,b}T'_{\mathbf{k}}]}{(\mathcal{X}-t\mathbf{n}'_{\mathbf{k}})(\mathcal{X}-u\mathbf{n}'_{\mathbf{k}})} \tag{C.15}$$

with $J_{i,j}$ is the j-th component of current J_i. Now using the Matsubara Fermionic sum, one can show

$$T\sum_{\omega_p}\frac{1}{(\mathcal{X}-t\mathbf{n}'_{\mathbf{k}})(\mathcal{X}-u\mathbf{n}'_{\mathbf{k}})} = \frac{n_F(E_n^t)-n_F(E_n^u)}{E_n^t-E_n^u} \tag{C.16}$$

We get the finite contribution only from $u = -t$ and $u = \pm$.

We sum over the Matsubara fermion frequencies and trace over Pauli σ-matrices to obtain the following form

$$\Pi_{xy}(\Omega,0) = \Pi_{xy}^{(+)}(\Omega,0) + \Pi_{xy}^{(-)}(\Omega,0), \tag{C.17}$$

where we have separated the contributions from the two Weyl cones

$$\Pi_{xy}^{(s)}(\Omega,0) = \Pi_0^{(s)}(\Omega,0) + \Pi_{\rm FS}^{(s)}(\Omega,0), \tag{C.18}$$

$$\Pi_0^{(s)}(\Omega,0) = -se^2n^2\alpha_n^2\int_{-\Lambda_0-s(Q+\Delta_n)}^{\Lambda_0-s(Q+\Delta_n)}\frac{dk_z}{2\pi}\int_0^{\Lambda_1\to\infty}\frac{k_\perp^{2n-1}dk_\perp}{2\pi}\frac{2v^2\Omega_m}{\Omega_m^2+4|\mathbf{n}'_{\mathbf{k}}|^2} \times\frac{T'_{\mathbf{k}}}{|\mathbf{n}'_{\mathbf{k}}|}\Big|_{i\Omega_m\to\Omega+i\delta}, \tag{C.19}$$

$$\Pi_{\rm FS}^{(s)}(\Omega,0) = se^2n^2\alpha_n^2\int_{-\Lambda-s(Q+\Delta_n)}^{\Lambda-s(Q+\Delta_n)}\frac{dk_z}{2\pi}\int_0^{\infty}\frac{k_\perp^{2n-1}dk_\perp}{2\pi}\frac{2v^2\Omega_m}{\Omega_m^2+4|\mathbf{n}'_{\mathbf{k}}|^2} \times\frac{T'_{\mathbf{k}}}{|\mathbf{n}'_{\mathbf{k}}|}\Big\{n_F(C_sk_z+|\mathbf{n}'_{\mathbf{k}}|-\mu+sC_s\Delta_n)-n_F(C_sk_z-|\mathbf{n}'_{\mathbf{k}}|-\mu+sC_s\Delta_n)+1\Big\}\Big|_{i\Omega_m\to\Omega+i\delta}. \tag{C.20}$$

Here, Λ_1 is cut-off considered for $k_\perp$ integral. Π_0 denotes the vacuum contribution for

$\mu = 0$, whereas $\Pi_{\rm FS}$ is the contribution of the states at the Fermi surface. $n_F(E) = (e^{(E-\mu)/T}+1)^{-1}$ is the Fermi distribution function and $|\mathbf{n}'_{\mathbf{k}}| = \sqrt{(T'_{\mathbf{k}})^2 + \alpha_n^2 k_\perp^{2n}}$. The cut-off Λ_0, which is introduced in the k_z integral, is known not to affect the vacuum contribution to the Hall conductivity. However, the other cutoff in Π^s_{FS},which is denoted as Λ, is crucial for finite Fermi surface effects in both the type-I and type-II regime.

Using eqn. (C.19), we have

$$\sigma^{(s)}_{xy} = \sigma^{(s)}_0 + \sigma^{(s)}_{\rm FS}, \tag{C.21}$$

$$\sigma^{(s)}_0 = -e^2 n^2 \alpha_n^2 \int_{-\Lambda_0 - s(Q+\Delta_n)}^{\Lambda_0 - s(Q+\Delta_n)} \frac{dk_z}{2\pi} \int_0^{\Lambda_1 \to \infty} \frac{k_\perp^{2n-1} dk_\perp}{2\pi} \frac{sT'_{\mathbf{k}}}{2|\mathbf{n}'_{\mathbf{k}}|^3}, \tag{C.22}$$

$$\sigma^{(s)}_{\rm FS} = e^2 n^2 \alpha_n^2 \int_{-\Lambda - s(Q+\Delta_n)}^{\Lambda - s(Q+\Delta_n)} \frac{dk_z}{2\pi} \int_0^{\infty} \frac{k_\perp^{2n-1} dk_\perp}{2\pi}$$
$$\times \frac{sT'_{\mathbf{k}}}{2|\mathbf{n}'_{\mathbf{k}}|^3} \Big[n_F(C_s k_z + |\mathbf{n}'_{\mathbf{k}}| - \mu + sC_s\Delta_n) - n_F(C_s k_z - |\mathbf{n}'_{\mathbf{k}}| - \mu + sC_s\Delta_n) + 1 \Big]. \tag{C.23}$$

Having obtained these equation, we now have to approximate the expression $\frac{sT'_{\mathbf{k}}}{2|\mathbf{n}'_{\mathbf{k}}|^3}$ considering the leading order contribution around the bare term $vk_z/E^3_{\mathbf{k}}$ with $E_{\mathbf{k}} = \sqrt{k_\perp^2 + v^2 k_z^2}$. Before that, in order to simply the calculation, we use the following change of varibale $k_\perp \to k_\perp^{\frac{1}{n}} \alpha_n^{-\frac{1}{n}}$. Under these transformation: $T'_{\mathbf{k}} = vk_z + \frac{\alpha_n^2}{\omega} \sum_{p=1}^{n-1} \beta_p^n \alpha_n^{\frac{2(p-n)}{n}} k_\perp^{\frac{2(n-p)}{n}}$ with $\beta_p^n = ({}^nC_p A_0^2)^p/p$ and $\alpha_n^2 k_\perp^{2n} = k_\perp^2$. In the following approximation, we consider the fact $\omega \to 0$ due to high frequency expansion of the Floquet effective Hamiltonian and hence, $\mathcal{O}(\omega^{-q})$, $q > 1$ terms are neglected. Therefore the denominator $|\mathbf{n}'_{\mathbf{k}}| = \sqrt{k_\perp^2 + (T'_{\mathbf{k}})^2}$ becomes

$$k_\perp^2 + (T'_{\mathbf{k}})^2 \approx E^2_{\mathbf{k}} + \frac{2vk_z\alpha_n^2}{\omega} \sum_{p=1}^{n-1} \frac{1}{p} ({}^nC_p A_0^2)^p \alpha_n^{\frac{2(p-n)}{n}} k_\perp^{\frac{2(n-p)}{n}} \tag{C.24}$$

Now, the main integrand is thus given by

$$\frac{T_{\mathbf{k}}}{(k_\perp^2+T_{\mathbf{k}}^2)^{3/2}} \approx \frac{1}{E_{\mathbf{k}}^3}(vk_z - \frac{3v^2k_z^2\alpha_n^2}{E_{\mathbf{k}}^2\omega}X_{\mathbf{k}} + \frac{\alpha_n^2}{\omega}X_{\mathbf{k}}(1-\frac{3vk_z\alpha_n^2}{E_{\mathbf{k}}^2\omega}X_{\mathbf{k}})) \quad \text{(C.25)}$$

with $X_{\mathbf{k}} = \sum_{p=1}^{n-1}\beta_p^n\alpha_n^{\frac{2(p-n)}{n}}k_\perp^{\frac{2(n-p)}{n}}$. For $n=2$, $X_{\mathbf{k}} = \beta_1^n\alpha^{-2/n}k_\perp^{2/n}$ and for $n=3$, $X_{\mathbf{k}} = \beta_1^n\alpha^{-4/n}k_\perp^{4/n} + \beta_2^n\alpha_n^{-2/n}k_\perp^{2/n}$. It is then more convenient to write $T'_{\mathbf{k}}$ explicitly for $n=2$ as $T'_{\mathbf{k}} = vk_z + \beta_1^n\alpha_n^{-2/n}k_\perp^{2/n}$ and for $n=3$ as $T'_{\mathbf{k}} = vk_z + \beta_1^n\alpha_n^{-4/n}k_\perp^{4/n} + \beta_2^n\alpha_n^{-2/n}k_\perp^{2/n}$. Therefore, the vacuum contribution becomes

$$\sigma_{xy}^{vac} = \sigma_0^{(+)} + \sigma_0^{(-)}, \quad \text{(C.26)}$$

$$\sigma_0^{(s)} \approx -se^2n\alpha_n^{2-2/n}\int_{-\Lambda_0-s(Q+\Delta_n)}^{\Lambda_0-s(Q+\Delta_n)}\frac{dk_z}{2\pi}\int_0^{\Lambda_1\to\infty}\frac{k_\perp dk_\perp}{2\pi}(F_{\mathbf{k},1}+F_{\mathbf{k},2}+F_{\mathbf{k},3}), \quad \text{(C.27)}$$

On the other hand, the Fermi surface contribution becomes

$$\sigma_{xy}^{FS} = \sigma_{FS}^{(+)} + \sigma_{FS}^{(-)}, \quad \text{(C.28)}$$

$$\sigma_{FS}^{(s)} \approx -se^2n\alpha_n^{2-2/n}\int_{-\Lambda_0-s(Q+\Delta_n)}^{\Lambda_0-s(Q+\Delta_n)}\frac{dk_z}{2\pi}\int_0^{b}\frac{k_\perp dk_\perp}{2\pi}(F_{\mathbf{k},1}+F_{\mathbf{k},2}+F_{\mathbf{k},3}) \quad \text{(C.29)}$$

$$\times\{\theta(v^2k_z^2+(Ck_z+sC\Delta_n-\mu)^2)-1\} \quad \text{(C.30)}$$

with

$$\begin{aligned}
\text{for} \quad n &= 2 & \qquad \text{for} \quad n &= 3 \\
F_{\mathbf{k},1} &= \frac{k_z}{E_{\mathbf{k}}^3} & F_{\mathbf{k},1} &= \frac{k_z}{E_{\mathbf{k}}^3} \\
F_{\mathbf{k},2} &= \frac{\beta_1^n \alpha_n^{-\frac{2}{n}} k_\perp^{\frac{2}{n}}}{E_{\mathbf{k}}^3} & F_{\mathbf{k},2} &= \frac{\beta_1^n \alpha_n^{-\frac{4}{n}} k_\perp^{\frac{4}{n}} + \beta_2^n \alpha_n^{-\frac{2}{n}} k^{\frac{2}{n}}}{E_{\mathbf{k}}^3} \\
F_{\mathbf{k},3} &= -\frac{3k_z^2 F_{\mathbf{k},2}}{E_{\mathbf{k}}^5} & F_{\mathbf{k},3} &= -\frac{3k_z^2 F_{\mathbf{k},2}}{E_{\mathbf{k}}^5}
\end{aligned} \tag{C.31}$$

Importantly, one should note that $sk_z/2k^3$ is the z-component of the Berry curvature of the Weyl cone with chirality s. Here, $\Theta(x)$ is the Heaviside function. Here, $b = \sqrt{(Ck_z + sC\Delta_n - \mu)^2 - v^2k_z^2}$. Now we are in a position to treat type-I and type-II mWSM differently. We know $\Delta_n \sim \mathcal{O}(1/\omega)$ and μ is an externally tunable parameter. Now for small k_z as considered in the low-energy model: b acquires the form $b \approx \sqrt{\mu^2 - v^2k_z^2}$ when $|C| \ll v$ for type-I, $b \approx \mu - ck_z$ when $|C| \gg v$ for type-II. Therefore, the point to note here is that $\text{sgn}(b)$ is always positive of small k_z (under k_z integral) while $\text{sgn}(b)$ can be positive and negative depending on the $\text{sgn}(k_z)$.

We shall now explicitly write the vacuum and Fermi surface contribution for $n = 3$. Taking the $T \to 0$, and performing the $k_\perp$ integration, we get

$$\begin{aligned}
\sigma_0^s &= -\frac{se^2 n \alpha_n^{2-\frac{2}{n}}}{4\pi^2} \int_{-\Lambda_0 - s(Q+\Delta_n)}^{\Lambda_0 - s(Q+\Delta_n)} dk_z [v\ \text{sgn}(k_z) - \frac{2v^2 \alpha_n^{\frac{2}{n}} \beta_1^n}{\omega\sqrt{\pi}} \Gamma(\frac{5}{6})\Gamma(\frac{5}{3}) k_z^{1/3} \text{sgn}(k_z) \\
&+ \frac{\beta_2^n}{\omega}(-\frac{3v^2 \alpha_n^{\frac{4}{n}}}{2\sqrt{\pi}} \Gamma(\frac{7}{6})\Gamma(\frac{7}{3}) k_z^{-1/3} \text{sgn}(k_z) + \frac{\alpha^{\frac{4}{n}}}{\sqrt{\pi}} \Gamma(\frac{1}{6})\Gamma(\frac{4}{3}) k_z^{-1/3} \text{sgn}(k_z))]
\end{aligned} \tag{C.32}$$

Now, while calculating the Fermi surface contribution, we consider $k_z \to 0$ and $b \neq 0$. As a result, $k_\perp$ integral approximated by only b. The Fermi surface contribution

for $n=3$ is thus given by

$$\sigma_{\rm FS}^{(s)} \approx -\frac{se^2 n\alpha_n^{2-2/n}}{8\pi^2}\int_{-\Lambda-s(Q+\Delta_n)}^{\Lambda-s(Q+\Delta_n)} dk_z\Big[\mathrm{sign}(k_z)-\frac{vk_z}{|C_sk_z-\mu+sC_s\Delta_n|}+b^{\frac{2M}{n}-1}a(M)\beta_2^n\alpha_n^{-2/n}+ b^{\frac{4M}{n}-1}a(2M)\beta_1^n\alpha_n^{-4/n}\Big]\times\left[\left(\Theta\left(v^2k_z^2-(C_sk_z+sC_s\Delta_n-\mu)^2\right)-1\right]\right., \tag{C.33}$$

with $a(M)=\frac{\Gamma(\frac{M}{n}+2)}{(\frac{2M}{n}+2)(\frac{2M}{n}-1)\Gamma(\frac{M}{n}+1)}$ with $M=1$.

Now, the leading order contribution for type-I with $n=3$, σ_{xy}^I is given by

$$\sigma_{xy}^I = \sigma_0+\sigma_{\rm FS} \tag{C.34}$$

$$\sigma_0 = \frac{e^2n\alpha_n^{2-2/n}}{2\pi^2}(Q+\Delta_n+\mathcal{O}(\frac{\beta_1^n}{\omega})+\mathcal{O}(\frac{\beta_2^n}{\omega})) \tag{C.35}$$

$$\sigma_{\rm FS} = n\frac{\alpha^{2-2/n}}{v}\cdot\frac{e^2}{4\pi^2}[C\frac{\mu-C\Delta_n}{6v^2}+\mathcal{O}(\frac{\beta_1^n}{\omega})+\mathcal{O}(\frac{\beta_2^n}{\omega})] \tag{C.36}$$

Now, the leading order contribution for type-I with $n=3$, σ_{xy}^{II} is given by

$$\sigma_{xy}^{II} = \sigma_0+\sigma_{\rm FS} \tag{C.37}$$

$$\sigma_0 = \frac{e^2n\alpha_n^{2-2/n}}{2\pi^2}(Q+\Delta_n+\mathcal{O}(\frac{\beta_1^n}{\omega})+\mathcal{O}(\frac{\beta_2^n}{\omega})) \tag{C.38}$$

$$\sigma_{\rm FS} = n\frac{e^2}{4\pi^2}\frac{\alpha^{2-2/n}}{v}[-\frac{v(c\beta_1-\mu)}{C^2}\ln[\frac{C^2\Lambda}{v(c\beta_1-\mu)}]+\mathcal{O}(\frac{\beta_1^n}{\omega})+\mathcal{O}(\frac{\beta_2^n}{\omega})] \tag{C.39}$$

Bibliography

[1] N. P. Armitage, E. J. Mele, and A. Vishwanath, Rev. Mod. Phys. **90**, 015001 (2018).

[2] B. Yan and C. Felser, Annual Review of Condensed Matter Physics **8**, 337-354 (2017).

[3] L. Savary and L. Balents, Rep. Prog. Phys. **80**, 016502 (2017).

[4] C. Broholm, R. J. Cava, S. A. Kivelson, D. G. Nocera, M. R. Norman, and T. Senthil, Science **367**, 6475 (2020).

[5] L. Landau, Phys. Z. Sowjet **11**, 26 (1937).

[6] X. G. Wen, F. Wilczek, and A. Zee, Phys. Rev. B **39**, 11413 (1989).

[7] V. Kalmeyer and R. B. Laughlin, Phys. Rev. Lett **59**, 18 (1987).

[8] D. Tong, ArXiv, 1606.06687 (2016).

[9] A. Einstein, B. Podolsky, and N. Rosen, Phys. Rev. **47**, 777 (1935).

[10] J. S. Bell, Phys. Phys. Fizika **1**, 3 (1964).

[11] P. Anderson, Mat. Res. Bull. **8**, 153 (1973).

[12] M. J. P. Gingras, Springer (2011).

[13] A. P. Ramirez, A. Hayashi, R. J. Cava, R. Siddhartan, and B. S. Shastry, Nature **399**, 333-335 (1999).

[14] K. A. Ross, L. Savary, B. D. Gaulin, and L. Balents, Phys. Rev. X **1**, 021002 (2011).

[15] L. Savary and L. Balents, Phys. Rev. Lett. **108**, 037202 (2012).

[16] M. Hermele, M. Fisher, and L. Balents, Phys. Rev. B **69**, 064404 (2004).

[17] A. C. Neto, P. Pujol, and E. Fradkin, Phys. Rev. B **74**, 024302 (2006).

[18] N. Shannon, O. Sikora, F. Pollmann, K. Penc, and P. Fulde, Phys. Rev. Lett. **108**, 067204 (2012).

[19] A. Banerjee, S. V. Isakov, K. Damle, and Y. B. Kim, Phys. Rev. Lett. **100**, 047208 (2008).

[20] M. Taillefumier, O. Benton, H. Yan, L. D. C. Jaubert, and N. Shannon, Phys. Rev. X **7**, 041057 (2017).

[21] L. Pauling, J. Am. Chem. Soc. **57**, 2680 (1935).

[22] R. Moessner, S. L. Sondhi, and E. Fradkin, Phys. Rev. B **65**, 024504 (16 pages).

[23] J. Rochner, L. Balents, and K. P. Schmidt, Phys. Rev. B **94**, 201111 (2016).

[24] P. Emonts and S. Wessel, Phys. Rev. B **98**, 174433 (2018).

[25] G. Chen, Phys. Rev. B **94**, 205107 (2016).

[26] L. Savary and L. Balents, Phys. Rev. Lett. **118**, 087203 (2017).

[27] O. Benton, Phys. Rev. Lett. **121**, 037203 (2018).

[28] J.-J. Wen, S. M. Koohpayeh, K. A. Ross, B. A. Trump, T. M. McQueen, K. Kimura, S. Nakatsuji, Y. Qiu, D. M. Pajerowski, J. R. D. Copley, and C. L. Broholm, Phys. Rev. Lett. **118**, 107206 (2017).

[29] D. Rokhsar and S. Kivelson, Phys. Rev. Lett. **61**, 2376 (1988).

[30] A. Wietek and A. M. Lauchli, Phys. Rev. E **98**, 033309 (2018).

[31] M. Kardar, Cambridge University Press, ISBN: 9780521873413 (2007).

[32] M. Rigol, T. Bryant, and R. R. P. Singh, Phys. Rev. Lett. **97** (2006).

[33] A. B. Kallin, K. Hyatt, R. R. P. Singh, and R. G. Melko, Phys. Rev. Lett. **110**, 135702 (2013).

[34] B. Tang, E. Khatami, and M. Rigol, Computer Physics Communications **184**, 557-564 (2013).

[35] M. Rigol, T. Bryant, and R. R. P. Singh, Phys. Rev. E **75**, 061118 (2006).

[36] M. E. Peskin and D. V. Schroeder, Avalon Publishing, ISBN: 9780813345437 (1995).

[37] Y. Ferreiros, A. A. Zyuzin, and J. H. Bardarson, Phys. Rev. B **96**, 115202 (2017).

[38] G. Sharma, P. Goswami, and S. Tewari, Phys. Rev. B **96**, 045112 (2017).

[39] A. A. Burkov and L. Balents, Phys. Rev. Lett **107**, 127205 (2011).

[40] G. B. Halasz and L. Balents, Phys. Rev. Lett. **85**, 035103 (2012).

[41] Wan and X et al., PRB **83**, 205101 (2011).

[42] G. Xu, H. Weng, Z. Wang, X. Dai, and Z. Fang, Phys. Rev. Lett. **107**, 186806 (2011).

[43] D. E. Kharzeev and H.-U. Yee, Phys. Rev. D **83**, 085007 (2011).

[44] J. Zhou, H.-R. Chang, and D. Xiao, Phys. Rev. B **91**, 035114 (2015).

[45] H. Nielsen and M. Ninomiya, Phys. Lett. B **130**, 389 (1983).

[46] S.-Y. Xu and et al., Science **349**, 613 (2015).

[47] H. et. al, Phys. Rev. B **95**, 241108(R) (2017).

[48] H. Weng, C. Fang, Z. Fang, B. A. Bernevig, and X. Dai, Physical Review X **5**, 011029 (2015).

[49] C. Fang, M. J. Gilbert, X. Dai, and B. A. Bernevig, Phys. Rev. Lett. **108**, 266802 (2012).

[50] S.-M. Huang and et al., Proc. Nat. Acad. Sci. **113**, 1180 (2016).

[51] L. Lepori, M. Burrello, and E. Guadagnini, Journal of High Energy Physics **06**, 110 (2018).

[52] R. M. A. Dantas, F. Pena-Benitez, B. Roy, and P. Surowka., Phys. Rev. Research **2**, 013007 (2020).

[53] T. Oka and H. Aoki, Physical Review B **79**, 081406(R) (2009).

[54] A. Eckardt and E. Anisimovas, New J. Phys. **17**, 093039 (2015).

[55] T. Kitagawa, T. Oka, A. Brataas, L. Fu, and E. Demler, Phys. Rev. B **84**, 235108 (2011).

[56] E. H. Hall, Am. J. Math. **2**, 287 (1879).

[57] E. H. Hall, Phil. Mag. **12**, 157 (1881).

[58] N. Nagaosa, J. Sinova, S. Onoda, A. H. MacDonald, and N. P. Ong, Rev. Mod. Phys. **82**, 1539 (2010).

[59] G. D. Mahan, Springer US, ISBN: 9780306463389 (2000).

[60] D. J. Thouless, M. Kohmoto, M. P. Nightingale, and M. den Nijs, Phys. Rev. Lett **49**, 405 (1982).

[61] R. Applegate, N. R. Hayre, R. R. P. Singh, T. Lin, A. G. R. Day, and M. J. P. Gingras, Phys. Rev. Lett. **109**, 097205 (2012).

[62] N. R. Hayre, K. A. Ross, R. Applegate, T. Lin, R. R. P. S. B. D. Gaulin, and M. J. P. Gingras, Phys. Rev. B **87**, 184423 (2013).

[63] H. Changlani, cond-mat/arXiv:1710.02234.

[64] R. B. Griffiths, Phys. Rev. Lett. **23**, 17 (1969).

[65] T. Pardini, A. Menon, S. Hau-Riege, and R. R. P. Singh, Phys. Rev. B **100**, 144437 (2019).

[66] R. N. Bhatt and P. A. Lee, Phys. Rev. Lett. **48**, 344 (1982).

[67] D. S. Fisher, Phys. Rev. B **50**, 3799 (1994).

[68] R. R. P. Singh, Phys. Rev. Lett. **104**, 177203 (2010).

[69] I. Kimchi, A. Nahum, and T. Senthil, Phys. Rev. X **8**, 031028 (2018).

[70] A. Andreanov, J. T. Chalker, T. E. Saunders, and D. Sherrington, Phys. Rev. B **81**, 014406 (2010).

[71] A. A. Zyuzin and A. A. Burkov, Phys. Rev. B **86**, 115133 (2012).

[72] Z. Li and J. P. Carbotte, Phys. Rev. B. **89**, 165420 (2014).

[73] X. Zhou, Y. Xu, and G. Jin, Phys. Rev. B **92**, 235436 (2015).

[74] C. R. Wang, W. Lu, L. Hao, W. Lee, T. Lee, F. Lin, I.-C. Cheng, and J. Chen, Phys. Rev. Lett **107**, 186602 (2011).

[75] Z. H.-Xin, W. T.-Tong, G. J.-Song, L. Shuai, S. Y.-Jun, and L. G.-Lin, Chin. Phys. Lett. **31**, 030503 (2014).

[76] X. Zhai, G. Zin, and P. R. B, **89**, 235416 (2014).

[77] A. Eckardt, Rev. Mod. Phys. **89**, 011004 (2017).

[78] R. Wang, B. Wang, R. Shen, L. Sheng, and D. Xing, EPL **105**, 17004 (2014).

[79] D. Sinha and EPL, **115**, 37003, (2016).

[80] J. Inoue, A. Tanaka, and P. R. Lett, **105**, 017401 (2010).

[81] B. Dora, J. Cayssol, F. Simon, R. Moessner, and P. Lett, **108**, 056602 (2012).

[82] M. A. Sentef, M. Claassen, A. F. Kemper, B. Moritz, T. Oka, J. K. Freericks, and T. P. Devereaux, Nat. Comm. **6**, 7047 (2015).

[83] K. Behnia and H. Aubin, Rep. Prog. Phys. **79**, 046502 (2016).

[84] A. A. Burkov, Phys. Rev. Lett. **113**, 187202 (2014).

[85] G. Sharma, P. Goswami, and S. Tewari, Phys. Rev. B **93**, 035116 (2016).

[86] J. F. Steiner, A. V. Andreev, and D. A. Peskin, Phys. Rev. Lett **119**, 036601 (2017).

[87] T. Oka and H. Aoki, Phys. Rev. B **79**, 169901 (2009).

[88] L. E. F. F. Torres, P. M. Perez-Piskunow, C. A. Balseiro, and G. Usaj, Phys. Rev. Lett. **113**, 266801 (2014).

[89] H. Dehghani and A. Mitra, Phys. Rev. B **93**, 245416 (2016).

[90] T. Iadecola, T. Neupert, and C. Chamon, Phys Rev. B **91**, 235133 (2015).

[91] H. H. et al., Nature Comm. **8**, 13940 (2017).

[92] L. Bucciantini, S. Roy, S. Kitamura, and T. Oka, Phys. Rev. B **96**, 041126(R) (2017).

[93] J. Zou and B. Liu, Phys. Rev. B **95**, 2015125 (2017).

[94] E. J. Sie, J. W. McIver, Y. Lee, L. Fu, and J. Kong, N. Gedik Nat. Materials **14**, 290 (2015).

[95] Y. H. W. et al., Science **342**, 453 (2013).

[96] S. J. W. et al., Phys. Rev. B **97**, 161404 (2018).

[97] U. S. et al., J. Phys. Condens. Matter **29**, 325701 (2017).

[98] M. Hirschberger. and et al., Nat. Mater. **15**, 1161 (2016).

[99] J. K. Freericks, H. R. Krishnamurthy, and T. Pruschke, Phys. Rev. Lett. **102**, 136401 (2009).

[100] M. S. et al., Phys. Rev. X **3**, 041033 (2013).

[101] S. Ahn, E. J. Mele, and H. Min, Phys. Rev. B **95**, 161112(R) (2017).

[102] B. Roy, P. Goswami, and V. Juricic, Phys. Rev. B **95**, 201102(R) (2017).

[103] J. H. Shirley, Phys. Rev. **138**, B979 (1968).

[104] J. C. S.-S. et al., Annals of Physics **531**, 1900035 (2019).

[105] X.-L. Qi, Y.-S. Wu, and S.-C. Zhang, Phys. Rev. B **74**, 085308 (2006).

[106] A. Menon and D. Chowdhury, and B. Basu Phys. Rev. B **98**, 205109 (2018).

[107] M. Wackerl, P. Wenk, and J. Schliemann, Phys. Rev. B **101**, 184204 (2020).

[108] A. Kumar, M. Rodriguez-Vega, T. Pereg-Barnea, and B. Seradjeh, Phys. Rev. B **101**, 174314 (2020).

[109] H. Dehghani, T. Oka, and A. Mitra, Phys. Rev. B **91**, 155422 (2015).

[110] H. Dehghani and A. Mitra, Phys. Rev. B **92**, 165111 (2015).

[111] J. M. Luttinger, Phys. Rev. **135**, A1505 (1964).

[112] R. Lundgren, P. Laurell, and G. A. Fiete, Phys. Rev. B **90**, 165115 (2014).

[113] M. Jonson and G. D. Mahan, Phys. Rev. B **21**, 4223 (1980).

[114] S. Nandy, G. Sharma, A. Taraphder, and S. Tewari, Phys. Rev. Lett. **119**, 176804 (2017).

[115] S. Saha and S. Tewari, Eur. Phys. J. B **91**, 4 (2018).

[116] K. Sonowal, A. Singh, and A. Agarwal, Phys. Rev. B **100**, 085436 (2019).

[117] M. Kargarian, M. Randeria, and N. Trivedi, Scientific Reports **5**, 12683 (2015).

[118] M. Tahir and P. Vasilopoulos, Phys. Rev. B **91**, 115311 (2015).

[119] M. Tahir, A. Manchon, and U. Schwingenschlögl, Journal of Applied Physics **116**, 093708 (2014).